TECHNISCHE UNIVERSITÄT MÜNCHEN

Lehrstuhl für Nukleartechnik

Functional foam coatings inside tubing and custom developed diamond ignition targets

Christoph Dawedeit

Vollständiger Abdruck der von der Fakultät für Maschinenwesen der Technischen Universität München zur Erlangung des akademischen Grades eines

Doktor-Ingenieurs (Dr.-Ing.)

genehmigten Dissertation.

Vorsitzender: Univ.-Prof. Dr. med., Dr. Ing. habil. Erich Wintermantel
Prüfer der Dissertation:

1. Univ.-Prof. Rafael Macián-Juan, Ph. D.
2. Univ.-Prof. Dr. rer. nat. Marcus Bäumer, Universität Bremen

Die Dissertation wurde am 22.04.2014 bei der Technischen Universität München eingereicht und durch die Fakultät für Maschinenwesen am 15.09.2014 angenommen.

Nothing is easier than self-deceit.
For what each man wishes,
that he also believes to be true.[1]

[1]Demosthenes (384 BC - 322 BC)

Abstract

English The development of inertial confinement fusion (ICF) targets requires precise understanding of target shell compression and the temperatures of the heavy hydrogen fuel during compression. Diamond with its high atomic density can reach higher pressures during compression than lower dense materials and thus is one promising target shell material. The surface roughness, density, hydrogen content and graphitic sp^2 carbon content are characterized in dependency to the grain size. The grain size ranged between 9 μm for microcrystalline diamonds and 5 nm for nanocrystalline samples. While the density of the microcrystalline material is higher which is favorable for ICF, the nanocrystalline diamond has a desirable smoother surface. In a sandwich target characterized here the micro- and nanocrystalline diamonds are combined by growing alternating layers on top of each other. For ICF experiments a high density with a smooth surface is desired to produce cost-effective ICF target shells.

To measure the temperature of the heavy hydrogen fuel during compression in the ICF target shell the characteristic emission spectrum of a high atomic number element (dopant) can be used. Here a coating process is shown which allows the uniform distribution of the dopant embedded in an aerogel. For the process the initially liquid aerogel precursor solution is filled with nL precision in the sperical 2 mm diameter diamond target shell and then uniformly distributed while the viscosity of the sol gel increases over time. Rheology experiments together with an analytical solution and simulation are used to predict the quality of the coatings. After the coating quality was determined and verified inside glass cylinders the results were used to coat the spherical diamond shells and functional catalytic coatings inside metal tubing. Coatings inside stainless steel tubing for possible catalytic reactors were done to show the generality of the coating procedure.

All layers were supercritically dried to produce a functional aerogel and for some catalytic coatings porosity was even achieved by drying at ambient conditions to obtain a xerogel. The resulting foam layer inside targets could even be used as a sponge which determines the shape of the liquid heavy hydrogen fuel. This sponge would facilitate the possible production of several thousand targets per day for an ICF power plant.

German Für die Entwicklung von Trägheitskernfusionstargets ist das Verständnis der Materialkompression und der Temperaturen des Wasserstoffbrennstoffs während der Kompression sehr wichtig. Diamant ist aufgrund der hohen atomaren Dichte ein vielversprechendes Material, da hohe Kompressionsdrücke erreicht werden können. Die Oberflächenrauhigkeit, die Dichte, der Wasserstoffgehalt und der graphitische sp^2 Kohlenstoffanteil von unterschiedlichen Diamanten werden in Abhängigkeit der Korngröße charakterisiert. Die Korngröße beträgt bis zu 9 μm für mikrokristallinen Diamant und ist bis zu 5 nm klein für nanokristallinen Diamant. Die hohe Dichte von mikrokristallinem Diamant und die glatte Oberfläche von nanokristallinem Diamant sind wichtige Kriterien für kosteneffiziente Trägheitsfusionstargets. Mit abwechselnden Schichten aus mikro- und nanokristallinem Diamant wurde ein Sandwich-target hergestellt, um eine hohe Dichte mit geringer Oberflächenrauhigkeit zu erreichen.
Um die Temperatur während der Kompression des Wasserstoffbrennstoffs zu bestimmen, wird das charakteristische Emissionssprektrum eines Elements mit einer hohen Ordnungszahl genutzt. In dieser Arbeit wird ein Prozess gezeigt bei dem eine Aerogel-Schicht, welche ein schweres Element enthält, in ein kugelförmiges Diamant-target gefertigt wird. Für diesen Prozess wird die anfänglich flüssige Aerogel Lösung mit nL Präzision in eine hohle 2 mm Durchmesser target-Kugel/ Kapsel gefüllt. Anschließend wird die Kapsel, bzw. das Rohr so gedreht, dass sich die Aerogel Lösung gleichmäßig verteilt, während die Viskosität ansteigt und die Lösung erstarrt. Mit Hilfe von Rheologie Messungen, einer analytischen Lösung und einer Computer-Simulation werden die Qualität der Beschichtungen für Zylinder- und Kugel-Geometrien vorhergesagt. Nachdem die Beschichtungsqualität

in Glaszylindern bestätigt wurde, sind die Ergebnisse genutzt wurden, um die funktionalen Beschichtungen in Kapseln und Metallrohren aufzutragen. Um die Allgemeingültigkeit des Beschichtungsprozesses zu zeigen, wurden zusätzlich katalytische Beschichtungen in rostfreien Metallrohren aufgetragen. Alle resultierenden Beschichungen wurden super-kritisch getrocknet, um ein Aerogel herzustellen und bei ein paar katalytischen Beschichtungen war das Trocknen an Luft genug, um ein poröses Xerogel zu erhalten. Das Aerogel in den Targets ist sogar robutst genug, dass es als Schwamm genutzt werden kann, um die Form des schweren Wasserstoffs zu definieren. Dieser Schwamm würde die Produktion von mehreren tausend targets pro Tag für ein Trägheitsfusionskraftwerk ermöglichen.

Preface

This dissertation is mainly based on my work at Lawrence Livermore National Laboratory from 2010 to 2013. The Nanoscale Synthesis and Characterization Laboratory (NSCL) group which I was a part of worked on new target designs for the Nation Ignition Facility. The development of inertial confinement fusion targets is a complex project that requires an interdisciplinary team environment. My contributions were mainly in the area of analysis of the characterization results from diamond films, rheological measurements, coating experiments as well as design and development of custom devices. In 2013 I further used my knowledge gained in Livermore to coat gel layers for possible Fischer-Tropsch applications at Universiyt of Bremen.
More details about my contributions are summarized in the list on page 128.
This work is divided in seven chapters. The first introduction chapter gives an general overview and connects my work for diamond targets, aerogel coatings inside capsules and catalytic coatings. The tasks for my thesis are described in the requirements section which were either defined by my advisors or physical purposes. The foundation of my work and similar techniques to fulfill these requirements are part of the next prior art chapter. Each of the following three chapters is then separated in an experimental, results and discussion, and conclusion section. The diamond characterization and growth are the foundation for the target coatings inside diamond capsules and is described in chapter 4. This work was mainly performed shortly after my arrival in Livermore. Chapter 5 is

about the coatings inside targets, the analysis and manipulation of coating parameters and gelation behavior as well as the drying and foam characterization. Chapter 5 is the most detailed section since this was my major project for my PhD. The knowledge of the coatings is then used at University of Bremen in chapter 6 to produce catalytic coatings inside stainless steel tubing which are promising Fischer-Tropsch reactors. The last chapter summarizes the three previous chapters and gives and outlook about potential developments for the future.

During my time as PhD student I published the following articles and record of invention that contribute to this thesis:

1. **Dawedeit, C.**; Walton, C.; Chernov, A.; Kim, S.; Worsley, M.; Braun, T.; Gammon, S.; Satcher, J.; Wu, K.; Hamza, A.; Biener, J., Coating functional sol–gel films inside horizontally-rotating cylinders by rimming flow/state. J. Sol-Gel Sci. Technol. 2012, 1-8.
2. **Dawedeit, C.**; Kim, S. H.; Braun, T.; Worsley, M. A.; Letts, S. A.; Wu, K. J.; Walton, C. C.; Chernov, A. A.; Satcher, J. H.; Hamza, A. V.; Biener, J., Tuning the rheological properties of sols for low-density aerogel coating applications. Soft Matter 2012, 8 (13), 3518-3521.
3. Biener, J.; **Dawedeit, C.**; Kim, S. H.; Braun, T.; Worsley, M. A.; Chernov, A. A.; Walton, C. C.; Willey, T. M.; Kucheyev, S. O.; Shin, S. J.; Wang, Y. M.; Biener, M. M.; Lee, J. R. I.; Kozioziemski, B. J.; Buuren, T. v.; Wu, K. J. J.; J. H. Satcher, J.; Hamza, A. V., A new approach to foam-lined indirect-drive NIF ignition targets. Nucl. Fusion 2012, 52 (6), 062001.
4. Kim, S. H.; Worsley, M. A.; Valdez, C. A.; Shin, S. J.; **Dawedeit, C.**; Braun, T.; Baumann, T. F.; Letts, S. A.; Kucheyev, S. O.; Jen J. Wu, K.; Biener, J.; Satcher, J. H.; Hamza, A. V., Exploration of the versatility of ring opening metathesis polymerization: an approach for gaining access to low density polymeric aerogels. RSC Advances 2012, 2 (23), 8672-8680.
5. **Dawedeit C.**; Kucheyev S. O.; Shin S. J.; Willey T. M.; Bagge-Hansen M.; Braun T.; Wang Y. M.; El-Dasher B. S.; Teslich N. E.; Biener M. M.; Ye J.; Kirste L.; Roehling C. C.; Wolfer M.; Woerner E.; van Buuren A. W.; Hamza A. V.; Wild C.; Biener J., Grain size dependent physical and chemical properties of thick CVD diamond films for high energy density physics experiments. Diam. Relat. Mat. 2013, Accepted Manuscript.
6. **Dawedeit C.**; Klink M.; Baeumer M.; Wittstock A., Catalytic Fischer-Tropsch coatings by the rimming state method inside stainless steel tubing, to appear in: J. Sol-Gel Sci. Technol. 2014

7. Patent: **DAWEDEIT, C.**; Biener, J.; Hamza, A.V.; Kim, S.H.; Satcher, J.; WALTON, C.C.; WORSLEY, M.A.; Wu, K.J., Coating of Spheres and Tubes with Aerogels. WO 2013055433. 2013

Acknowledgements

I would like to acknowledge Marcus Bäumer and Arne Wittstock at University of Bremen who made my Ph.D. work possible. At Lawrence Livermore National Laboratory special thanks goes Steve Letts who thought me all the rheology skills and always helped me immediately to build new equipment or offered his equipment. Moreover I am grateful for the entire NSCL group that always pushed the project forward to achieve an outstanding result and enabled me to equip an entire lab room. Special thanks goes to my advisors Alex V. Hamza, Jürgen Biener and Kuang Jen Wu for hosting me and financial support.

Especial thanks goes to Linda Jones and Margitta Franke the administrative staff of LLNL and TUM who managed all the difficult communications across the ocean. In addition I would like to thank Prof. Macian Juan who made my Ph.D. work in Livermore and Bremen possible by being my advisor in Munich.

Apart from that I appreciated all the support in tough as well as in good times during my work in Livermore from my family Ute, Heiko and Marius Dawedeit.

This work was partly performed under the auspices of the U.S. Department of Energy by Lawrence Livermore National Laboratory under Contract DE-AC52-07NA27344.

Contents

1

Introduction

The development of new inertial confinement (ICF) fusion targets might enable nuclear fusion to be a possible answers to supply the energy demand of the future without emitting carbon dioxide (CO_2). In the last decades the population increased by about 1.2 % per year while the annual CO_2 emission per capita stayed constant around 4 $\frac{t \cdot CO_2}{capita}$.(1, 105) This means about 330 million tons of CO_2 are emitted additionally every year. At this emission rate the carbon cycle on earth is not fast enough to transform CO_2 into solid or liquid based carbon compounds (e.g. oil, coal, wood, etc.).(93) Consequently the demand of carbon-based fuels in the future cannot get satisfied anymore and the increasing CO_2 in the environment impacts the climate.(16) Nuclear fusion energy can mitigate these effects by being an environmental friendly, virtually inexhaustible energy source.(75)

To achieve the conditions required for nuclear fusion high densities and temperatures like they occur in stars are necessary. In 1929 Atkinson explained how nuclear fusion supplies the energy of the stars.(4) In stars light elements like hydrogen constantly fuse with each other and release energy. At high densities and temperatures the usually repelling coulomb forces between two elements are too weak to prevent the collision between nuclei. The collision of two nuclei can lead to fusion where one bigger element is created out of two lighter nuclei. This new element requires less energy to be stable and thus it releases energy.

A few years later around 1955 this process of nuclear fusion was reproduced on earth as described by Teller.(103) From there on the idea of the usage of nuclear fusion for energy generation started, leading to several different approaches. Besides the unproven idea of cold fusion the nuclear fusion process is mainly differentiated between magnetic- and inertial- confinement fusion (ICF).(26) In magnetic confinement fusion a hovering fuel plasma is contained by magnets while it is heated to reach the conditions for fusion.(35) Currently the major test facility the International Thermonuclear Experimental Reactor (ITER) for magnetic confinement fusion is being built in Cadarache, France.(21) In ICF the fuel is confined to reach extreme densities that are required for nuclear fusion.(12, 74) ICF is currently studied at the National Ignition Facility (NIF) at Lawrence Livermore National Laboratory (LLNL).(40)

Here I am focusing on ICF and in particular on the ablator and fuel-layer within the target which are confined to achieve nuclear fusion. The ablator of the target has to absorb as much energy as possible and transfer this energy in form of a shockwave to the fuel. To build the most efficient ablators high energy density (HED) physics experiments are required to optimize the material characteristics at extreme confinement conditions. Here I am investigating the material characteristics of diamond which is one possible ablator target. For the fuel-layer I am explaining a new process to get a foam layer inside a hollow 2 mm capsule. This foam layer acts as a sponge and defines the shape of the liquid fuel layer or it can be used to bring dopants in direct contact with the fusion fuel which is required to investigate the temperatures during the fusion process.

1.1 Inertial confinement fusion (ICF)

In ICF the fusion relies on the inertia of the fuel mass to generate confinement.(12, 60, 74) High densities and temperatures are achieved by a laser induced implosion of the spherical ablator target which contains the fusion-fuel. Figure 1.1 shows the ICF process schematically with a hollow ablator targets which contains a hydrogen fuel layer. In the first step the radiation beams get absorbed by the ablator target to create plasma surrounding the fuel. To achieve a high efficiency it is important that the target uniformly heats and that a partially melted state is avoided to mitigate instabilities. In the second step the molten shell ablates which means that the energy of the ablator

blow-off is transferred to the fuel. The inertia of the fuel now drives the fuel layer into the center of the capsule. Radiation beams are still pushing on the target to avoid an early explosion of the dense core. The center gets so dense and hot that the compression creates a hot spot in the fuel. In the last step the hot spot leads to ignition which spreads through the dense surrounding fuel yielding to the complete ignition of the nuclear fuel. At NIF the energy is supplied by 192 lasers with a total power of 2 MJ [1] ultraviolet light and up to two shots can be fired per day.(59) For future energy generation with ICF a Laser Inertial Fusion Energy (LIFE) reactor is planned which would shoot about 10-15 shots per second with about the same energy as NIF.(70, 90)

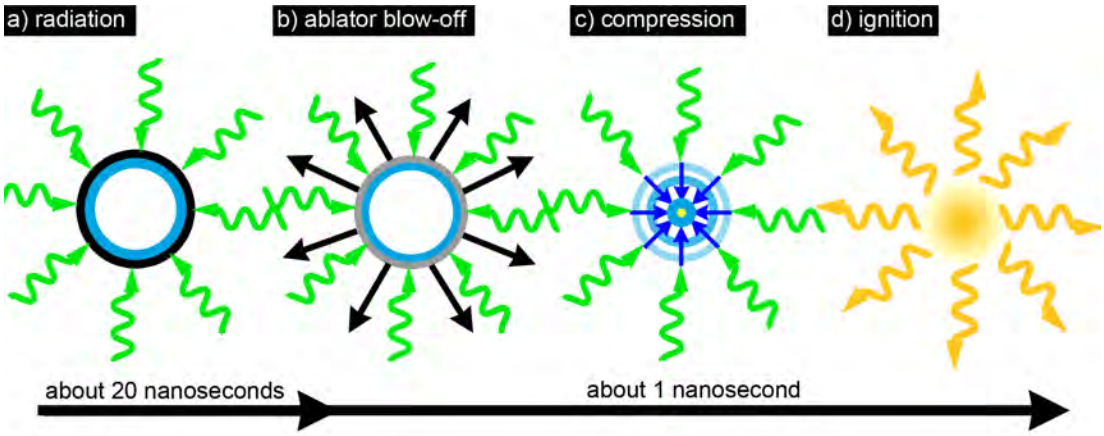

Figure 1.1: ICF schematic - a) the fuel (blue) layered capsule (black) absorbs the surrounding radiation (green) and creates a plasma envelope around the fuel; b) the capsule ablates which means that the energy of the blow off of the capsule is transfered to the fuel. Around 10 % of the ablator material is still surrounding the fuel to mitigate instabilities; c) the blow-off and the radiation compress the fuel to reach a density and temperature which creates a hot-spot; d) this hot-spot spreads, ignites the the remaining fuel and releases energy (yellow)

1.2 Targetdesign

The energy transport for the implosion of the ablator can be either direct driven or indirect driven. In the direct drive configuration the lasers hit the ablator shell directly

[1] The power of the laser system was recently upgraded from 1.8 MJ to 2 MJ

where as in the indirect configuration the ablator is mounted into a cylinder called hohlraum that converts the laser light to x-rays which bath the ablator shell. The ablation uniformity is better in the indirect drive configuration since the capsule is uniformly surrounded by x-rays. As mentioned above the ablation uniformity is crucial for successful nuclear fusion experiments. This increase in uniformity sacrifices some energy in the x-ray conversion process though.
Here I am focusing on the indirect drive approach which is currently used at the NIF.(40, 59) The cross section of a schematic indirect drive target is shown in Fig. 1.2. The laser beams are focused on the inner walls of the hohlraum and enter the hohlraum through the laser entrance holes. By the absorption of the laser light in the high atomic number material of the hohlraum x-rays are emitted (Black Body radiation). These generated x-rays now bath the ablator which absorbs the x-rays. The ablator target containing the fuel is centered in the middle of the hohlraum by two plastic membranes, called tents. A small fill-tube is connected to the ablator target which is used to fill the capsule with heavy hydrogen, the fusion fuel. To control the fuel layer of the hydrogen within the capsule the entire hohlraum is chilled to about 13 K by its attached silicone arms which hold the hohlraum. The metal on the outside of the target is used to scatter uncontrolled laser light to limit the amount of light being reflected back in the laser optics beam.

1.3 Fuel layering

Within the about two millimeter diameter ablator target a layer of about 70 μm thick hydrogen is required as fusion fuel. For nuclear fusion the two heavy hydrogen isotopes deuterium and tritium (D-T) require the least energy to fuse and are consequently used for fusion experiments. These two hydrogen isotopes only have a short lifetime in the low temperature (13 K) of their solid state because of the generation of $_3He$. Thus mechanical fabrication approaches to build the ice layer are not feasible and the ice layers are mainly built by slowly freezing D-T from liquid or vapor. At NIF the layers growth from liquid and vapor usually starts with a single crystal seed. The process to build an entire layer from this seed crystal takes between 8 and 16 hours and grain boundaries which roughen the surface sometimes occur.(53) For the mass production of targets where about 15 targets are shot every second the growth from single seeds is

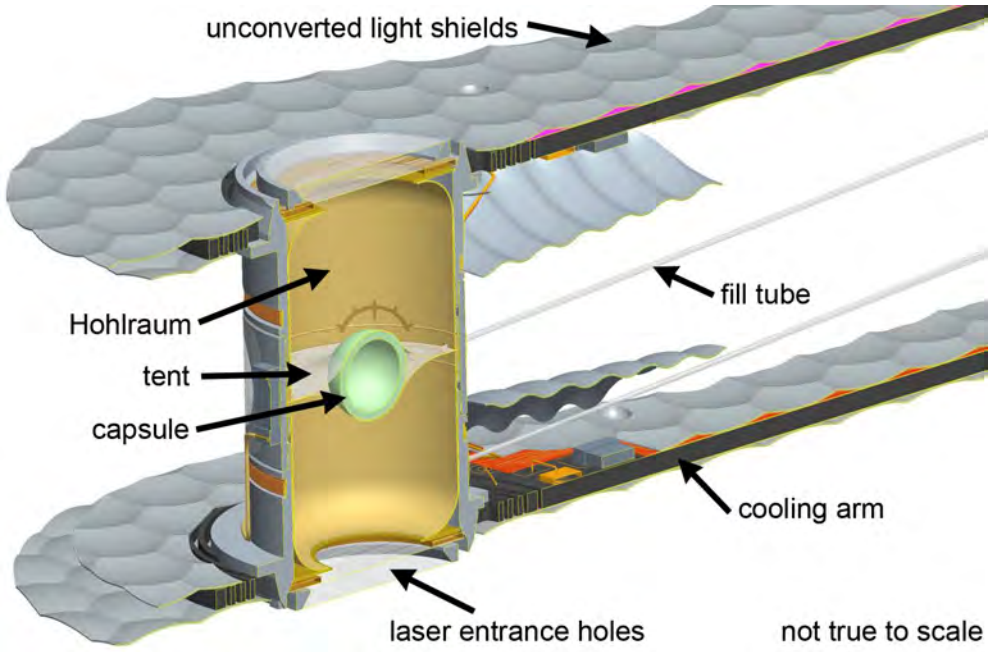

Figure 1.2: Target cross-section schematic - shows the entire target configuration for NIF with the cooling arms which hold the hohlraum and acurately distribute the temperature. The can shaped holhlraum which absorbs the laserlight entering through the laser entrance holes and converting the light to soft-x-rays. These x-rays bath the capsule in the center of the holhlraum which is hold by a thinn membrane, the tent. The fuel for the capsule is supplied by the fill tube, adapted from Hohlraum viewgraphs Vivini Tour 12-10-01

too time and labor intensive. The use of a scaffold which defines the shape of the D-T fuel is a promising option to decrease the time for target production. Here I am using an aerogel which can be used as a sponge to shape the fuel layer within the capsule as shown in Fig. 1.3. To successfully use an aerogel-scaffold a layer needs to be built inside the ablator capsule.

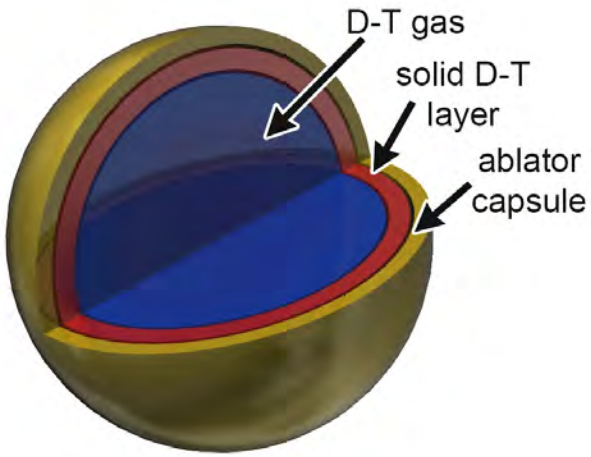

Figure 1.3: Ablator capsule schematic - the ablator shell gets filled with a solid layer of deuterium tritium (D-T) containing the evaporated gas from the solid D-T in the center of the capsule

1.4 Aero- and Xerogels

The outstanding properties of aerogel with its low-density, small pore-size, high strength, being a low atomic number material and adjustable sol-gel chemistry make aerogels a promising target material to use them as scaffold for D-T.(32, 42, 45, 47, 56) The typical fabrication of an aerogel is shown in Fig. 1.4. This process is initiated by adding a catalyst to a solution. Polymerization of precursor molecules in solution lead to formation of so called primary particles which aggregate into longer chains forming the so called "wet gel". During this process the viscosity of the precursor solution increases until all particles are connected. When suitable procedures are applied the typical pore structure and network can be maintained when the liquid gets extracted out of the wet gel. The remaining solid with gas voids is called aerogel.(47) Special liquid extraction

techniques are required because of the capillary forces that would collapse the gel during drying. Supercritical and freeze drying circumvent these forces by using a supercritical liquid or by sublimation. In contrast xerogels are dried at room temperature and the gel network either collapses or shrinks.

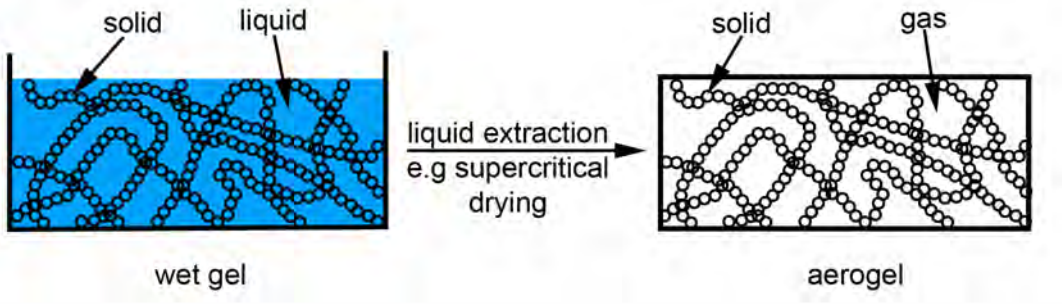

Figure 1.4: Aerogel schematic - particles form a chain within a liquid which is usually done by a catalyst or condensation reaction. The liquid is then removed by supercritical drying or freeze drying leaving particle chains behind. The shape of the dried gel has the same shape as the liquid gel had before

1.5 Coating and rheology

The coating of functionalized aerogels attracted a lot of attention in the past because of its capability to incorporated catalyst materials, dopants and reinforcing carbon nanotubes.(52, 61, 71, 107, 113, 115) Especially for ablator capsules the ability to embed dopents in the scaffold of the fuel layer is important to use their spectra during ignition as temperature gauge. Dip-coating, spin- coating and centrifugal coatings are widely studied fields to apply layers to flat or cylindrical geometries. But the coating within 2 mm spherical capsules requires a new approach to achieve a uniform coating. Here, this approach of generating a uniform film in a slowly rotating geometry is first tested in cylinders and then the technique is adjusted for the use in spherical geometries. The same technique can also be used to coat the outside of a cylinder or capsule, but this is not part of this thesis.(68)

A uniform layer of liquid in a horizontally rotating, partially filled cylinder can be observed when the viscosity and rotational speed are in the correct ratio. This state

of having an uniform layer is called the rimming state and is used for the coatings here. Compared to dip-coating this technique only requires simple hardware and no venting techniques and withdrawing velocity adjustments to achieve an uniform layer are required.(83) Centrifugal coating has the disadvantage that the colloidal sol can precipitate because of the centrifugal forces.(69) However the technique described here requires a precise knowledge of the viscosity over time behavior to set the correct coating conditions. This data is acquired by rheology measurements which determine the viscosity *vs.* time behavior, the elastic- and plastic- storage modulus of the sol and sol-gel transition.

In the partially filled horizontally rotating cylinder a puddle at the bottom of the cylinder decreases with the increasing velocity of the precursor solution until the viscosity of the rimming state region is reached. However, different sol-gels have different rheological properties and differ in their shear sensitivity. During rotation an inevitable recirculation region in the initial puddle of the precursor solution develops in the presence of gravity.(64) These shear forces can damage the fragile wet gel structure during the buildup of the gel porous network. To prevent this damage the viscosity needs to be above a threshold where the shear forces disappear since a viscous liquid sticks to the cylinder walls and does not flow anymore. A Newtonian sol-gel which increases the viscosity over time and a shear thinning liquid where the viscosity can be reversibly lowered are tested here.

In a shear thinning gel used here this effect is used to lower the viscosity by shaking and to distribute the sol. During rotation for coatings the shear forces are not sufficient to prevent the gel network buildup. This shear thinning aluminium-iron-oxide gel is used for catalytic coatings inside metal tubing. Another solution to mitigate these shear forces in Newtonian liquids is by increasing the viscosity and hence allowing the formation of the rimming state at lower velocities. Here I show how a co-polymerization process for CH_x aerogels is developed which increases the viscosity before the sol-gel transition and thus decreases the shear forces experienced by the gelling system. The co-polymerization process is exemplary shown for poly(dicyclopentadiene) (PDCPD) aerogels which are pure CH_x gel. By the addition of norbornene (NB) to the 3-dimensionally branched PDCPD gel the cross-linking capabilities of the PDCPD were limited leading

to a more linear chained network. Linear gel-networks have a higher viscosity before their sol-gel transition since more bonds are required to interconnect all particles as describe by the classical theory of gelation.(27) Compared to pre-polymerization, use of higher viscosity solvents, and substitution of cross-linked polymers by linear polymers approaches the benefit of this technique is that the viscosity can be continuously adjusted by the addition of the co-monomer NB.(18, 48, 57, 80, 114)

With the guidance of Melo's and Moffat's analytical approximation to reach the rimming state for liquids a study with four aerogels was conducted to achieve rimming state coatings in cylinders.(64, 68) First the analytical approximation is experimentally verified with various silicone oils to predict the transition to the rimming state region. In addition the position of the puddle at low speeds was measured and the velocity range at intermediate speeds for a mixture of the puddle and the rimming state was determined. This data was then used to determine the error of the analytical approximation and to ensure that the computational fluid dynamics simulations code accurately captures the rotating liquid. Apart from that the observations with the silicone oil showed that the region with the mixture of the puddle and the rimming state should be avoided to reach uniform coatings. This means that for aerogel coating the velocity should be transitioned directly in the rimming state without going through the mixed state. Here I show that uniform coatings can be achieved with the knowledge of the viscosity *vs.* time behavior and by triggering the transition in the rimming state abruptly. Coatings inside cylinders with silicon-oxide (SiO_2), iron-oxide (Fe_2O_3), titanium-oxide (TiO_2) and PDCPD aerogels are exemplary shown. The viscosity for the coatings ranged between 0.01 and 30 $Pa \cdot s$ with an expected layer thickness from 100 to 700 μm in a 103 mm diameter glass cylinders.

With the results of the cylindrical coatings a process to coat the inside of the spherical 2 mm ablator capsules is developed. In addition, techniques such as the drying of the aerogel and filling of the precursor solution through the 30 μm fill hole needed to be adjusted compared to the easier cylindrical aerogel layers. Earlier developed techniques which fist manufactured the foam scaffold and then coated an ablator shell on top are not feasible for the thick and uniform ablator targets required by NIF.(51) Consequently a chemistry in a capsule approach is developed which coats the foam scaffold inside the

ablator target. Here I show this process where the capsule gets mounted in a holder to track the fill hole position, the capsule gets filled through a $30\mu m$ fill hole, the fill hole gets temporarily plugged, the gel layer is coated with specially developed coating patterns and the solvent gets removed to have the free standing foam within the capsule.

The development of the custom holders that hold the capsule in a tapered hole and allow simple mounting with the fill hole pointing up is the beginning of the chemistry in the capsule process. Followed by the custom design of pressure differential filling device which achieves the required nL precision to permit accurate layer thickness. In the next step the fill hole is temporary plugged by surrounding the capsule with its own precursor solution without applying pressure to the capsule. Then the most challenging step follows by uniformly coating the inside of the capsule.

This coating is done with three different custom developed rotation devices for the capsule. The most advanced coating is done by a random position machine (RPM) that provides a deterministic, continuous change in orientation relative to the gravity vector thus simulating a true microgravity environment.(10) This can be achieved by a system that uses two perpendicular and independently driven frames. The sphere is mounted in the intercept point of both axes. Thus a puddle of the foam precursor within the hollow capsule will distribute to a homogenous layer. I designed a custom machine to fit the necessary specifications with an accurate control over the motion with a feedback loop and speeds up to 20 rpm; a high temperature resistant setup to cure gels up to 80 °C; a flexible stage to allow different mounting and centering techniques for the capsule. With the guidance of the cylindrical results and computational fluid dynamics (CFD)-simulations special coating paths are developed to uniformly distribute the precursor solution. X-ray images are taken from the resulting capsules to improve the coating patterns. An overview of the PDCPD coatings with different velocities and various ratios of the two axis speed will be analyzed.

In the last step the wet aerogel needs to be dried which is especially challenging through a $30\mu m$ fill hole. The toluene of the PDPCP gels is first replaced by acetone in a custom build pressure cycling setup. The success of the solvent exchange is investigated by infrared spectroscopy which can distinguish between toluene and acetone.

The completely solvent-exchanged capsules are then supercritically dried with liquid carbon dioxide (CO_2). The dried PDCPD foam in the capsules was then filled with liquid hydrgon to check whether the foam survives the capillary forces of the hydrogen in the foam pores.

1.6 Catalytic coatings

The deposition of catalytic layers on structured surfaces such as tubings, fibers, foils, microchannels, honeycombs etc. generated many deposition techniques in the past to increase the catalytic efficiency of reactors.(17, 62, 63) With improved catalyst and sol-gel design the limiting factors like heat and mass transfer as well as layer crackability and thickness limits were reduced.(38, 39) An overview about the most common deposition techniques can be found in Valerie Meille's review.(62) Here, I focus on a sol-gel coating technique which bases on the rimming state coating developed for the ICF target development. Instead of glass vials which I used to validate the coating predictions in the ICF section I am using stainless steel tubing since the reactor requires good heat transfer and robustness.

As possible catalysts different Aluminium-Iron-Oxide sol-gels are characterized to validate the coating properties, layer adhesion and robustness during calcination. In general iron is known for its reactivity in respect to water and oxygen which hampers the catalytic activity. In a reducing athmosphere like during Fischer Tropsch synthesis iron's reactivity is beneficial to convert gases to liquid fuel.(46) Current Fischer-Tropsch micro-structured reactors which consist of a tube with a layer of catalyst offer a better efficiency than other reactor designs because mass and heat transfer resistances are negligibly small.(38) The limit of this reactor design is the thin layer of catalyst on the reactor wall that drastically reduces the productivity regarding the reactor volume. Sol gel coatings enable thicker porous layers to improve the reactor productivity.

Sol gel coatings are already widely applied for corrosive protection but are still rare as catalytic coatings.(39, 91, 108, 117) As corrosive protection sol gel coatings are usually only 0.2-1 μm thick and for catalytic applications thicker porous coatings

are desired.(62, 108) Currently most coatings are based on a porous monolith which gets washcoated in a catalytic suspension. The washcoating is about 10-200 μm thick and the surface area is defined by the monolith.(62) Additionally the correct particle size in the suspension is important to adhere to the surface and to uniformly coat all pores in the monolith without plugging them.(62) In contrast aero- and xerogels can be exceedingly active products with their high surface area and tunable simple incorporation of promoters and stabilizers as well as adjustable pore structure. (2) An additional benefit of a flexible porous gel network is that thermal expansion mismatches between the surface and the coated layer can be compensated to mitigate cracks in thick films. Here, I am depositing an up 50 μm thick porous iron sol gel layer with aluminium as support and structural promoter directly on stainless steel tubing.(67)

1.7 Diamond targets

Diamond has emerged as a promising material for high-energy-density physics and inertial confinement fusion experiments because of its high density, robustness, chemical inertness, adjustable grain-size and roughness and its high purity.(9, 20, 37, 82, 109) It is of high importance for ICF targets to determine the diamond density, purity and grain-size to understand the physical condition of diamond under extreme confinement.(11) The resulting equation of state (EOS) tables are required to tune the shape of the laser pulse which hits the ICF target. Here I am characterizing six different samples which were grown under different conditions to achieve various grain-sizes.

The grain-size of thick diamond films is generally controlled by the re-nucleation rate.(111) Here the feed-gas ratio of hydrogen and methane is controlled to introduce nanocrystallinity. Five different samples grown in a microwave-plasma-assisted-chemical-vapor-deposition (MPCVD) reactor are characterized with scanning electron microscopy (SEM), atomic force microscopy (AFM), electron backscatter diffraction (EBSD), transmission electron microscopy (TEM), x-ray diffraction (XRD), white light interferometry (WLI), stylus roughness measurements, Archimedes density measurements, Vibrometry Young's modulus measurements, elastic recoil detection analysis (ERDA), Fourier transformed infrared spectroscopy (FTIR), Raman measurements and Soft X-ray Absorption Near Edge Structure (XANES). For one additional sample the

re-nucleation conditions during MPCVD is alternated to grow stacked layers of micro- and nano-crystalline grains. This sandwich sample is characterized with SEM, TEM and density measurements. With all these techniques described above the grain-size, roughness, crystallite orientation, density, Young's modulus, hydrogen content and sp^2 hybridized carbon content are obtained and compared to existing values in the literature for thin films grown in hot-filament CVD reactors.(82, 112)

The motivation of this work is to smoothen the surface while keeping the density of the material high. The higher the density of the ablator target the thinner the ablator shell can be which allows one to reach higher pressures. The roughness is important for the production of ICF targets that require a smooth surface. It is desirable to achieve the smooth surface by nanocrystalline diamond growth to eliminate the expansive polishing step. In one of the samples characterized here the growth conditions between nano-crystalline- and micro-cystalline- diamond were alternated to aim for the high density of microcrystalline diamond with the smooth surface of nanocrystalline diamond.

2

Requirements

2.1 Foam layers for targets

Initially R.A. Sacks suggested to define the shape of the cryogenic fusion fuel by using a foam layer as a scaffold for the liquid DT-fuel.(88) This is still a potential application for future Laser-Inertial-Fusion-Energy (LIFE) power plants that require about 15 target shots per second.(66) To shoot 1.3 million targets per day the target has to be produced cost-effective.(34) Currently the DT-layer is condensed into the ablator shell and grown from a single seed crystal. This process takes upto 18 hours and is constantly under observation to ensure the quality of the single crystal since grain boundaries would roughen the surface.(53) The production of a rigid foam as scaffold within the ablator shell would dramatically shorten this process and automated mass production of the DT-fuel layer would be more likely. The foam-layer would act as an about 150 μm thick sponge and suck up the liquid fuel and the aerogel would define the distribution of the fuel. Whether the DT-fuel will be used in the liquid state or as cryogenic fuel is still under discussion. Even for the cryogenic fuel rough grain boundaries could be avoided because the growth of the grain boundaries is reduced by briefly freezing the fuel before the shot. The process of manufacturing targets with foam- layers potentially reduces the costs for target production fundamentally and makes LIFE more likely. Thus, the ingredients for the foam-layer need to be abundant and low priced.

Current NIF and Omega (Laser facility in Rochester, NY) targets require dopants in close contact to the fusion fuel. The atomic number of these dopants needs to be

between silver and iodine to measure the temperature by its emission spectra during the target implosion. The ideal foam has this dopant incorporated in the foam structure and the foam density is low enough ($< 30\frac{mg}{cm^3}$) that it does not interfere with the fusion process. Table 5.1 gives an overview of the different target requirements. The major differences between the Omega and NIF targets are the laser power, target size and different shot configurations. The Omega target is shot in the direct drive configuration which means that the target is directly hit by the laser where asymmetric laser light adds additional shock non-uniformities. The indirect drive requires higher laser power; the laser hits the capsule indirectly which leads to a more uniform target implosion. Consequently the indirect drive configuration should be able to tolerate more ablator, foam and ice-layer non-uniformities.

To mitigate foam non-uniformities it is essential to have a machine-able, deformable or

requirements	**direct drive Omega**	**indirect drive NIF**	**indirect drive LIFE**
shell diameter [mm]	0.8-0.9	2	4
foam thickness [μm]	50-120	15-30	150
foam density [$\frac{mg}{cm^3}$]	50-250	<30	<30
foam composition	mostly resorcinol-formaldehyde	pure CH_x + dopant	pure CH_x
ablator thickness [μm]	1-5	80-150	100
ablator material	glow discharge polymer (GDP), polyvinylphenol	GDP, beryllium, diamond	diamond
reference	(8)	(8)	(66)

Table 2.1: foam requirements - Overview of the foam requirements for different laser facilities

a coat-able material to build a foam capsule. The possible low atomic number materials (upto 6 carbon) for foams are limited by their surface finish, pore-size and strength. On the one hand the material needs to support the liquid DT-fuel without collapse and on the other hand it is important to produce surfaces and concentric foam shells that mitigate the effect of shock non-uniformities. Simulations revealed that the foam

microstructure only has minimal effect on the target performance as long as the void spaces/diameter are less than 0.5 μm.(15, 41)

2.2 Foam layers for catalytic applications

The fundamental requirement for the efficient application of catalytic materials is a good control over the dispersion of the catalytically active material and the porosity, i.e. mass transport within the catalytic bed. So called catalytic washcoats such as in the automotive converter consists of a mixture of an inexpensive support material and the active catalyst (Platinum, cerium oxide etc.). These mixtures are then applied as a coat from a slurry. Even though these are well established routines they, in particular, lack control over the porosity of the applied catalytic coating. Sol-gel chemistry derived catalytic coatings on the other hand provide a great potential for controlling pore sizes and thus mass transport on a wide scale.

One particular interesting catalytic material is iron and iron oxide. This material is employed as the catalyst in the so called Fischer-Tropsch catalysis.(46, 67) In its reduced form it is also the active catalyst in the Haber-Bosch catalysis.(99) Iron and its oxides are thus prime catalytic materials.

In order to be applicable as catalytic coatings these sol-gel derived foams have to sustain high temperatures up to 400°C and mechanical shock, without delamination. Foam layers with thicknesses on the order of micrometers inside of stainless steel tubes are desired for Fischer-Tropsch synthesis.

2.3 Diamond ablator

The diamond ablator requires an excellent smoothness, sphericity, material uniformity, high-density and a low-cost production. A smooth inner- and outer surface finish, a uniform material as well as a good sphericity are important to mitigate instabilities during confinement and consequently increasing the implosion stability. The main advantage of diamond over other low atomic number ablator materials is its much

higher density that results in a thinner ablator that absorbs more radiation and thus allows one to reach higher pressures (density of beryllium $1.85\frac{g}{cm^3}$, plastic $0.8-2.2\frac{g}{cm^3}$, diamond $3.52\frac{g}{cm^3}$). Similar to the price sensitivity of the foam layers the diamond-ablators need to be produced at low cost for a LIFE power plant as well.

3

Prior Art

3.1 Nozzle and emulsion techniques

In 1987 R.A. Sacks proposed the idea to use foam shells as surrogates to manufacture cryogenic spherical D-T shells.(89) The fabrication of thick D-T fuel layers in a spherical geometry was not feasible at this time and gravitational slumping was believed to be a major challenge to produce these targets. The basic foam target requirements have not changed since Sacks proposed the wetted foam targets. He suggested small pores, a low density, low atomic number material and a rigid material that survives the wetting of liquid fuel and does not interfere with the fusion process. Shortly after Sacks published his wetted foam target idea N.K Kim et al. described the first approach to produce such wetted foam targets.(51) He used a dual-nozzle technology to produce aerogel foam targets. The technique is schematically shown in Fig. 3.1 and is similar to blowing bubbles. The droplet formation with the precursor solution occurs between the inner and outer nozzle. The inner nozzle supplies the inside of the foam bubble with nitrogen while the bubble is dropped into a highly basic gas where the gelation occurred quickly. The resulting rigid gel bubbles were super-critically dried. The dried capsules had a 300 μm thick wall, an outer diameter ranging from 1.2 to 1.4 mm and were made out of silica aerogel. The rheology, stoichiometry of the reactant solution, gas mixture, sphericity, wall-uniformity, morphology and geometry were further characterized and improved by other groups leading to better foam targets.(14, 49)

To improve sphericity M. Takagi suggested an emulsion method where the precursor

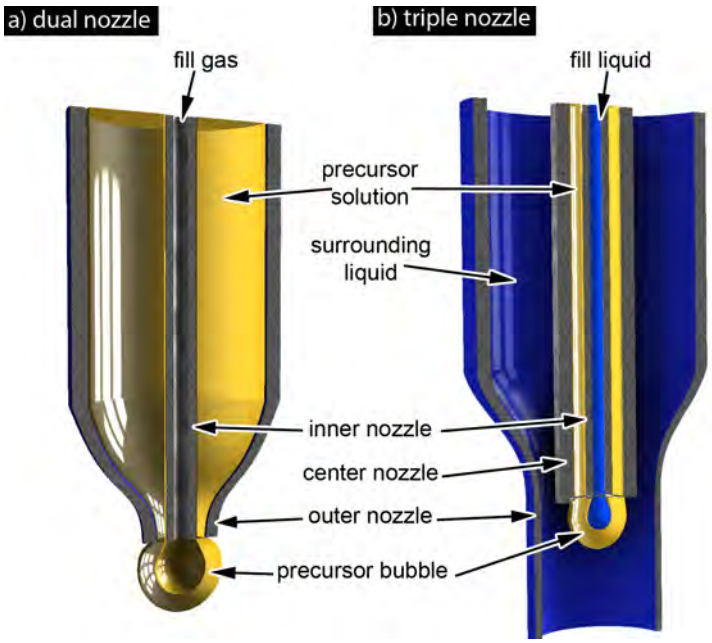

Figure 3.1: nozzle techniques - a) the initial two nozzle technique is similar to blowing soap bubbles where the aerogel precursor solution is bubbled with a fill gas; b) with a triple nozzle technique and by matching the densities of the three liquids a better uniformity can be achieved. The aerogel precursor bubble gets filled with an unmiscible fill liquid and surrounded with an unmiscible surrounding liquid

is not miscible in another solution creating an emulsion.(102) In detail he fist created small bubbles of water in the oil based precursor to make a water/oil emulsion. These bubbles were transferred into another water bath leading to a thin layer of oil-precursor between an inner core of water and a surrounding water bath. Then the water of the bubbles was exchanged by ethanol. In M. Takagi's process the capsules were made out of xerogel which means the bubbles in ethanol were dried in air and the structure and network of the material deforms. He achieved good sphericity by matching the density of the oil and water and manufactured capsules with thin walls of 2-14 μm at a relative small diameter of 500 μm.

In 1994 T. Norimatsu combined the dual-nozzle technique with the emulsion method by using a triple-nozzle technique.(54) Figure 3.1b) shows how the precursor bubble is created between the inner- and center-nozzle. In addition to the two nozzle-technique this bubble is surrounded by liquid. To achieve concentricity the liquid of the inner core, the precursor and the surrounding liquid need to have the same density to avoid buoyancy. The bubbles created with the three nozzle technique are directly deposited into a warm bath of solution to allow polymerization of the precursor. After the solvent exchange the gel bubbles were super-critically dried in carbon dioxide. The resulting foam capsules had a wall thickness of 10-15 μm, about 1500 μm diameter and had a density of about 45 $\frac{mg}{cm^3}$ out of trimethylolpropane trimethacrylate. Norimatsu compared his new three-nozzle technique, he called it dual orifice, with the emulsion method and he achieved higher reproducibility in diameter and wall thickness.

The triple-nozzle technique and the emulsion method are still the most common techniques used today to manufacture foam bubbles for target applications. These techniques were further developed for recorcinol-formaldehyde-, devinylbenzene-, phloroglucinol-formaldehyde-, polystyrene- and polymethylmethacrylate-aerogels.(54, 78, 102, 114) The limiting capabilities of these foam bubbles are the achievable diameter, wall-thickness and density. Usually the resulting targets were about 500-1000 μm in diameter with a wall thickness of about 20-150 μm and density often above 100 $\frac{mg}{cm^3}$. The high density was required because the foam targets were not robust enough to keep sphericity during the drying process and handling, thus showing deviations from roundness.

In addition, most precursors did not meet the requirement of being a pure CH-aerogel.

To achieve a permeation barrier for the DT-fuel the final free standing foam capsules are coated with a glow-discharge-polymer from the outside or dip coated with another polymer.(72, 73) The basic requirements for the permeation barrier are good fuel retention, surface finish and strength as well as a desired cryogenic behavior. The surface finish is obviously important for the target performance to keep the target as smooth and spherical as possible.(79) The strength is defined by the required ablator characteristics and might be required to withstand the pressure of the liquid fuel.

3.2 Chemistry in a capsule

Chemistry in a capsule means the entire process of coating and formation of the gel layer by sol-gel chemistry, including the drying of the foams, inside an ablator capsule. In the beginning this process contained the three stages of filling, coating and subsequent drying which are still part of the current procedure in Fig. 5.1. The first step started with filling diamond capsules with precursor solution. The capsules had a fill hole of about 200 μm diameter that was positioned upwards. Schematically Fig. 3.2a) shows a syringe filled with 30 $\frac{mg}{cm^3}$ Dicyclopentadiene (DCPD) precursor solution, placed in a syringe pump and tubing connected to a glass capillary. The glass capillary was controlled by a xyz-stage to inject the capillary in the capsule. The insert shows a real diamond capsule during filling.

The syringe pump was intended to control the fill volume of the capsule. The initial liquid immediately plugged the gap between the fill hole and the glass-capillary. Consequently the air did not vent and a higher pressure was necessary to fill the capsule. Accurate control of the fill volume was not achieved and was only visually controlled. The first capsules were completely filled with PDCPD precursor and gelled stationary. Figure 3.2b) shows a complete fill with 30 $\frac{mg}{cm^3}$ PDCPD after supercritical drying and vapor phase iodine doping.

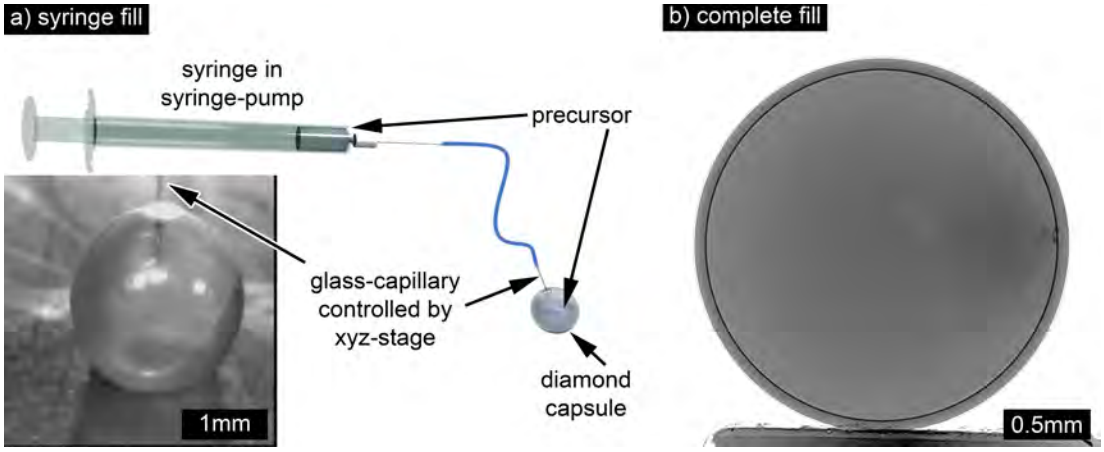

Figure 3.2: syringe fill - a) the capsule gets filled with precursor solution by injecting a glass capillary into the capsule and pumping liquid with a syringe pump through the capillary. The capillary usually plugs the fill hole and pressure within the capsule builds up during filling which makes accurate filling impossible; b) a complete filled and dried 30 $\frac{mg}{cm^3}$ PDCPD aerogel in a capsule filled with the syringe fill method and doped with iodine vapor

3.3 Tuning rheological properties of aerogel

Successful coatings require the precise understanding and adjustment of the sol-gel rheology. Three different techniques are currently used to adjust the sol-gel transition and the viscosity *vs.* time behavior of aerogels. A pre-polymerization technique by S. Letts describes the pre-aging of a resorcinol-formaldehyde (RF) aerogel.(57) The sol gel transition does not change but the known pre-polymerized viscosity can be used to coat at predictable conditions. A similar approach is used by R. Paguio who suggest to start with higher viscous solvent. (80) He added a styrene-butadiene-styrene block copolymer to oil based RF aerogel which raised the viscosity of the oil. F. Ito discribed the first approach which changes the viscosity over time behavior and the viscosity at the sol gel transition by using a linear polymer instead of using a cross linking reaction.(48, 114) He exchanged the cross linking RF gel by a linear polymer phloroglucinolcarboxylic acid and formaldehyde (PF) aerogel.

3.4 Catalytic coatings inside cylinders

Current coatings inside tubing are usually applied by dip coating and require special exhaust pipes and adjustments of the withdrawing velocity to keep the layer thickness constant.(62, 76, 83) To my knowledge the coating by the rimming state for catalytic layers has not been done before. Meile's review gives a good overview about current catalytic sol-gel coatings such as aluminum oxide and silicon dioxide on glass which are usually done for smaller diameter micro reactors with thin layers up to 10 μm thickness.(62)

3.5 Diamond ablator targets

Ablator films are required to absorb as much energy as possible to compress the fusion fuel to ignition. Instabilities like the Rayleigh-Taylor instability and shell irregularities can occur and influence the symmetry of the implosion. In addition a too strong single laser pulse would create entropy in the fusion fuel making fusion less likely. Especially optimized laser pulses and uniform shells mitigate these possibilities. Diamond is one of the possible candidates that performs well for these requirements.(9) In addition the high density of diamond allows absorbing more energy than most other ablator targets.

The production of spherical diamond ablator shells is done with a chemical vapor deposition process.(9) Figure 3.3 shows the schematic production process of these diamond targets. In the first step the silicon mandrels are agitated in diamond suspension and then placed on a tilted disc in the diamond coater. The mandrels randomly move under rotation on the disk and are coated by microwave-plasma-chemical-vapor-deposition. For high density target shells the coating parameters are micro-crystalline diamond parameters, with about 1 % methane and 800° C. The coating is usually done in a cost-efficient batch process and after the desired layer thickness is achieved (about 2 μm/h) the capsules at these high densities have a rough outer surface finish. Currently a time consuming step of polishing the shells is required to meet target specifications. The mechanical strength of diamond only allows diamond to be polished with another diamond. For this process the capsules are placed on another disc with circular V-groves and a rotating diamond disc is placed on top of the capsules. The polished capsules can achieve as low as 10 nm surface finishes with high-precision

grinding discs. In the next step a hole is drilled by laser into the diamond capsule. This hole is required to remove the silicon mandrel and later this hole will be used as fill-hole. The laser-drilling only produces volatile vapors and no additional debris gets into the capsule. In the final step the silicon mandrel is etched out of the diamond shell. After a few days of ultrasonic etching only the clean diamond shell is left. The inner surface finish is determined by the silicon mandrel in beginning and as low as 10 nm rms roughness is feasible.

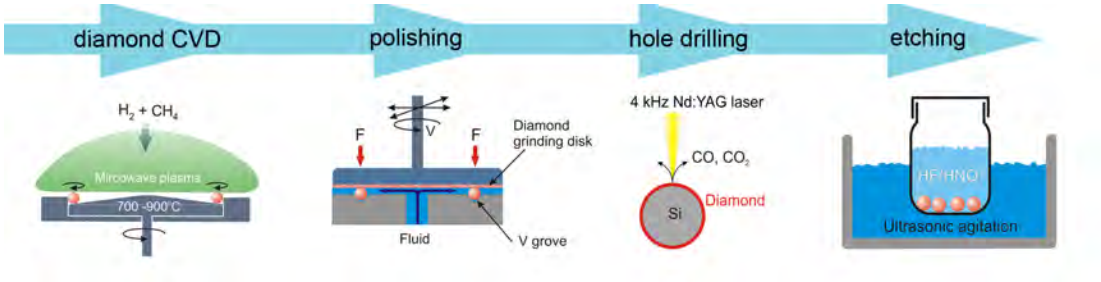

Figure 3.3: Schematic diamond capsule production process - in the first step the diamond gets coated with microwave assisted chemical vapor deposition on silicon mandrels which randomly rotate on a tilted disc. Followed by a time consuming polishing step where the diamond capsules get polished with another diamond disc. In the next step a hole is laser drilled into the capsule to enable the mandrel removal and later capsule filling. The capsules get agitated in a strong acid to etch out the silicon mandrel in the last step. The diamond is chemically inert and does not get damaged by the etching (9)

4

Diamond targets

Diamond with its high density is a promising target material. The morphology, physical and chemical properties are characterized in dependency to their grain size to achieve dense carbon with a smooth as grown surface finish which eliminates the expansive polishing step of regular diamond. The grain size and with it the diamond properties is manipulated by adjusting the methane concentration in the feed gas. For $\geq$ 3% methane in the feed gas an abrupt transition from micro-crystalline to nanocrystalline diamond is observed while the amount of impurities like sp^2 carbon and hydrogen increase. To achieve a smooth as grown diamond and the required dense material a sandwich target was produced where micro-crystalline and nanocrystalline diamond were alternated. The density did not increase as expected but the target performed well in a compression experiment.

4.1 Experimental

4.1.1 Microwave assisted plasma chemical vapor deposition

The artificial growth of diamond by chemical vapor deposition requires energized feed gases that deposit carbon on a substrate. The most common energy sources are hot filaments, arc discharges and microwave plasmas. The diamond samples characterized here were grown by microwave plasma chemical vapor deposition (MPCVD) in an ellipsoid geometry as described by Füner et. al..(28, 29) In this geometry the microwaves introduced by an antenna are reflected by the ellipsoid reactor and focused on the substrate. Figure 4.1 schematically shows this ellipsoid microwave reactor where the antenna is

the microwave inducing focal point and the substrate the microwave absorbing focal point. The feed gases of the plasma are contained by a bell jar. For the samples characterized here the feed gas contained a mixture of hydrogen (H_2) and methane (CH_4) to control the grain size. With the energy of the microwaves plasma CH_3 radicals, C_2H_2 molecules and atomic hydrogen are produced. The CH_3 radicals are the most probable growth species for diamond while C_2H_2 and atomic carbon only facilitate the growth at very high power.(33) The basic role of the atomic hydrogen is to etch non-diamond phases that can be formed simultaneously with the diamond growth. In addition the hydrogen re-combustion heats the substrate to the required temperature. Silicon wafers were used as substrate in the plasma. To enable the growth of diamond on the silicon wafers the wafers were agitated in a diamond particle suspension before growth. The samples characterized here were grown at an almost unchanged temperature between 830°C and 850°C to grow an about 40 μm thick layer. The CH_4 concentration in the feed gas varied between 2 % and 5 % to change the grain size.

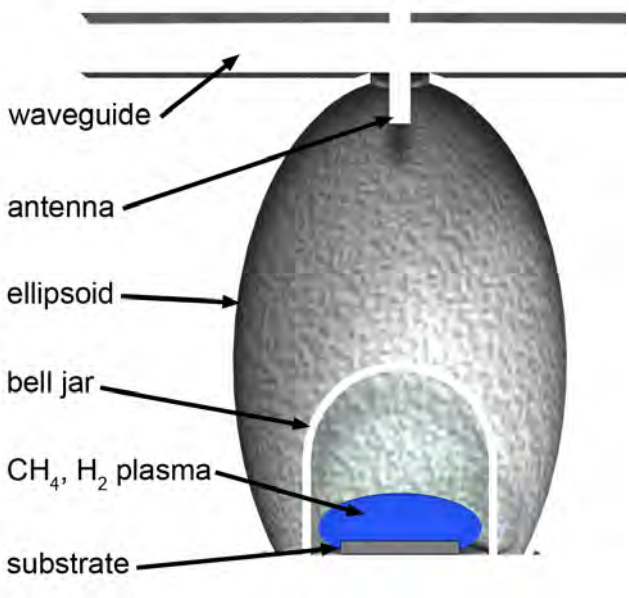

Figure 4.1: Ellipsoid reactor schematically - in an ellipsoid reactor the microwaves get injected through a waveguide by an antenna. The antenna is in the upper focal point of the reactor and the substrate in the lower focal point. Consequently the microwaves create a plasma surrounding the substrate

4.1.2 Surface characterization

Scanning Electron Microscopy (SEM) images from the growth side of the diamond surface were acquired with a Hitachi S-800 and a Jeol JSM-74011f instrument. An acceleration voltage of 2-3 kV was used in secondary electron mode and the images were recorded with the beam perpendicular to the surface. For electron imaging usually a conductive sample is required to prevent charging. Here, upto 20 nm of conductive palladium were evaporated on the sample surface for the low magnification images. For the high magnification images a small uncoated sample was used and placed next to conductive copper to mitigate the charging of the sample. White Light Interferometry (WLI) scans were acquired with a Wyco NT1100 from Veeco with a 50× magnification objective. The appendent software calculated the surface roughness out of the interference pattern from the surface reflections and the reference light. Atomic Force Microscopy (AFM) images were captured on a Molecular Imaging AFM (today agilent technologies). For AFM the sharp tip on a cantilever is used to scan the surface of a sample. The deflection of the cantilever is usually measured by the reflection of laser light on photodiodes. The imaging techniques can be divided into contact- and non-contact-modes. In contact-mode the tip generally is in contact with the surface and a feedback loop always keeps the force on the tip constant. The adjustments to keep the force constant are measured and mapped to calculate the surface tomography. In non-contact-mode the frequency change, usually caused by van der Waals forces, of the oscillating cantilever is measured. The feedback loop keeps the frequency constant by adjusting the tip to sample distance. These distance adjustments give the surface topography. For materials with a high hardness both modes usually give a similar image. Here I used the contact mode with a diamond coated nanosensors tip. The surface tomography and surface roughness were processed with the Agilent Pico Imaging AFM software. In addition to the WLI and AFM surface roughness measurements a stylus Profilometer was used.

4.1.3 Crystallite characterization

The Electron Backscatter Diffraction (EBSD) grain orientation data was acquired with a TexSEM Laboratories (TSL) Orientation Imaging Microscopy (OIEM) system mounted on an FEI Quanta200 Environmental Scanning Microscope (ESEM). For

EBSD measurements some backscattered electrons of the incoming electron beam are captured by a phosphor screen which converts the electrons in light. The light of the excited phosphor screen shows a diffraction pattern which is recorded with a CCD-sensor. The diffraction pattern of the backscattered electrons is caused by Bragg's law:

$$2 \cdot d \cdot \sin\theta = n \cdot \lambda \tag{4.1}$$

where d is the distance between two lattice planes, θ the scattering angle, n an integer determined by the order given and λ is the wavelength. Constructive inference between the reflected beams on the different lattice planes causes the diffraction pattern. TSL OIM 6 data analysis software was used to generate inverse pole figure maps. Because of the limited spatial resolution $> 300nm$ of the tungsten filament equipped SEM for fine grained specimens only coarse grained samples can be measured with EBSD.

X-ray diffraction is another method to determine the atomic and molecular structure of crystals. The intensity and angle of the diffracted x-ray beams is detected and used to calculate $\theta/2\ \theta$ scans and pole figures. $\theta/2\ \theta$ can be used to determine the purity of the diamond and to calculate the grain size of the material. Pole figures contain the grain orientation. Figure 4.2 shows schematically the difference between $\theta/2\ \theta$ scans measured in reflection and transmission. In transmission the scattering vector is perpendicular to the grains and thus mainly the diameter of the columnar grains is probed. In reflection the scattering vector is parallel to the columnar grains which mainly determines the height of the grains.

The X-ray Diffraction (XRD) $\theta/2\ \theta$ scans were measured on a STOE Stadi P focusing diffractometer equipped with Cu sealed tube and a bended Ge 111 monochromator providing Cu Kα_1 radiation. Measurements were performed in the 2 θ ranges of 20° - 142° with a step width of 0.03° - 0.05° and a 1 mm detector slit. The X-ray diffraction texture measurements (pole figure measurements) were performed on a Panalytical MRD diffraction system with Cu X-ray radiation in a point focus setup. At the primary beam side, a polycapillary X-ray lens with a divergence of 0.3° and a Ni filter for the suppression of Cu Kβ radiation was used. The size of the beam spot was limited to $2{\times}2\ mm^2$ or $1{\times}1\ mm^2$ by a crossed slit assembly. On the detector side, a parallel plate

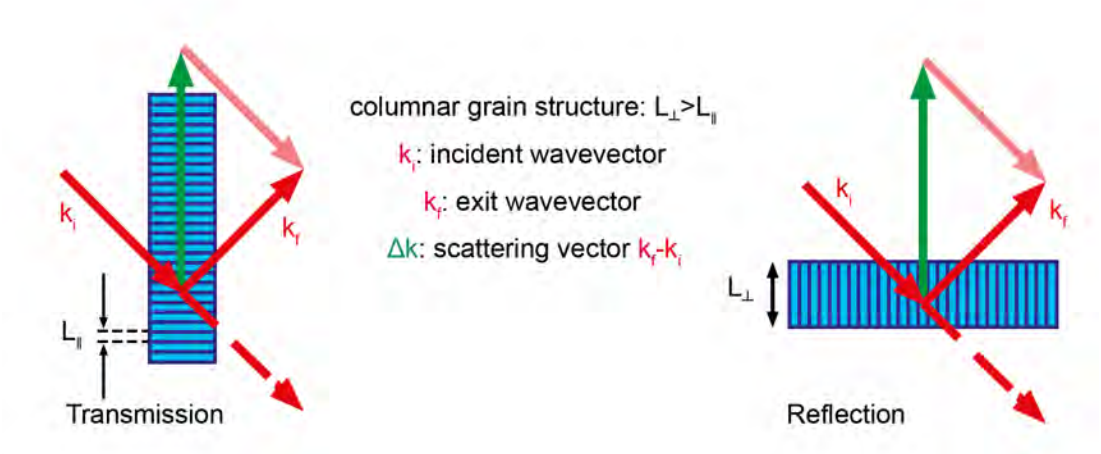

Figure 4.2: Difference between XRD in transmission and reflection - in transmission XRD the scattering vector probes perpendicular to columnar grains which means that the resulting grain size should be smaller compared to reflection; in reflection the scattering vector is parallel to the grains

collimator and a 0.04 rad Soller slit was used.

The gain-size was estimated by the Scherrer equation after deconvolution where optical diamond was used as reference and additionally with the software "Stoe WinXPOW size" version 1.0. The grain size determination is limited to small grains around 100-200 nm since coarse grains do not correlate with the peak broadening.(43) The Scherrer equation predicts broader peaks for smaller grains:

$$t = \frac{K \cdot \lambda}{B \cdot \cos\theta} \tag{4.2}$$

where t is the grain size, K a shape factor between 0.89 and 094 for diamond, B is the full-width-half-max at the θ peak and λ the wavelength of the x-rays.(43, 92) The K constant is dependent on the geometry of the grains where 0.94 is for spherical grains.(55) The values calculated "by hand" with the Scherrer equation were very similar to the WinXPOW software values. Because of this similarity I am using the software values here. Additional deconvolution of size and micro strain broadening with a Williamson Hall analysis did not yield conclusive results and a computational diffraction peak simulation with Rietfield refinement was not performed.

The Transmission Electron Microscopy (TEM) characterizations were performed in a Philips CM300-FEG microscope, with an acceleration voltage of 300 KeV and a field emission gun with an extraction voltage of 4.2 eV. The image contrast is generated by the absorption of electrons or wave interactions in the nm- thick sample. Bright-field, dark-field, and selected area diffraction (SAD) techniques were applied to investigate the grain size information of the as-synthesized materials. The TEM samples were etched with an oxygen plasma from the nucleation side to electron transparency using an etch mask which had about 3×2 mm windows. One of the windows was removed and transferred to a TEM grid. No ion-beam thinning procedure was applied. The average grain-size of the TEM, SEM and EBSD images was measured manually by measuring the longest and shortest distance of at least 20 grains. The values shown are the average of all measurements with the "error bars" showing the entire range measured.

4.1.4 Elemental composition

The sp^2- and sp^3-hybridized carbon content are characterized by Soft X-ray Absorption Near Edge Structure (XANES) and Raman spectroscopy. The hydrogen content of the diamond samples is determined with Elastic Recoil Detection Analysis (ERDA) and Fourier Transformed Infrared Spectroscopy (FTIR).

XANES spectroscopy measurements were performed at beam-line 8.0 at the Advanced Light Source at Berkeley National Laboratory and at Stanford Synchrotron Radiation Lightsource at the SLAC National Laboratory Accelerator Laboratory. In XANES measurements a x-ray photon excites a core shell electron. An intense tunable soft x-ray source, usually a synchrotron, is required to excite the core shell electron in the vicinity of its absorption edge. The detection of XANES spectra is divided into three different measurements: in total-electron-yield (TEY) the emitted photoelectrons are measured, in total-florescence-yield (TFY) photons are detected which are emitted after the vacancy of the photoelectron is filled by a higher energy level electron, and Auger electrons are detected when an emitted photon gets absorbed by another electron and this electron leaves the atom. Auger electrons are the most surface sensitive measurement followed by TEY, and TFY is more bulk sensitive.(106) The high surface sensitivity makes Auger measurements extremely difficult for diamond because of

residual contaminations on the surface. Here I focus on TEY and TFY measurements that still require an in-depth cleaning of the surface to remove contaminations which was done by heating the surface in vacuum and plasma etching.

For Raman spectroscopy a 457.94 nm wavelength Ar+-laser was used for optical excitation of the carbon atoms. The excited atom moves from the ground state to a virtual energy state. A photon is emitted when the molecule relaxes and returns to a different vibrational energy state. The energy difference between the original ground state and this new state leads to a shift between the excitation wavelength and the emitted wavelength. This shift can be interpreted to distinguish between sp^2- and sp^3-hybridized carbon.(24) The scattered light was recorded using a triple monochromator (Triplemate Spectrograph 1877, SPEX Industries) equipped with a liquid nitrogen cooled charge coupled device detector array SPEC-10:100B from Roper Scientific Inc..

ERDA is used to profile the hydrogen content in about the first 500 nm of the sample.(23) The same setup as for Rutherford backscattering (RBS) can be used but for ERDA the detector needs to capture the forward scattered ions. Compared to RBS ERDA is more sensitive to light elements like hydrogen after they got hit by an incident ion beam. The sample normal direction was tilted to 70° with respect to the incident beam direction, and hydrogen atoms recoiled at 150° were measured with a surface barrier detector covered with a 13 μm thick carbon foil. Analysis of ERDA spectra was done with RUMP code (22) with scattering cross sections from Ref. (6). A 4 MV ion accelerator module at Lawrence Livermore National Laboratory (model: 4UH by NEC) was used to generate 3 MeV $^4He^+$-ions.

In addition to the scattered light measured by Raman spectroscopy an absorption measurement was done with Fourier transformed infrared spectroscopy (FTIR). To determine the hydrogen content and bonding to carbon the absorption around 3000 – 2800 cm^{-1} is characterized here. In contrast to the ERDA FTIR measurements are in transition and thus capture the entire sample depth. For details about infrared spectroscopy please see below in the chemisty-in-a-capsule chapter 5. The FTIR measurements of the diamond samples were performed with a Digilab UMA 400 instrument.

4.1.5 Mechanical properties

The density of the small light weight diamond samples was determined with a custom build Archimedes principle experiment. With a Mettler Toledo XP56 microbalance with a readability of 1 μg the samples were measured in two different density environments. The first measurement was performed in air. For the second measurement in liquid I needed to ensure that vapors of the liquid did not condense on various parts of the balance. Instead of water that did not fulfill this requirement I used a perfluoro-compound. The Acros perfluoro-compound FC-40 (also called Flourinert by 3M) showed good wetting of the diamond samples and did not condense within the balance. For the measurement of the sample in FC-40 a sample-basket connected to the transducer of the balance was submerged into the FC-40. With the known densities of the air (ρ_{air}) and FC-40 (ρ_{FC-40}) as well as the measured weights in air (m_{air}) and FC-40 (m_{FC-40}) the density of the sample was calculated:

$$\rho_{sample} = \frac{(m_{air} \cdot \rho_{FC-40}) - (m_{FC-40} \cdot \rho_{air})}{m_{air} - m_{FC-40}} \tag{4.3}$$

The density of F-40 was first calculated by using an optical diamond with a known density of 3.52 $\frac{g}{cm^3}$. The setup was then verified by determining the density of gold and comparing it to its actual density 19.32 $\frac{g}{cm^3}$.

The Young's modulus was determined by vibrometry with a Polytec MSA-500 instrument. The diamond sample is clamped as a cantilever which means it is fixed on one side and the other side is free standing. The oscillation of the cantilever is measured by the Doppler effect of laser light which gets reflected from the cantilever. The Doppler shifted signal is then processed to calculate the resonance frequency of the different modes of oscillation. The actuation of the diamond cantilever is done by a piezo shaker. With the frequency obtained and the known rectangular beam geometry plus density the Young's modulus (E) can be calculated out of the Euler-Bernoulli beam theory:

$$E = \frac{f_n^2 \cdot L^4 \cdot \rho}{h^2} \cdot \frac{48 \cdot \pi^2}{\lambda_2^4} \tag{4.4}$$

Where f_n is the resonance frequency at mode n, L the length of the free standing cantilever, ρ the density of the beam, h the thickness of the beam and λ the eigenvalue corresponding to the mode (n(1)=1,875; n(2)=4,694; n(3)=7,854 and for $n > 3$: $(2n -$

1)$\frac{\pi}{2}$).(86, 87) The modes are the different oscillations which superimpose each other. Here two measurements with two different cantilever lengths for each experiment were performed. The Young's modulus was calculated for each mode separately and the results here are the average of all measurements and the "error bars" show the entire range measured.

4.2 Results and discussion

In the first step the grain size and surface roughness of the five diamond samples is characterized. In the next step the sp^2-hybridized carbon, the hydrogen content, density, Young's modulus and possible textures in the samples are investigated. In the last step the results are used to grow sandwich targets which alternate the different growth mechanisms characterized here. The idea of sandwich targets is to have a smooth surface while having a high density of coarse grains, as mentioned in the introduction on page 13. To keep the results clearly arranged I did not distinguish between nano- and regular-seeded diamond samples. AFM, SEM and roughness measurements did not show any difference between nano-seeded and regular seeded diamond. The five samples here were grown roughly at the same temperature between 830°C and 850°C and the CH_4 concentrations were: 2 %, 2.5 %, 3 %, 4 % and 5 %.

4.2.1 Surface roughness, grain -size and -orientation

The change in surface morphology of the diamond samples is shown in Fig. 4.3. The sizes of the crystallites decrease with increasing CH_4 concentration. In the 2 % CH_4 sample the crystallites are clearly visible with an estimated average size range of about 0.6-8.8 μm, Fig.4.3a). The grains of the diamond grown with 3 % CH_4 in Fig. 4.3b) are still visible at the same magnification while in Fig. 4.3c) of the 5 % diamond only cauliflower like morphology is visible. Further magnification in the insert of Fig. 5.3c) shows this morphology and the roughly estimated grain-size range is around 5-50 nm. Figure 4.3d-f) shows AFM images of the same samples shown in Fig. 4.3a-c). The images have the same scale bar as the SEM images and the trend of decreasing grain-size with increasing CH_4 concentration is confirmed. The WLI measurements in Fig. 4.3g-i) sample a bigger area. The 2 % CH_4 sample in Fig. 4.3g) shows a few red peaks which are between 2.5 and 3 μm high. The 5 % sample has peaks up to 300 nm high.

The WLI images in Fig. 4.3g-i) prove the peak heights of AFM results. In addition to WLI and AFM measurements a simple stylus roughness measurement was performed that compared well with the WLI results. Further SEM micrographs are shown in appendix A.

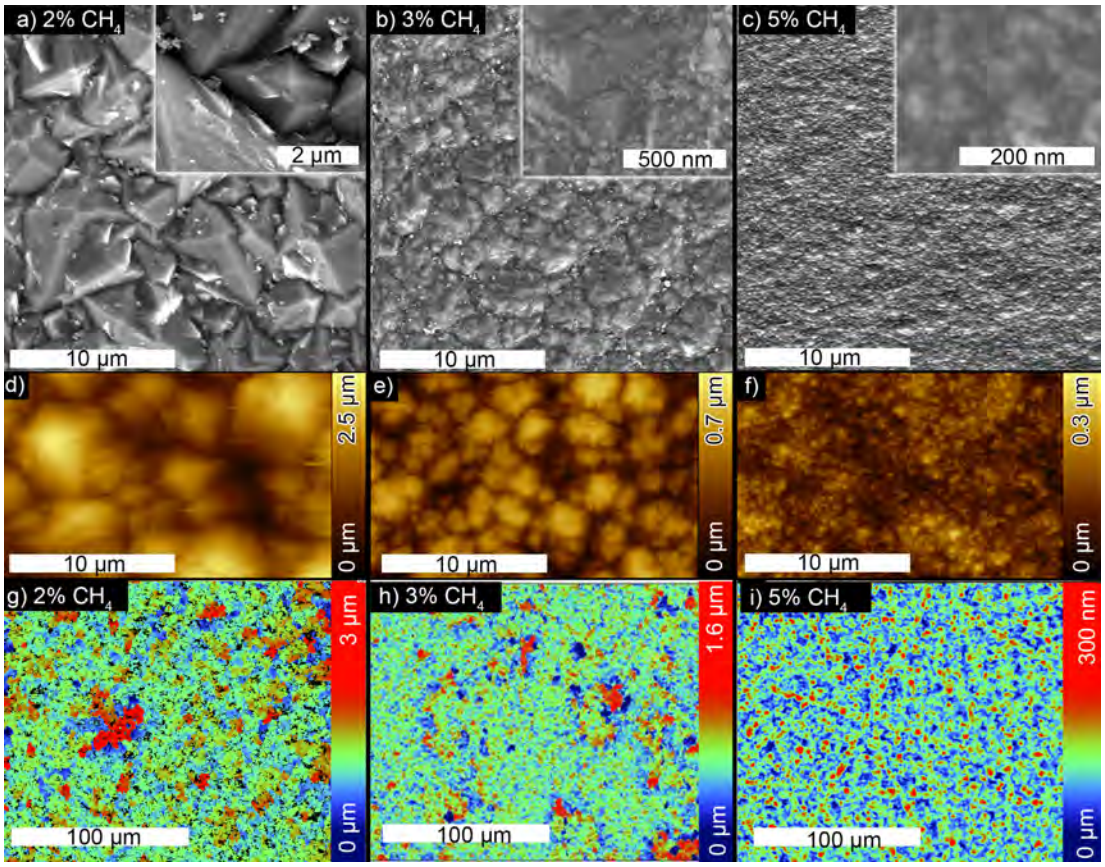

Figure 4.3: Surface morphology - the surface morphology of three different micro- and nanocrystalline diamond samples grown at different methane concentrations and characterized by SEM (upper row), AFM in contact mode (middle row) and WLI (lower row); the roughness of the samples decreases clearly with increasing methane concentration from left to right. The peak to valley roughness in the WLI and AFM measurements agree with each other except of for the 3 % methane sample where the WLI captured a bigger area with some higher peaks. The crystallites are visible in the SEM images and their size can be estimated. The root mean square roughness values are in table 4.1

To accurately determine the grain size EBSD, TEM and XRD were used. The resolution of the EBSD measurement is limited to the bigger grained diamond samples

which are the 2 % and 2.5 % CH_4 samples. This means that the average grain size of the other samples is below 300 nm. The EBSD images of these 2.0 % and 2.5 % CH_4 samples are shown in the inverse pole figure orientation map in Fig. 4.4a-b). The grain orientation seems to have a slight preferred [110] orientation as a color comparison with the plane orientation map in the lower center between the two EBSD maps shows more green. The average size of the grains calculated out of the inverse pole figures is between 0.6-5.2 μm for the 2 % CH_4 sample and 0.2-3.5 μm for the 2.5 % CH_4 sample. The high resolution TEM images in Fig.4.4c-d) clearly show the grains of the 3 % and 5 % CH_4 sample. The average grain size of the TEM image is between 4 and 40 nm for the 3 % CH_4 sample and between 5 and 18 nm for 5 % CH_4. Table 4.1 gives an overview of the calculated root mean square roughness values and the measured grain size range.

XRD diffraction $\theta/2\ \theta$ scans were performed in reflection and transmission to guarantee that the columnar structure of the grains is included in the measurements, Fig. 4.5. The Scherrer equation predicts smaller grains for broader peaks but is limited to grains up to 200 nm.(43, 92) A qualitative analysis of the transmission results in Fig. 4.5a) confirms the trend of decreasing grain size with increasing CH_4 concentration. The reflection results are very similar to the transmission results and the qualitative results are confirmed, Fig. 4.5b). Noticeable is that the 400 peak of the reference does not appear in reflection while it is only weakened in transmission and the [220] peak is less pronounced in transmission which indicates a preferred [110] orientation. Compared to the EBSD and TEM results the XRD analysis always revealed smaller grains for micro-crystalline samples since the grains are above 100-200 nm which is the resolution limit of the Scherrer approximation. Further investigation by XRD pole figures indicated that a fiber texture is present which alters the width of the $\theta/2\ \theta$ peaks and eliminates the [400] peak, Fig. 4.5c).

The Pole-figure (Fig. 4.5c) of the nanocrystalline 5 % CH_4 diamond shows a red closed ring that can be attributed to a fiber texture with a [110] fiber-axis. The [110] fiber-texture seems to be unique for the nano-crystalline samples. As comparison Fig. 4.5d) shows the pole figure from a NCD film that was grown under similar conditions on a diamond [110]-single crystal. The discontinuous ring pattern indicates additional

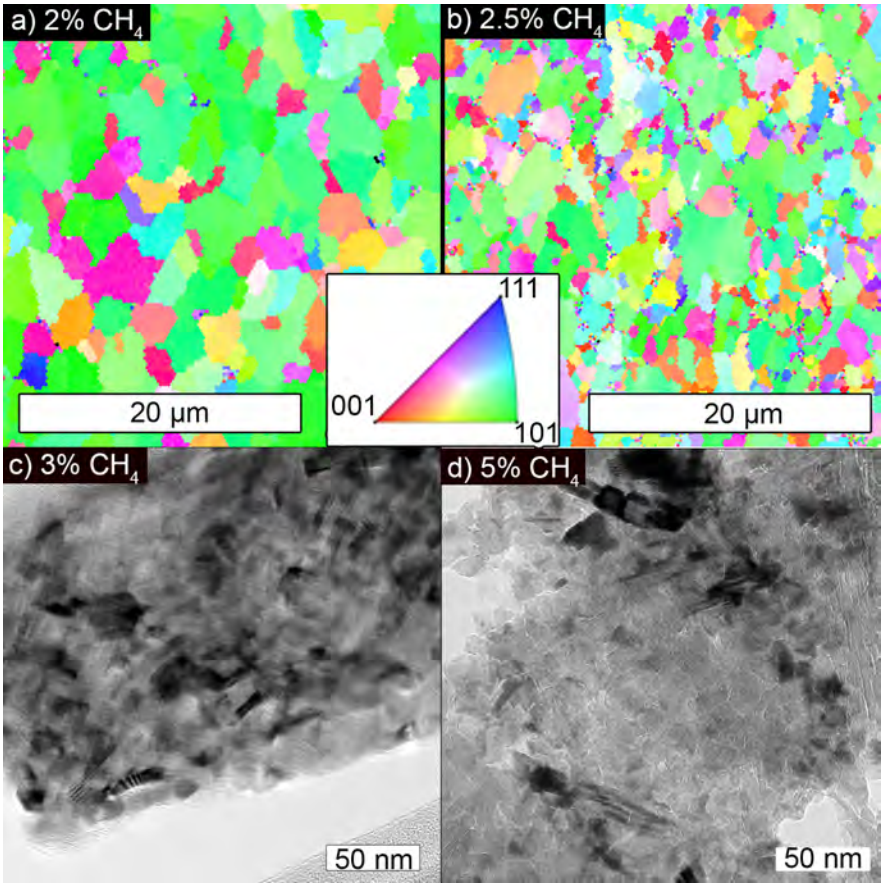

Figure 4.4: Grain size determination by EBSD and TEM - the EBSD inverse pole figure grain orientation maps both show predominant green which can be attributed to a preferred [110] orientation of the grains. a) the average grain size is between 0.6 and 5.2 μm and b) 0.2-3.5 μm for 2.5 % methane; c-d) The average grain size of the grains in the TEM images between 4 and 41 nm for 3 % CH_4 and between 5 and 18 nm for 5 % CH_4

in-plane texture. The EBSD measurement of 2 % and 2.5 % CH_4 concentration diamonds confirmed this preferred orientation, Fig. 4.4a-c).

The surface roughness and grain size dependencies towards the CH_4 concentration are summarized in Fig. 4.6. HED physics experiments require a precise knowledge of the grain-size to understand the physics for EOS calculations. The roughness is important for the production of ICF targets that require a smooth surface. It is desirable to achieve the smooth surface by nanocrystalline diamond growth to eliminate the expansive polishing step. The grain-size as well as the roughness clearly decreased with increasing CH_4 concentration. To better understand the transition from micro-crystalline grained to nano-crystalline diamonds two intermediate samples with 2.5 % and 4% CH_4 in addition to the samples in Fig. 4.3-4.4 are shown in Fig. 4.6. The SEM values are used for further characterization since these values capture all other measured results.

The AFM, WLI and stylus-roughness measurements in Fig. 4.6a) are in good agreement with each other for the nano-crystalline grained samples (4-5 % CH_4). In addition our roughness values of 20-40 nm rms concur with Wiora's and Sharda's value of about 10-30 nm rms.(97, 112) For the micro-crystalline samples with 2 and 2.5 % CH_4 the AFM measurement indicates a rougher surface than the stylus and WLI measurements. Several AFM measurements confirmed this high surface roughness indicating that the stylus tip was not as sharp as the AFM tip and the WLI technique is known to have a limited lateral resolution.(7) The comparison of the three different roughness measurements suggests that the AFM measurements are subjected to the smallest error, see table 4.1.

The grain size information is summarized in Figure 4.6b) where the grain size clearly decreases with increasing CH_4 concentration. The EBSD and SEM results for the 2 and 2.5 % CH_4 are in good agreement with each other while the XRD grain size for the microcrystalline samples is much lower since grains bigger than 100-200 nm cannot be determined by the Scherrer equation.(43) The 2 and 2.5 % CH_4 diamond sample have an average grain size of 2.4 and 2 μm which is characteristic for microcystalline diamond films. The 3 % CH_4 diamond seems to be transitioning to become nanocrystalline as

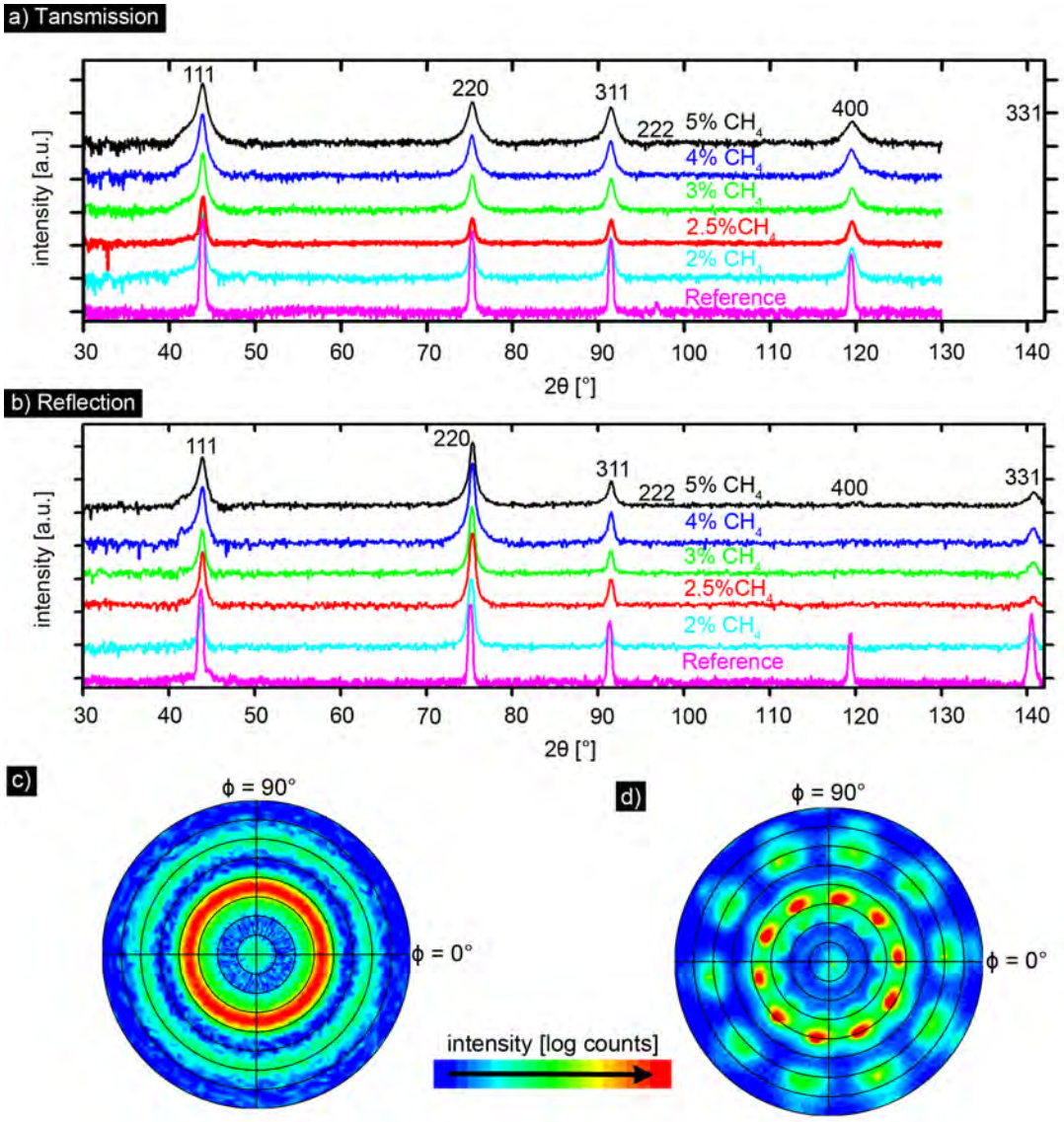

Figure 4.5: XRD $\theta/\ 2\theta$ scans and pole figures - a-b) show the $\theta/\ 2\theta$ plots of the five different diamond samples in transmission a) and reflection b). a) All the peaks of the reference spectrum show up with a slightly lower intensity than the reference peaks. b) The [400] peak does not show up and the [111] peak is smaller than the [220] peak which indicates a preferred [110] grain orientation. X-ray texture analysis of c) 120 μm and d) 30 μm thick NCD samples deposited with 4 % methane on a [100] Si wafer and a [110] diamond single crystal, respectively: The 111 pole figure shown in c) has an intensity maximum that forms a closed ring at a polar angle at 35° with a second smaller intensity maximum at 60° which can be attributed to a [110] oriented fiber texture with random azimuthal orientation (35.2° untwinned, 57° first order twins). The 10-fold symmetry observed in d) reveals a 110 oriented 5-fold twinned nanofiber morphology which is also in registry with the substrate

the big grain size difference (50-500 nm) in the SEM micrographs indicate. The 4 % CH_4 diamond is dominated by the smaller grains (30-100nm) where the 5 % CH_4 sample has a grain size of about 10-50 nm by SEM, 9 nm by TEM and 22 nm by XRD. Surprisingly the grain size determined by XRD is bigger than the grain size estimated by TEM which is probably due to the nanocrystalline seeded TEM sample and regular seeded XRD sample. Values between 10 to 100 nm are typical grain sizes for nanocrystalline diamond.(111, 112)

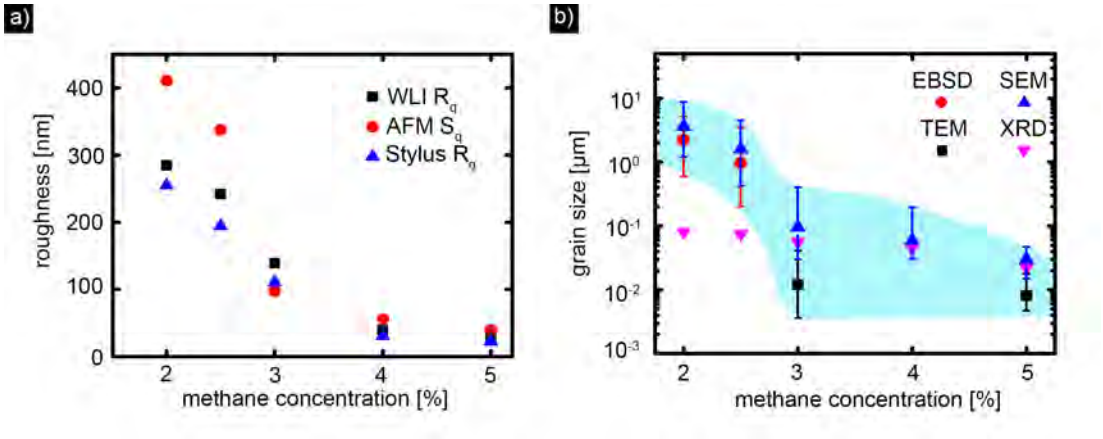

Figure 4.6: Roughness and grain size overview - the roughness and grain size measurements are summarized; a) the surface roughness measurement of the AFM is the best result because of its sharp tip and better lateral resolution compared to the stylus profilometer and WLI. b) The SEM results capture almost the range of all measurements except of the smaller TEM results. For further characterization the SEM results are used. The high XRD grain size for the 5 % CH_4 is probably due to a regular seeded sample compared to the nano seeded TEM sample

4.2.2 Chemical and mechanical characteristics

The sp^2 or sp^3 hybridization of the carbon to distinguish between graphitic and diamond components was determined by XANES and Raman measurements. For the XANES measurements the sp^2-hybridized carbon content was estimated out of our total electron yield by integrating the peak area of the π^* peak and comparing it to the integrated peak area of the reference HOPG peak. Even for the lowest grain-sizes the sp^2 hybridized carbon content was below 5 %. However more quantitative data was not possible because of contaminations on the diamond surface. The bulk sensitive total flu-

oresce yield (TFY) XANES measurements allowed a qualitative analysis that indicates increasing sp^2 content with increasing grain size, Fig. 4.7a). The spectra exhibit the representative diamond exciton peak at 289.5 eV with the characteristic spectrum of diamond. The qualitative TFY analysis is confirmed with Raman spectroscopy where our samples show a sharp sp^3 diamond peak even though Raman spectroscopy is more sensitive to sp^2 bonded carbon. The width of the diamond peak at 1332 cm^{-1}reveals how much random stress or many defect free grains are present.(36). Here the diamond peak at 1332 cm^{-1}gets more distinctive with increasing grain size, Fig. 4.7b). The ratio of the G-peak 1580-1600 cm^{-1} to the D-peak around 1350 cm^{-1} was not analyzed to determine the crystallite size and amount of "disorganized" carbon.(25) Even though the samples were extensively cleaned with de-ionized water and methanol no unambiguous data of the G-peak could be obtained.

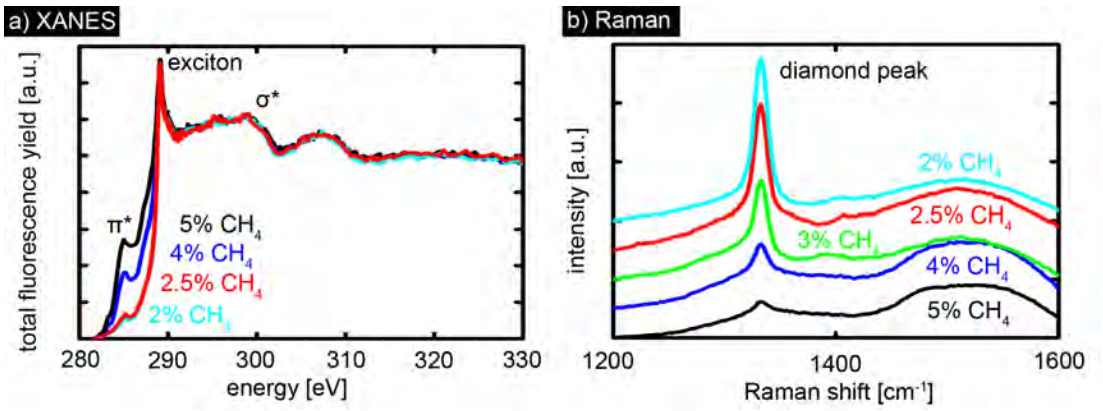

Figure 4.7: XANES and Raman - the graphitic sp^2 and diamond sp^3 phase in our samples is charcerterized by XANES and Raman. a) the π^* peak is related to sp^2 carbon and it increases with decreasing grain size; b) the intrinsic diamond peak around 1335 $\frac{1}{cm}$ shows a more distinctive diamond peak for coarse grained samples

The hydrogen content and its bonding are analyzed by ERDA and FTIR. For the ERDA the hydrogen content was calculated with RUMP code for two samples first and then linearly interpolated for all samples.(22) Figure 4.8a) shows the measurement and the RUMP simulation of a 5 % CH_4 sample. The calculation reveals a hydrogen concentration of 3.5 at.%. For the linear interpolation all spectra were plotted in one graph and at a depth of 200 nm the hydrogen content was linearly interpolated from

the yield. The small grained material had up to 3.5 at.% hydrogen and with decreasing grain size the hydrogen concentration almost linearly decreased to 0.9 at.% hydrogen. Earlier work by Reichart investigated the distribution of hydrogen in diamond and he concluded that most hydrogen is located at the grain boundaries.(84) For the bonding of the hydrogen to the carbon and an additional qualitative analysis of the hydrogen FTIR absorbtion measurements were performed. The ERDA results were confirmed by FTIR which additionally probes the entire sample thickness. In Fig. 4.8b) the FTIR spectra of all 5 diamonds are shown and the hydrogen concentration increases with the CH_4 concentration. Moreover the FTIR results reveal that the hydrogen is bonded to sp^3 carbon since all the absorptions occur in the sp^3 regime between 2850 and 2955 cm^{-1}.(85) This means that the sp^3 carbon in our grain-boundaries mostly causes the hydrogen impurity. Parallel to the ERD-analysis Rutherford backscattering (RBS) experiments were conducted and only negligible amounts of oxygen on the surface were detected.

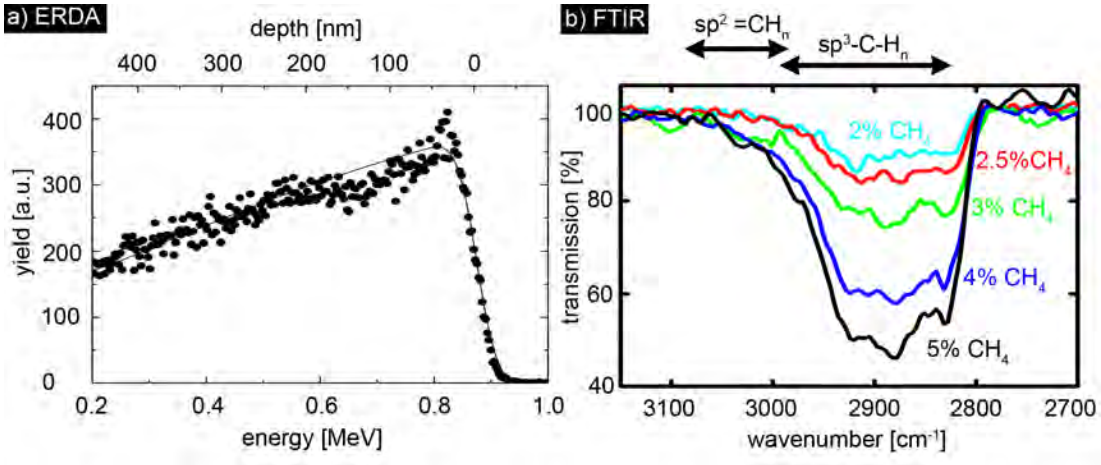

Figure 4.8: ERDA and FTIR - the hydrogen concentration and bonding is measured by ERDA and FTIR. a) the ERDA measurement from the nanocrystalline 5 % methane diamond film and the RUMP code simulation reveal a hydrogen concentration of 3.5 %; b) the FTIR absorption measurement in the hydrogen region shows less transmission for the fine grained samples and almost the entire absorption is in the regime of sp^3 bonded hydrogen.

Figure 4.9a) summarizes the hydrogen content results. The maximum hydrogen content is 3.5 at.% and the lowest 0.9 at.%. Compared to values in the literature this

is a good agreement for the fine grained samples. Michaelson's values were between 5.1 and 6.1 at.% and Wiora's values between 3.2 and 4.3 at.% for 9-30 nm grains.(65, 112) The sp^2 content is not shown in the viewgraph because only an upper threshold of 5 % was calculated. The calculated 5 % sp^2 carbon content in our samples are confirmed with Wiora's values between 3-7 % sp^2 carbon for 10-60 nm grains.(112)

The density is clearly affected by the grain size and CH_4 concentration in Fig. 4.9. The density of the diamonds decreases with increasing grain size. The micro-crystalline grained material has a density close to the density of single crystalline diamond around 3.52 $\frac{g}{cm^3}$ while the small grained materials can exhibit a density as low as 3.3 $\frac{g}{cm^3}$. The density is especially important for analyzing the high energy density physics experiments where it is important to distinguish between pores in the material and lower density elements/allotropes such as hydrogen and graphite.

To estimate the effect of hydrogen on density, I assume as a first order approximation that hydrogen simply replaces carbon atoms by forming C-H groups (hydrogen has $\frac{1}{12}$ of the mass of carbon). If I take the ERDA results as this percentage it would yield exactly with 0.25 % deviation to the density of the 2-3 % CH_4 samples. For the nanocrystalline samples with 4-5 % CH_4 the density would be still about 3 % too high. Similar to the hydrogen the sp^2 hybridized carbon has the effect of lowering the density which is more pronounced at the many grain boundaries of small grains. With the known total density, density of sp^2 graphitic carbon ($\sim 2.15\frac{g}{cm^3}$) and hydrogen content the maximum amount of sp^2 in the diamond lattice can be calculated. For the microcrystalline samples with 2-3 % CH_4 the amount of sp^2 can be neglected since the hydrogen alone explains the density difference. The sample with 4 % CH_4 can reach a maximum sp^2 value of 3.6 % which is well below the maximum value of 5 %. For the nanocrystalline sample 7.5 % sp^2 would be required to explain the density difference which is above the maximum value of 5 %. The calculated total density is still 2.5 % higher than the actual measured density which means that either voids or a different carbon bonding cause this discrepancy. The TEM image did not show any pores and thus rules out the solution of having voids in the diamond sample at least in the area of the TEM sample. A possible explanation is tetrahedral amorphous carbon (ta-C) that has a density of 2.45 $\frac{g}{cm^3}$ and still contains 50 % sp^3 carbon.(95) By repeating the

same calculation from above instead of sp^2 carbon with ta-C the total density matches and is within the 5 % sp^2 limit. Because of ta-C similarity to diamond it would not show any difference in the XANES spectra.

The Young's modulus increases with increasing grain size as expected, Fig. 4.10). The Young's modulus for optical diamond is between 1100-1200 GPa and the coarse grained 2 % CH_4 sample should be close to this value.(82) Unfortunately this value does not match and additional experiments such as nanoindentation would be required to achieve a broader experimental base for assessing the unexpected results.

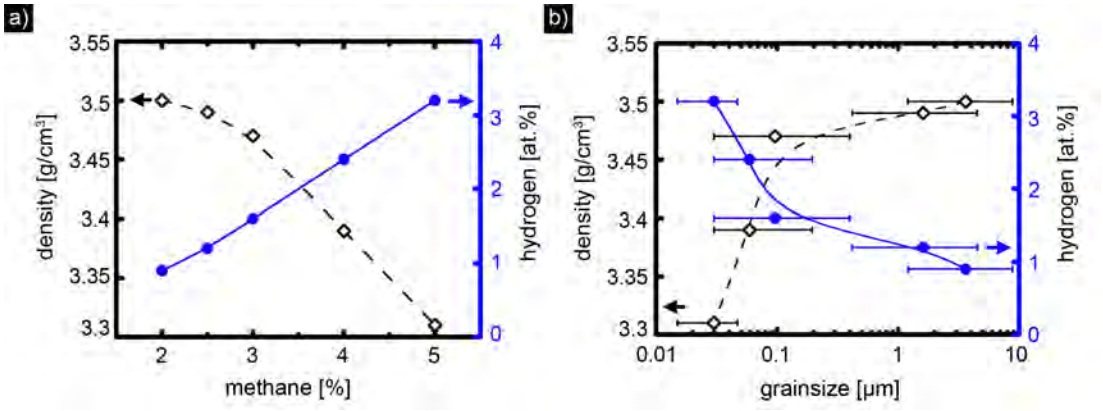

Figure 4.9: Overview of hydrogen and density *vs.* grain size and CH_4 - a) shows that the hydrogen content increases almost linear with the CH_4 concentration while the density drops after 3 % CH_4; b) the density drops for the nanocrystalline material and the hydrogen content decreases with increasing grain size. The lines are added as visual guidance

4.2.3 Sandwich targets and special geometries

For high energy density physics experiments the shock propagation through different geometries is especially important to calculate the equation of state tables and to predict hydrodynamic instabilities. Figure 4.11a-c) show a diamond step-target, a ripple-target and diamond capsules. To manufacture the step target in Fig. 4.11a) the steps are machined in a silicon wafer which is used as seed surface to grow the diamond on top of this mold. After the sample achieved the required thickness during the growth process the silicon wafer is etched off the diamond leaving the free standing sample behind. To

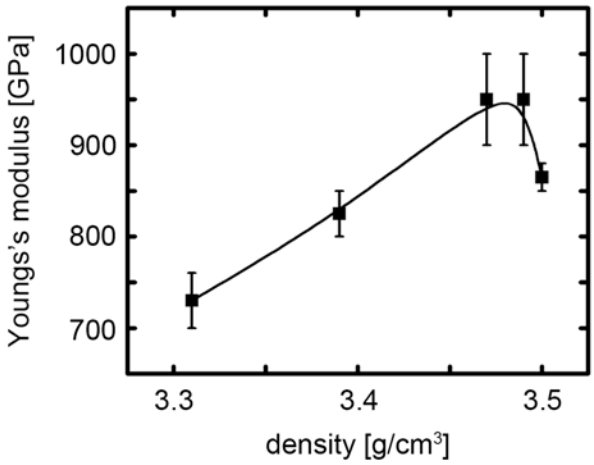

Figure 4.10: Young's modulus *vs.* density - qualitatively the Young's modulus increases with increasing grain size as expected. The coarse grained 2 % CH_4 highest density sample does not follow this trend

achieve a uniform flat surface on the opposing growth side the steps transferred to the growth side of diamond were removed by polishing while the seed side contained the perfect imprint of the mold. The ripples in Fig. 4.11b) were grown on a silicon mold which transferred the sine wave perfectly to the diamond. Figure 4.11c) shows diamond capsules that were grown on a silicon mandrel which was later etched out leaving the free standing diamond capsule behind.(9) These diamond capsules are promising candidates for ICF experiments as mentioned above.

With the results from the diamonds grown at five different CH_4 concentrations above a sandwich target was manufactured which contained layers of micro- and nano-crystalline diamond. The change between micro- and nano-crystalline diamond was induced by periodically changing the feed gas ratio. The goal of the microcrystalline diamond was to achieve a pure diamond with a high density while the nano-crystalline diamond was supposed to keep the surface roughness low. Figure 4.11d) schematically shows the sandwich diamond grown as a step target with three 10 μm steps and a maximum thickness of 170 μm. A TEM sample slice was ion-etched out of the diamond step target and further characterized in Fig. 4.11e) and f). Figure 4.11e) shows a SEM of this slice with the bands of nano- and microcrystalline diamond running

parallel to the nucleation surface. The TEM in Fig. 4.11f) reveals these bands at an even higher magnification where the dark bands are the nanocrystalline layers. As reference to distinguish between nano- and microcrystalline grains one nanocrystalline layer was duplicated on top of each other. The sandwich structure with the parallel band structure even after 500 layers on top of each other indicates a high reproducibility of the layer growth. The smooth surface was consequently achieved but a density measurement revealed 3.25 $\frac{g}{cm^3}$ as density. This value is lower than expected for nanocrystalline diamond but it performed very well in a shock experiment and reached 5 TPa.(100)

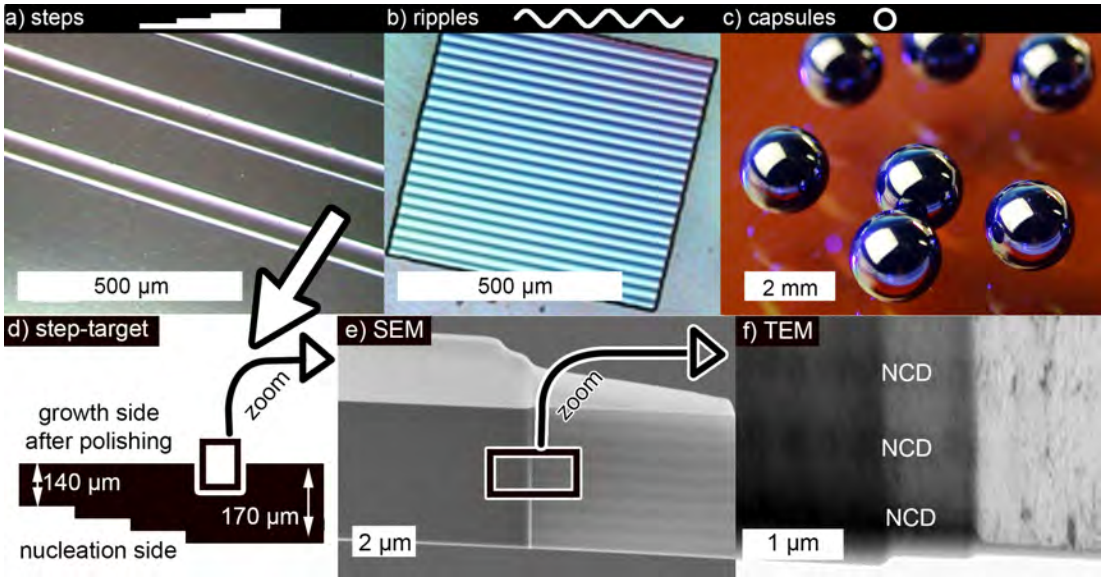

Figure 4.11: HED diamond targets: steps, ripples, capsules and a sandwich target - the first row shows examples of diamond targets for HED physics experiments: a) stepped diamond target with 4 steps 15, 30, 45 and 60 μm thick and each step 200 μm wide for ramp-wave compression experiments; b) a diamond sine wave target with a 50 μm period and 250 nm amplitude to study hydrodynamic instabilities; c) the diamond ablator shells which are coated with an aerogel in the following chapter and have 2 mm inner diameter; the second row shows the characterization of a sandwich step target which has alternating layers of micro- and nanocrystalline diamond; a) shows schematically how a TEM sample was ion etched from the growth side on the step target; b) the SEM image of the free standing sample already shows some band structure; c) the TEM image clearly shows some dark bands which are 300 nm thick and are assigned to nanocrystalline diamond

CH_4	**Deposition temp.**	**Growth rate**	**Thickness**	**AFM roughness**	**AVG grain size SEM**	**Grain size range**	**Density**	**Young's modulus**	**Hydrogen**	sp^2 **carbon**
[%]	$[C^\circ]$	$[\frac{\mu m}{h}]$	$[\mu m]$	$[nm]$	$[\mu m]$	$[\mu m]$	$[\frac{g}{cm^3}]$	$[GPa]$	$at.\%$	[%]
2	850	0.394	39.4	411	3.6	0.6-8.8	3.5	865	0.9	~ 0
2.5	840	0.421	42.1	338	1.6	0.2-4.5	3.49	944	1.2	~ 0
3	830	0.384	30.7	97	0.1	0.004-0.4	3.47	975	1.6	~ 0
4	850	0.441	44.1	56	0.06	0.03-0.2	3.39	838	2.4–2.7	<3,6
5	830	0.406	40.6	40	0.03	0.005-0.05	3.31	730	3.2–3.5	$\leq$5
sandwich	830	0.35	170	-	-	-	3.25	-	-	-

Table 4.1: Overview diamonds - summary of the diamond characterization results

4.3 Conclusion

The five samples characterized here show a clear correlation between grain size, density and their composition. The smaller the grains the higher were the fraction of hydrogen, sp^2 hybridized carbon and the lower the density. The diamond with the low CH_4 feed-gas concentration of 2 % almost showed optical diamond properties with a high purity (<1 at.% hydrogen, negligible sp^2 carbon, $> 3.5\frac{g}{cm^3}$ density). For the samples with a higher CH_4 feed-gas concentration of up to 5 at.% the density gradually decreased to about $3.3\frac{g}{cm^3}$, the hydrogen content increased up to 3.5 at.% and the sp^2 hybridized carbon fraction increased to up to 5 %. Noticeable is that the roughness clearly decreases as the diamond transitions into nanocrystalline growth as it can be seen in Fig. 4.12

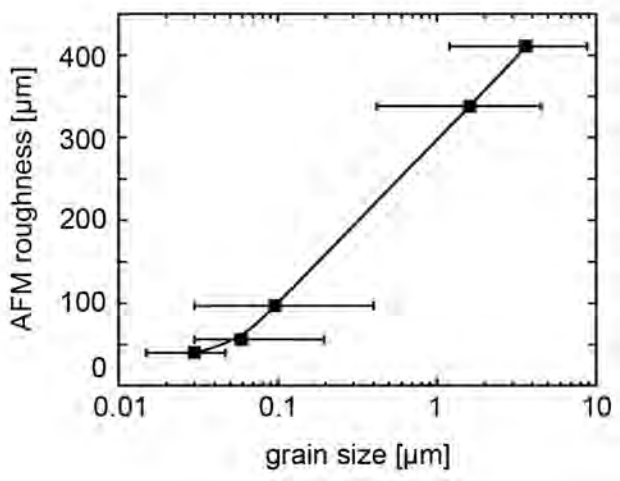

Figure 4.12: Roughness *vs.* grain size - the roughness clearly decreases with the start of nanocrystalline growth and the 3 %, 4 % and 5 % CH_4 have a smooth as grown surface

The ERD-analysis and RBS did not show any other noticeable impurities than hydrogen and the hydrogen concentration is lower than for the published data on hot-filament CVD grown diamond in the same grain size range. The sp^2 hybridized carbon in our samples is similar compared to other published data. The MPCVD grown diamonds here have a high purity and the smooth as grown surfaces of the nanocrystalline diamond make these materials a promising target for HED physics experiments. Our approach to increase the density while keeping the surface roughness of nanocrystalline

material yielded in a surprisingly uniformly layered target but the density did not increase. In the next chapter I will coat a layer of aerogel within spherical diamond targets.

5

Chemistry in a capsule

The chemistry in a capsule approach was developed to cast foam within the ablator target. Here I use diamond capsules as ablators and casted the foam within these 2 mm inner diameter spherical capsules. Figure 5.1 schematically shows the chemistry in a capsule approach and gives the basic outline for this chapter. In the first step the capsule is mounted by friction to define the position of the fill hole during the entire process. The capsule is filled with a defined volume of aerogel-precursor-solution in the second step. Here I use a CH-based aerogel (poly(dicyclopentadiene)) (PDCPD) with a tunable viscosity *vs.* time behavior (Chapter 5.1) which is required in the following coating step where the viscosity is adjusted to uniformly coat the capsule interior. During coating the capsule is deterministically rotated while the viscosity of the aerogel increases. After the aerogel reached the sol-gel transition the gel layer builds an inner sphere within the ablator target. The low density of the aerogel makes it very sensitive to the drying process. Because of this sensitivity a super critical drying process is required and the initial solvent of the aerogel has to be exchanged to another solvent which is better miscible in the super critical fluid (carbon dioxide (CO_2)). In the last step the exchanged solvent is replaced by liquid CO_2 that is brought to its supercritical condition and subsequently evaporated so that no phase transition occurs which could damage the fine pore network. In this process the foam structure and network are maintained and a foam layer connected to the ablator target is left behind. To monitor the the chemistry in a capsule process the coating and chemistry parameters as well as the coating results are tracked in a wiki-database.

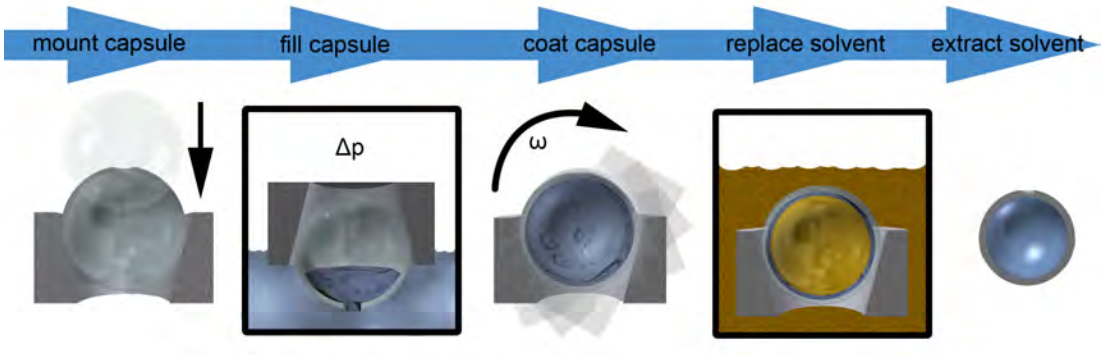

Figure 5.1: Schematic chemistry in a capsule process - in the first step the capsule gets mounted by friction in a tapered hole to control the fill hole position during the entire process. In the following step the capsule gets filled with the required precursor solution by under-pressurizing and re-pressurizing the capsule. With the desired amount of precursor solution in the capsule a deterministic rotation process is started to distribute the precursor during gelation in the capsule. The wet gel layer of PDCPD contains toluene which needs to be exchanged by acetone which is better miscible in liquid CO_2. The solvent exchange is done by pressuring the capsule and waiting for diffusion to exchange the toluene with acetone. In the final step the gel layer in the capsule is super-critically dried which means that CO_2 is used in its supercritical regime

5.1 Aerogel chemistry

The requirement of pure CH_x foam limited the choices of the applicable aerogels. Silica- and resorcinol-formaldehyde aerogels are the most common and characterized gels for target applications, but both of them did not meet the requirement of being a pure CH_x gel. Thus we decided to use poly-dicyclopentadiene (PDCPD) aerogel which was initially characterized for insulation applications.(56) PDCPD is a low-cost material and is coproduced in large quantities in the steam cracking of naphtha and gas oils to ethylene. In addition I performed coating experiments with titanium-oxide (TiO_2), silica oxide (SiO_2) and iron oxide (Fe_2O_3) aerogels.

5.1.1 Experimental

5.1.1.1 Dicyclopentadiene (DCPD) based aerogel

Dicyclopentadiene (DCDP, $C_{10}H_{12}$, Aldrich), norbornene (NB, C_7H_{10}, 99 %, Aldrich) and Grubbs' 1st generation catalyst, bis(tricyclohexylphosphine)benzylidene ruthe-

nium dichloride (+97 %, Aldrich) were used as received without additional purification. The PDCPD monomer is a solid at room temperature (melting point 32.5 °C) consisting mostly out of endo isomer and containing butylated hydroxytoluene as stabilizer. The anhydrous toluene (99.8 %, Aldrich) bottle was purged about 10 min with nitrogen prior to use by injecting a long syringe needle connected to nitrogen and another needle as vent into the rubber-septum.

Polydicyclopentadine (PDCPD) is a polymeric aerogel and for its synthesis the ring opening metathesis polymerization (ROMP) approach is commonly used. Lee and Gould were the first who demonstrated the ROMP approach for PDCPD aerogels.(56) Grubbs' 1st generation catalyst opens the initial cyclic molecule that undergoes ROMP and is converted step by step to interconnected chains that finally build a polymer. Figure 5.2 schematically shows the process for PDCPD and NB. PDCPD has two double bonds that both undergo ROMP forming a 3D network. The addition of NB which has one double bond forms a less interconnected chain-network. In the 3D network gelation occurs quicker compared to the more linear NB chain network. The ROMP occurs at room temperature. PDCPD precursor solution was prepared in a 50 $\frac{mg}{cm^3}$ PDCPD/toluene one liter batch that was used for about 6 month. For the preparation of the solution I melted 50 g of PDCPD and injected it by syringe into a sealed bottle of anhydrous toluene. I stored the solution in a freezer at about -5 °C. To adjust the density of the precursor solution the desired amount of toluene was added. E.g. for 10 mL of 25 $\frac{mg}{cm^3}$ I mixed 5 mL 50 $\frac{mg}{cm^3}$ PDCPD/toluene with 5 mL of anhydrous toluene. Catalyst solution was prepared daily by weight with 20 mg of Grubbs 1st generation catalyst and 8.67 g (10 mL) anhydrous toluene mixed to a 2 $\frac{mg}{cm^3}$ catalyst/toluene solution. This catalyst toluene solution was mixed on a vortex mixer for about 5 min to ensure that the catalyst was completely dissolved. Unless otherwise noted I added 0.1 wt.% catalyst by eppendorf pipette to the 50 $\frac{mg}{cm^3}$ PDCPD/toluene solution (250 μL for 10 mL) and 0.2 wt.% to the 25 $\frac{mg}{cm^3}$ PDCPD/catalyst solution (250 μL for 10 mL). It is of extreme importance to use clean toluene resistant labware and anhydrous toluene for the preparation of the aerogel. The catalyst is very sensitive to water and even changes in humidity changed the gelation behavior. For each sample new glass vials with metal foil seals were used to ensure compatibility with toluene.

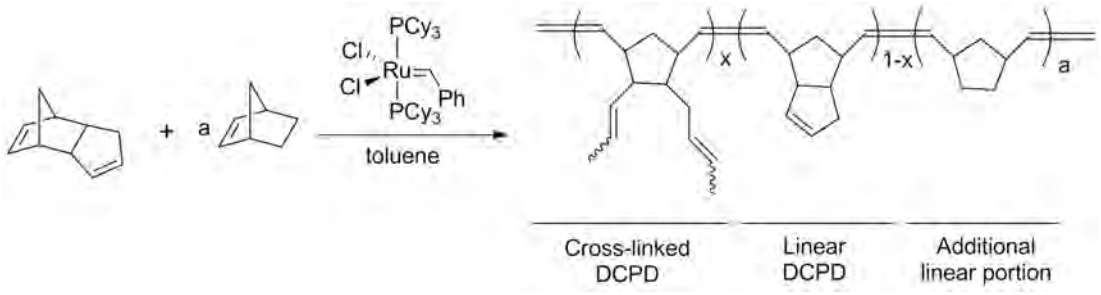

Figure 5.2: Ring opening metathesis polymerization (ROMP) - shows the ROMP for dicyclopentadiene (DCPD) and norbornene (NB) in toluene using grubbs first generation catalyst

Additives for the PDCPD were prepared in separate batches and added as desired to the prepared PDCPD/toluene mixture. For Poly(dicyclopentadiene-random-norbornene) (P(DCPD-r-NB)) I prepared a separate 50 $\frac{mg}{cm^3}$ NB/toluene mixture in a 40 mL vial which usually lasted for about a month. To mix 25 $\frac{mg}{cm^3}$ PDCPD/toluene, 10 wt.% NB and 0.2 wt.% catalyst I weighed 4.34 g (5 mL) 50 $\frac{mg}{cm^3}$ PDCPD/toluene, 4.34 g (5 mL) toluene and added 500 μL 50 $\frac{mg}{cm^3}$ NB/toluene and 250 μl 2 $\frac{mg}{cm^3}$ catalyst/toluene by eppendorf pipette. If desired the transparent wet gel was dyed with 2 $\frac{mg}{cm^3}$ solvent blue 35/ toluene solution to increase its visibility.

5.1.1.2 Silica oxide (SiO_2) gels

For SiO_2 gels with a set density of 120 $\frac{mg}{cm^3}$ two prepared solutions were mixed with each other. One solution consisted out of 1.14 g tetramethoxysilane (TMOS, Silar Laboratories) that was refluxed to remove low boiling constituents and impurities before use, and 3.89 g methanol (MeOH, anhydrous, 99.9 %, EMD). The other solution was prepared with 2.78 g MeOH, 417 μL deionized water and 56 μL ammonium hydroxide (NH_4OH, ACS grade, Aldrich). Both batches were stored in a freezer for up to 1 week. In contrast to P(DCPD) SiO_2 gels are inorganic and gelation occurs through hydrolysis (cleavage of chemical bonds by the addition of water) and condensation (formation of a larger molecule and a small byproduct molecule) initiated by the NH_4OH.(47) To increase the visibility of the 10 mL transparent wet gel it was dyed with 10 mL of 2 $\frac{mg}{cm^3}$ crystal violet/ MeOH solution for 12 hours.

5.1.1.3 Iron oxide (Fe_2O_3) gels

Fe_2O_3 gels were prepared with a density of about 40 $\frac{mg}{cm^3}$ by mixing two solutions with each other. One solution consisted out of 0.42 g iron (III) chloride hexahydrate ($FeCl_3 \bullet 6H_2O$, 98 %, Aldrich), 5 g ethanol (EtOH, anhydrous, 99.9 %, EMD) and 100 μl deionized water. The other solution was mixed out of 1 g EtOH and 0.9 g (±)-propylene oxide (PPO, 99.5 %, Aldrich). Both solutions were used immediately after mixing and led to 10 mL precursor solution. The water starts the hydrolysis and the PPO steals a proton from the metal ring and turns the solution slightly acid that opens the ring and initiates the condensation.(30) The final Fe_2O_3 gel had a yellowish color.

5.1.1.4 Titanium dioxide (TiO_2) gels

The TiO_2 gel with a density of 193 $\frac{mg}{cm^3}$ was mixed in an ice bath to ensure that the highly flammable (±)-propylene oxide (PPO, 99.5 %, Aldrich) was stable. First 2 g of titanium (IV) ethoxide ($Ti(OC_2H_5)_4$, technical grade, Aldrich) and 7.14 g EtOH were mixed in an magnetic stirrer in an ice bath. After 5 min 143 μL hydrochloric acid (HCL, 37 %, Aldrich) were added plus a prepared mixture of 172 μL deionized water and 0.76 g PPO. The water had to be mixed with the PPO before adding it to the solution to prevent the precipitation of $Ti(OC_2H_5)_4$. This entire solution was stirred for another 5 min in ice water before it was used for measurements or coatings. The gelation of TiO_2 is similar to the SiO_2 and Fe_2O_3 gelation but the condensation was initiated with HCl and PPO.(13, 30) The final TiO_2 gel had a milky transparent color.

5.1.1.5 Glass-ware and oils

All experiments requiring containers smaller than 40 mL were done in disposable pre-cleaned glass-ware with caps attached. The caps of the disposable glass vials were metal foil or PTFE for toluene based gels and polyethylene cone seals for all other aerogels. Roller glass bottles (Wheaton Sci.) 110 x 270 mm (I.D. 103 mm and 190 mm coatable wall height) were cleaned with a saturated potassium hydroxide water solution for one week at room temperature and rinsed with concentrated sulfuric acid (97 %) afterwards.

For tests which required constant viscosity - reference standards were used. Most experiments were done with Brookfield silicone oil and a few experiments with Cannon olefin- or mineral oil general purpose viscosity standard. Unless otherwise mentioned silicone oils were used.

5.1.1.6 Aerogel doping

Three different doping techniques for the PDCPD based gels were developed. Two simple techniques are based on the diffusion of iodine in gas or liquid into the foam or wet gel. Wet PDCPD gels were placed in a 1-10 $\frac{mg}{cm^3}$ iodine toluene solution until the gel turned black. For the doping of the dried aerogel foams the samples were placed with solid iodine in a closed container until the foam turned dark. Another method is the copolymerization of modified monomers and adding these monomers like I added the regular NB before. More about the synthesis of (bis)iodo-norbornene monomers can be found in Kims publication.(52)

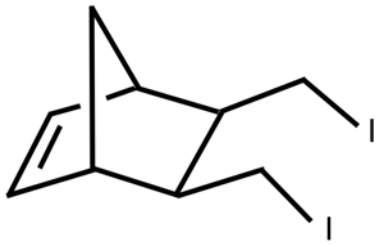

Figure 5.3: (Bis)iodo-norbornene - shows the synthesized (bis)iodo-norbornene monomer

5.1.2 Results and Discussion

The robustness of the foam when wetted with liquid DT-fuel is one of the most important requirements. Figure 5.4a) shows a 30 $\frac{mg}{cm^3}$ PDCPD aerogel piece in liquid hydrogen. The piece sinks in liquid hydrogen and no visual evidence of cracking is visible. Small angle x-ray scattering experiments confirmed this behavior where the scattering initially increased when liquid got into the pores and decreased as the pores got filled. Figure 5.4b) shows an experiment with a 25 $\frac{mg}{cm^3}$ PDCPD foam that was filled with liquid deuterium (LD_2). Initially in the upper picture only the iodine doped

foam is visible. In the next step this foam is filled with LD_2, this was confirmed with a buildup of a meniscus at the fill tube and a small debris part. The lower picture shows an overfill of LD_2 with a liquid puddle of deuterium at the bottom.

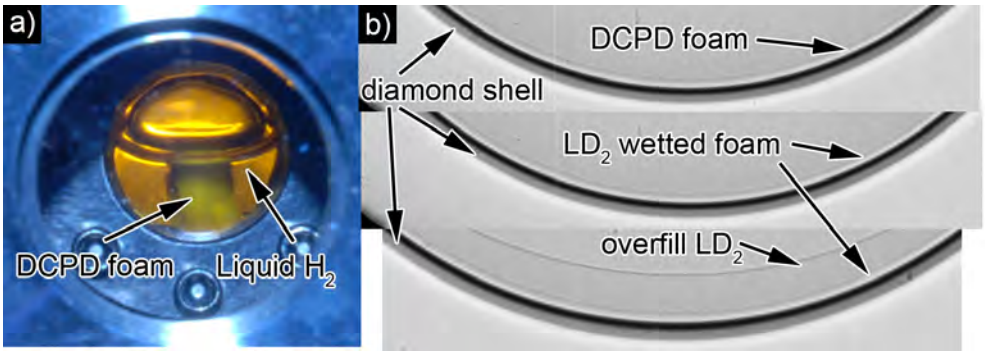

Figure 5.4: DCDP survives liquid hydrogen - a) shows a piece of 30 $\frac{mg}{cm^3}$ PDCPD aerogel in liquid hydrogen. During the filling with liquid hydrogen the PDCPD layer did not show any shrinkage which indicates that the PDCPD is strong enough to withstand hydrogen wetting. b) shows a 25 $\frac{mg}{cm^3}$ P(DCPD-r-NB) foam layer which was wetted with liquid deuterium (LD_2). The upper image shows the dried foam, in the center image the foam is wetted with LD_2 and in the lower image the interface between wetted foam and LD_2 is visible. The process is reversible without damaging the foam layer

The doping has two different purposes. It is one requirement for NIF-targets to determine the temperature of the implosion. In addition the pure low-density PDCPD aerogels are not visible in radiographs to determine the quality of the dry foam. The doping with liquid or gas phase iodine doping has the disadvantage of not being quantitative and a too high iodine dose like 10 $\frac{mg}{cm^3}$ iodine/toluene tends to damage the gel network. Another disadvantage of the liquid doping is the iodine wash-off in case the gel needs additional solvent exchange. Figure 5.5 shows the iodine doping procedure. The wet 25 $\frac{mg}{cm^3}$ 15 wt.% NB P(DCDP-r-NB) was doped with 1 mL 1.5 $\frac{mg}{cm^3}$ iodine toluene solution for 2 days. The resulting gel is almost dark. After washing this gel in hexane for 10 days almost all of the iodine gets washed-off and after additional 7 days in acetone the iodine is barely visible at all. To prevent this iodine wash-off the capsule could be directly dried without solvent exchange, but this leads in most cases to a collapse of the gel during drying. Consequently we developed in our group an iodine NB copolymer that is currently tested, Fig. 5.3.

Figure 5.5: Iodine doping wash-off in PDCPD gels - shows how liquid iodine doping which is required as contrast agent for radiography images can be washed-off with acetone and hexane wash (from left to right): the doping solution containing iodine and toluene; the pure aerogel; the iodine doped aerogel after two days; the iodine wash-off after 10 days in acetone and the wash-off after additional 7 day hexane wash

5.2 Capsule control parameters

The progress of each coating experiment was tracked with a wiki-database. After I received the capsules from Diamond Materials GmbH the capsules were added to the wiki-database with their initial weight, degree of cleanliness, its target and actual hole size, date of arrival and batch they were manufactured in. The weight measurements were performed with a Mettler-Toledo XP-2U balance which has an accuracy of 0.1 μg, the visual inspection was done with standard Nikon stereo microscope and the hole size measurement was done with a Carl-Zeiss SteREO Discovery V12. After the initial capsule check and registration in the wiki with consecutive numbers they were stored in 2 mL glass vials until the capsules got filled. The same procedure was applied for recycled capsules. The capsule recycling was done at 450 °C for 12 hours in an oven to oxidize residual CH-foam to CO_2. The diamond was not damaged by this process since the transformation of diamond in graphite occurs above 450 °C.

A screenshot in Figure 5.6 shows the wiki with data of the filling process. I structured the wiki in several layers to keep track of the capsule condition, mounting, filling, doping, drying and additional layers for the chemistry, protocols of our group meetings, simulation efforts and the diamond targets. The basic data contained the capsule weight before and after filling, the pressure differential which was applied for the filling, the composition of the gel, the coating speed and parameters, the duration of the coating, the layer quality, the capsule mounting technique used, the drying parameters and the images acquired to control the layer quality.

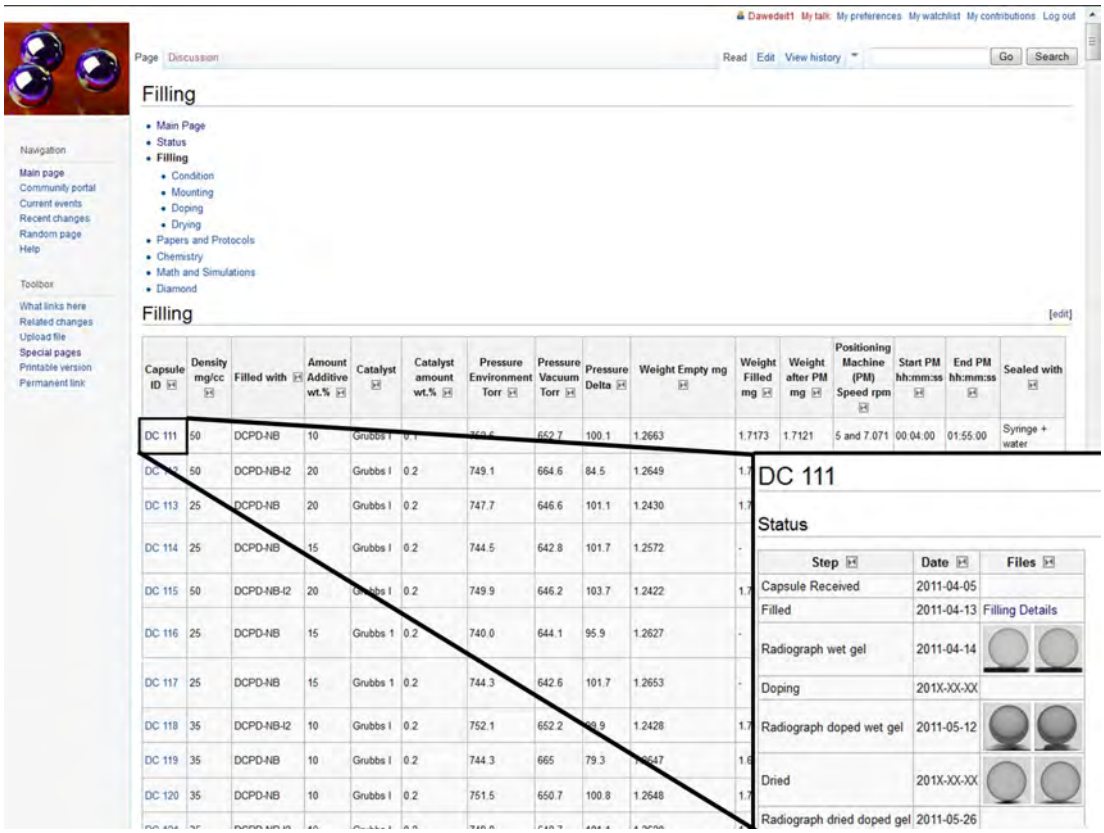

Figure 5.6: wiki - shows the wiki which was used to track the capsule coating parameters, the coating success and as database for radiography images

5.3 Capsule mounting

The capsule holder changed several times in the chemistry in a capsule project to fulfill growing requirements. For the first capsules I started with a simple titanium holder

with a deepening in the center. This holder had a M6 thread to connect to the rotation device and the capsule was centered by the depression. Figure 5.7a) schematically shows this first holder. To prevent the capsule from falling off the entire holder was covered with a titanium cover lid. The advantage of this holder was that it was independent of the capsule size but the capsule could not be plugged and solvent evaporated out of the capsule. As next temporary capsule holder I used centrifuge containers that had the same diameter as the capsule in the lower part. I filled the rest of the centrifuge container with KimWipes®and solvent to prevent evaporation out of the capsule. The conic shape of the centrifuge containers allowed screwing them partially into the M6 threads of the rotation device. Figure 5.7b) shows a special designed syringe holder. The capsule was fixed with the plunger of the syringe at the low diameter needle connector. The syringe itself was fixed with a set screw. To prevent precursor evaporation the capsule was surrounded by precursor solution or solvent. The low diameter needle connector was closed with hot-glue. This set-up worked well even though the syringe was partly dissolved by the solvent. Unfortunately this configuration did not allow to rotate the capsule with a defined fill hole position.

To hold the capsule in a defined position I developed a new holder with a tapered hole where the capsule gets temporary stuck. Figure 5.7c) shows the capsule which goes into the tapered hole below it. To remove the capsule out of the holder a little pressure was applied on the side-hole of the holder that was connected to the taperd hole. The pressure pushed the capsule out of the holder. The holder was manufactured out of ferritic stainless steel to attach a magnet on top of the capsule with a perfluoroalkoxy-polymer membrane to seal the fill hole. This seal did not work satisfactorily over several hours and the reflections of the spherical capsule made it hard to verify the fill hole position. In addition the different thermal expansion of the diamond and steel broke two capsules.

The next capsule holder was made out of PTFE which is chemically inert to toluene and its non-sticky surface is gentle to the diamond capsules. Instead of using a magnet or a screw cap, that was used for an intermediate holder, I decided to use PTFE pipette tips filled with precursor to surround the fill hole with precursor solution. The pipette point is sealed with hot glue. Figure 5.7d) shows a schematic drawing of the holder and

the actual holder with a PTFE tip below it. The technical drawing can be found in appendix B. The tapered hole is only 2 mm deep followed by a 2 mm through hole with an M2 thread at the end. This inner M2 thread is used for the capsule filling setup and for another rotational coating device. In addition by shining light through the inner 2 mm hole one can easily see the fill hole in the capsule to confirm its position. To mount the blank capsule it is first aligned under the microscope. Then the capsule is picked up with a vacuum chuck with the fill hole covered by the vacuum chuck and finally placed in the capsule holder. Friction holds the capsule in the tapered hole and by pushing a needle through the 2 mm hole the capsule can be easily removed. This holder can be used for the entire chemistry in a capsule process with the pipette tip removed after the coating. The outer M6 thread which is on all the holders except of the syringe and centrifuge container setup is still used to attach the holder to the coating device.

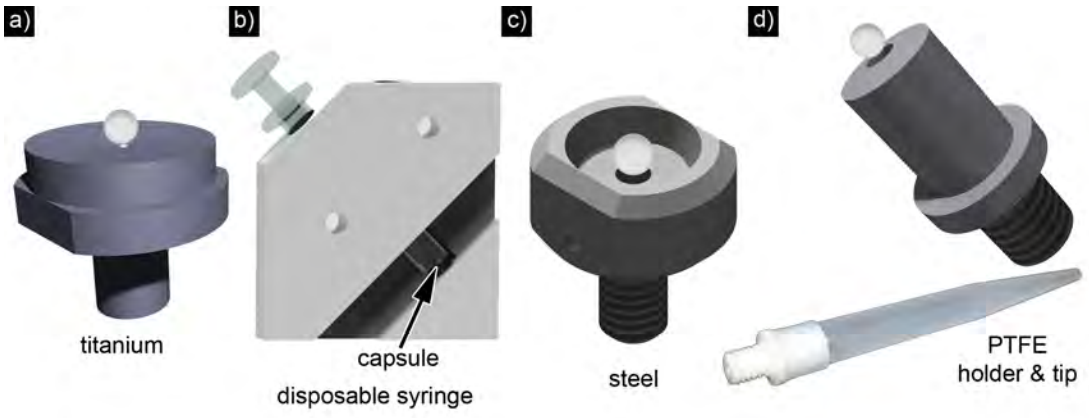

Figure 5.7: evolution of the capsule holder - a) was the first capsule holder which only had a small indent in the center and a screw cap on top (not shown) to hold the capsule with tissue in between, no proper sealing was possible; b) a disposable syringe was used to fix the capsule position in the channel to the needle, the fill hole position was not defined; c) the capsule was mounted in a tapered hole which held the capsule by friction in place, the seal by a magnet with a teflon membrane did not work satisfactory; d) the final holder was build out of PTFE and the capsule was mounted in a tapered hole. The capsule was sealed with a pipette tip on top which contained precursor solution

5.4 Fill setup

5.4.1 Experimental

The fill volume of precursor in the capsule determines the foam shell thickness. To deterministically fill the capsule, I developed a filling setup which is shown in Fig. 5.8. The capsule with the hole pointing down is mounted in the capsule holder and together with a vial of precursor solution they are both within a small vacuum chamber (Kurt Lesker 6 way Kleinflansch Cross). The vacuum chamber has one linear feedthrough (Kurt Lesker KLPD Push Pull Linear Positioner) to hold the capsule, two valves (Swagelok, needle valve) and one vacuum gauge (Kurt Lesker KJLC 902). One of the valves is connected to vacuum to under-pressurize the chamber and the other valve feeds air into the chamber from the environment.

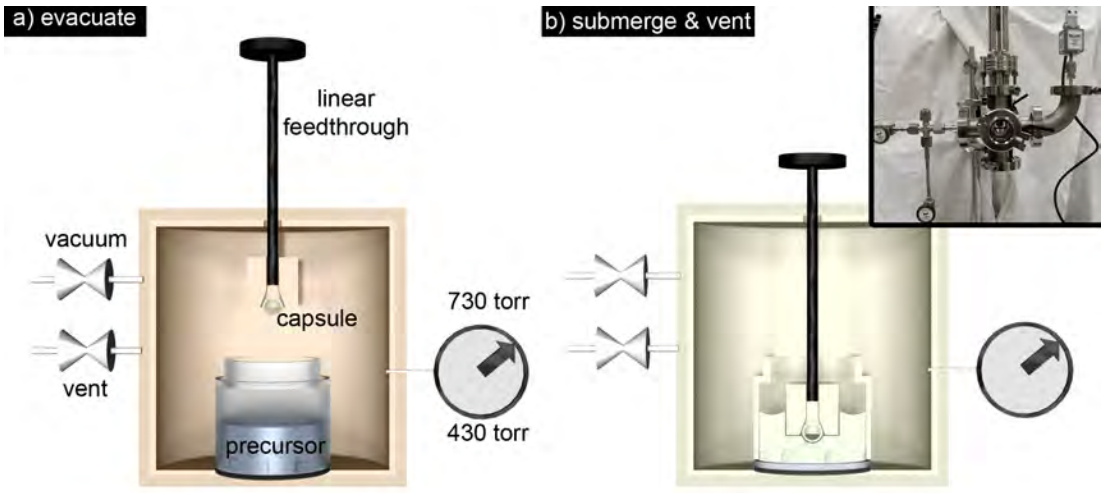

Figure 5.8: Δp pressure filling of the capsules - a) the chamber was under-pressurized while the capsule was mounted in a capsule holder with the hole pointing down and not in contact with the liquid. This dry evacuating has the advantage that no bubbles attach to the capsule which can re-enter the capsule when the chamber is re-pressurized; b) the capsule gets submerged in the liquid and the chamber gets re-pressurized. By controlling the pressure accurately a nL precision filling can be achieved. The insert shows the actual setup

To fill a capsule the chamber is slightly under-pressurized (20-250 torr below atmospheric pressure) which depends on the desired layer thickness, Fig. 5.8a). The capsule

is not in contact with the precursor solution yet to prevent the formation of bubbles near the fill hole. This is important to achieve a high reproducibility of the fill process. In the next step the capsule is submerged in the liquid by the linear feed-through, Fig 5.8b). By re-pressurizing the chamber to the environmental pressure the liquid is sucked into the capsule. The insert in Fig. 5.8b) shows the actual fill setup which has two windows to visually check the position of the capsule during the filling process. All parts are stainless steel, either KleinFlansch or VCR components. As a pressure gauge I used a piezo pressure transducer from KurtLesker that is toluene vapor resistant.

5.4.2 Results and Discussion

The required 10 nL precision control ($\pm 0.8 \mu m$ layer thickness variation for a $50 \mu m$layer) to achieve a high reproducibility is reached with the above describe filling process. Figure 5.9 shows the calibration with a 2 mm inner diameter diamond shell with a 30 μm diameter fill hole. The fill hole barely has any influence on fill volume as I compared a 30 μm and a 50 μm diameter fill hole with each other. The fill volume was acquired by measuring the weight of the capsule and calculating the weight by assuming a density of toluene (8.67 $\frac{g}{cm^3}$) for the precursor solution. The fill volume is completely linear with the applied pressure differential. These results agree with ideal gas law:

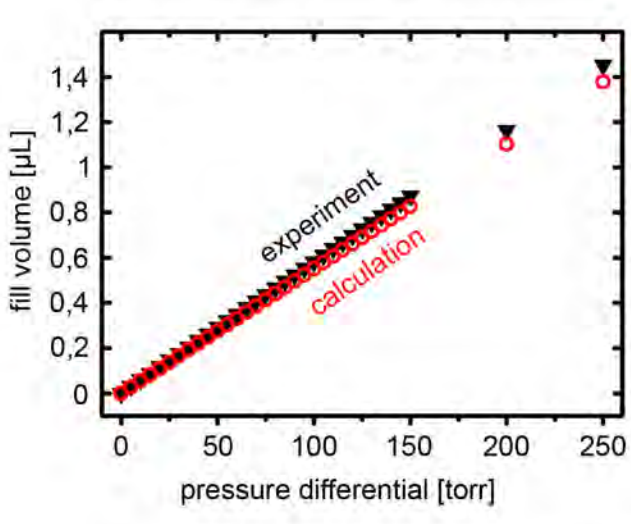

Figure 5.9: pressure filling calibration curve - shows how the amount of filling can be predicted by pressure change. The black triangles mark a 30 μm fill hole capsule which is close to the theoretical calculation with the ideal gas law

$$\Delta V = \frac{V_s \cdot \Delta p}{p_0} \tag{5.1}$$

where ΔV is the fill volume, p_0 the environmental pressure (760 torr), Δp the pressure differential applied and V_s the volume of an empty capsule (4.19 μL). The small difference between the experimental and calculated data in Fig. 5.9 is likely to be caused by the constantly changing environmental pressure and temperature.

5.5 Coating

The coating section is divided in three sub-sections to provide comprehensive details about the development of the coating techniques. The rheology section describes how the sol-gel transition can be manipulated by changing the chemistry. This step is important to mitigate shear forces during rotation. The coatings were initially tested in a cylinder configuration to visually inspect the coating results and to determine the required velocities as well as viscosities. With the knowledge of ideal velocity and the optimal viscosity behavior for coatings the quality of the coating can be predicted analytically and by CFD simulation. The prediction was then transfered to spherical coatings which are the ultimate goal for foam layering ICF targets. The coatings in the spherical capsules were inspected by a 2D projection of the capsules by x-rays.

5.5.1 Experimental

5.5.1.1 Rheology

The change of viscosity over time was quantitatively measured with a strain controlled Rheometrics Fluids Spectrometer (RFS 8400). Figure 5.10 shows the schematic setup of a strain controlled rheometer with a couette geometry which consists out of a cup and a bob. Other possible setups are cone and plate or plate and plate geometries. For the experiments here I used the couette geometry because of its high surface area in contact with the liquid and thus its higher sensitivity to measure even low viscosity liquids. In addition to increasing the sensitivity this setup allows a relatively simple gas seal with a lid on top of the couette to prevent evaporation. About 10 mL of the matter to be analyzed is placed in the cup so that only the walls of the bob are in contact with the liquid. The lower end of the bob entraps an air bubble and the upper end is only lowered to the meniscus of the liquid. This setup guarantees a well-defined

surface in contact with the liquid compared to a flat bottom bob which could always entrap an unknown air bubble or an increased liquid evaporation with a liquid covered bob. For the long-term viscosity measurements I placed an additional lid on the cup.

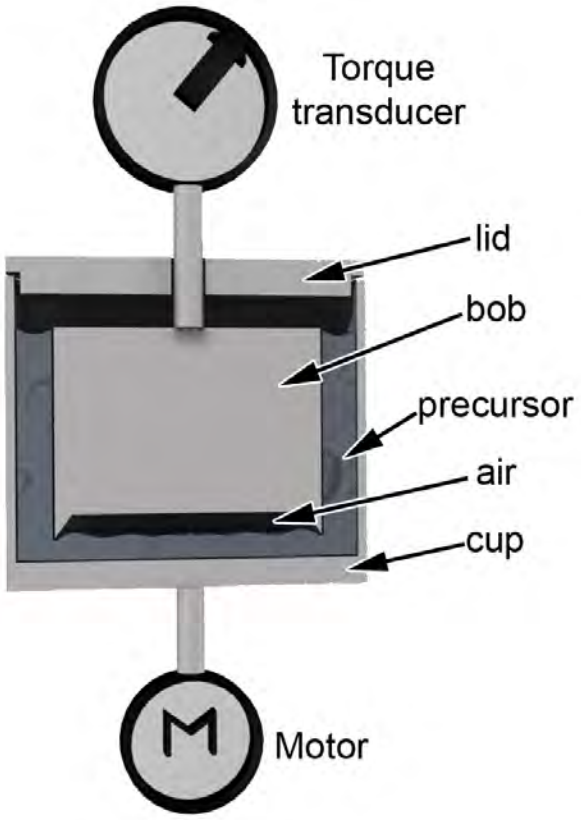

Figure 5.10: Couette geometry in a rheometer - the cross section of the couette geometry with the attached motor and transducer of the rheometer is shown. The advantage of the couette geometry is that it can be easily sealed with a lid and a relative large volume of the liquid is in contact with the wall which increases the rheometer's sensitivity. Only the walls of the bob are in contact with the liquid which leads to a very defined contact area

The viscosity is measured by applying an angular velocity to the cup (r_{cup} = 17 mm) and through the liquid the response at the bob (r_{bob} = 16 mm) is measured by the torque transducer (strain controlled). For a Newtonian fluid the quotient of the

shear stress (τ) and the shear strain rate ($\dot{y}$) is the viscosity η.

$$\eta = \frac{\tau}{\dot{y}} \tag{5.2}$$

The shear strain rate is given in a strain controlled experiment by the strain amplitude y_a and the shear rate ω:

$$\dot{y} = \omega \cdot y_a \tag{5.3}$$

The shear stress is given by:

$$\tau = \frac{T}{2 \cdot \pi r_{bob}^2 \cdot H} \tag{5.4}$$

where, T is the measured torque and H is the height of the bob (32 mm). The entire calculation is very similar to Hook's law where the Young's or shear modulus is determined by the devision of stress by strain.

For measuring polymers like our aerogels the viscosity changes over time and the transition from a liquid to a solid needs to be measured. This is a "non-Newtonian" behavior but by acquiring multiple measurements at low shear rates which do not interfere with the gelation the Newtonian fluid measurement can be used. Therefore an oscillatory measurement was used where the cup turned back and forth. The advantage of this oscillatory movement is that the time dependent phase angle (δ) between the applied strain and the measured torque (shear stress) is detected and the complex viscosity η^* can be calculated. The complex viscosity contains the storage modulus (G') and the loss modulus (G") which correspondent to elastic behavior ($\delta = 0°$) and plastic deformation ($\delta = 90°$):

$$G' = \cos\delta \cdot \eta^* \tag{5.5}$$

$$G\text{"} = \sin\delta \cdot \eta^* \tag{5.6}$$

$$\tan\delta = \frac{G\text{"}}{G'} \tag{5.7}$$

For the aerogels measured here this means that at $\delta = 45°$ the elastic component G' gets bigger than the viscous modulus G" and the sol transitions into a gel.

Here I used the Dynamic Time Sweep mode to measure at a constant frequency and amplitude over time. In this mode the motor makes the above mentioned oscillatory motion. A low strain amplitude of 5 % and frequency of 1 radian per second were used

to mitigate shear forces experienced by the gelling system while still providing a high sensitivity. 5 % strain amplitude corresponds to a 50 μm amplitude which is 5 % of the 1 mm gap between cup and bob. Matter with a viscosity as low as 1 m$Pa \cdot s$ could be measured with theses parameters.

5.5.1.2 Cylindrical coatings

Cylindrical coatings inside horizontally rotating cylinders were used to determine the best coating formulations for the spherical coatings in capsules. Instead of mounting vials into a drill chuck or gluing them on the motor shaft I used "hot-dog-rollers" to simultaneously rotate several vials. These "hot-dog-rollers" are parallel, simultaneously driven rolls where the vial is placed on top of two rolls, Fig. 5.11a). This "hot-dog-roller" technique offers a good velocity control, is self-centering for the vials and allows to place vials immediately after mixing the precursor solution.

Here I used three different "hot-dog-rollers" in different sizes to coat inside 5 to 110 mm glass cylinders (NMR-tubes – glass bottles). Figure 5.11b-d) shows an overview of the three different rollers. A preliminary steel-roller was built out of material-handling-steel-conveyor-roller which was initially driven by a controlled stirring motor and later modified to a maxon motor EC40. The rigid tolerances of the steel rolls only had a wobbling of about 20 μm. Figure 5.11b) shows a custom roller in a compact design with rigid tolerances and two aluminium rollers to hold cylinders. The commercial low profile roller from Stovall life science has up to 10 rotating rolls which rotate between 1 and 30 rpm and can accommodate up to 30 vials, Fig. 5.11c). The roller can be adjusted to vial diameters as low as 5 mm by using all 10 rolls or to bigger vials by flexibly removing every other roll. The roller is rated for temperatures up to 65 °C and can be used in an oven to gel or cure liquids during rotation. The bigger the vial the slower is the actual rotation speed because of the transmission ratio between the roller and the bottle. To rotate big vials at high speeds up to 200 rpm I designed a simple bottle roller out of cart rollers that were driven with a feedback controlled motor, Fig. 5.11d). This setup is especially designed for the 110 x 270 mm wheaton sci. glass bottles.

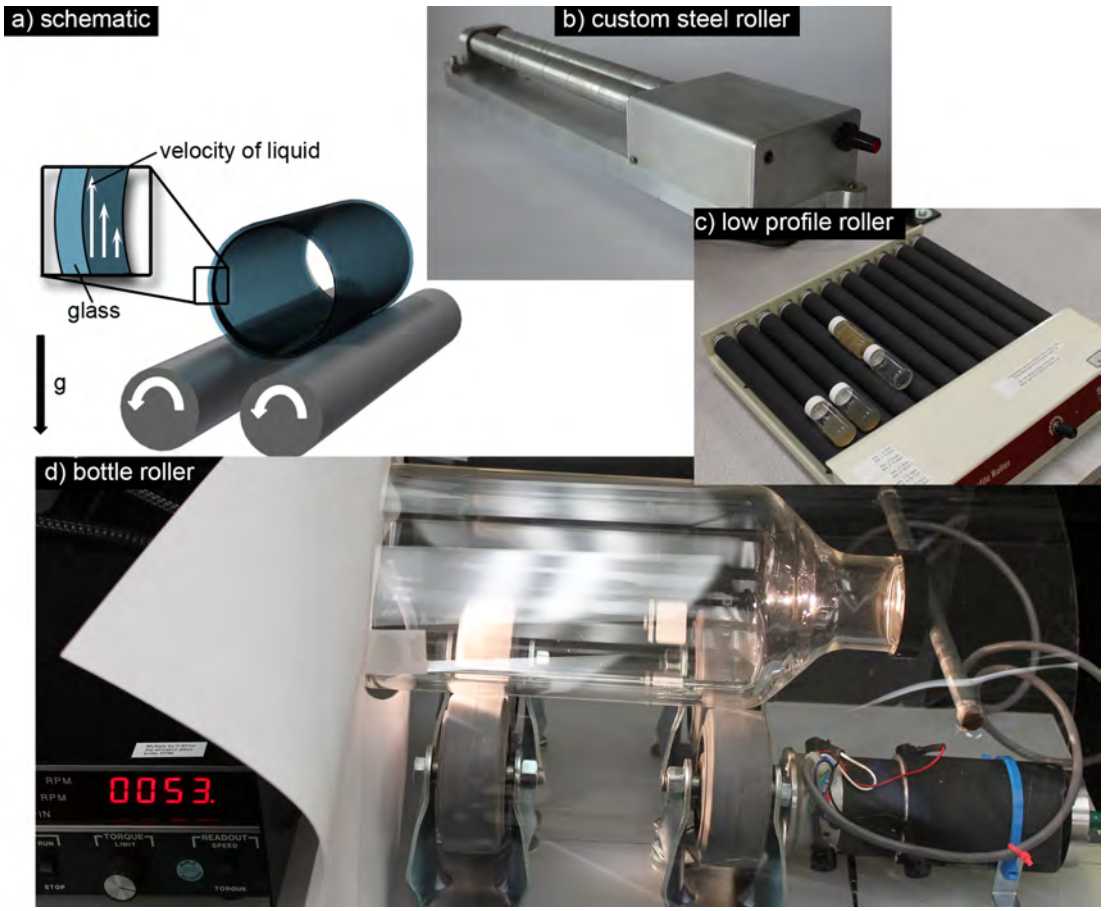

Figure 5.11: Single axis coaters - for cylindrical coatings the glass vials and bottles were placed on horizontally rotating rollers; a) schematic overview how the liquid gets distributed within the horizontally rotating cylinder; b) the steel roller which has the tightest tolerances which result in the least wobbling; c) shows the low profile roller which rotates up to 30 vials at once; d) the bottle roller enabled coatings inside 120 mm diameter vials

5.5.1.3 Spherical coatings

To circumvent the gravity in our spherical coatings I designed a random position machine (RPM) that provides a deterministic, continuous random change in orientation relative to the gravity vector thus simulating a true microgravity environment.(10) This can be achieved by a system that uses two perpendicular and independently driven frames. The capsule is mounted in the intercept point of both axes. Thus a puddle of liquid within a hollow capsule will distribute to a layer.

I designed a custom machine to fit the necessary specifications. Some of these requirements were: An accurate control over the motion with a feedback loop and speeds up to 20 rpm; temperature resistant setup to cure gels up to 80 °C; a flexible stage to allow different mounting and centering techniques for the capsule; LLNL specifications for electronic devices (e.g. UL-, TÜV-, AHJ- certifications etc.).

Figure 5.12 shows the first idea of the RPM, a schematic overview of the technical drawings and the actual device. With the idea I evaluated the concept of two perpendicular driven frames with a CATIA V5 Release V5R20 mechanics simulation, Fig. 5.12a). The two axes of the frames are highlighted with red arrows. One axis drives the U-shaped outer frame and the inner axis is only schematically shown where the capsule sits on the pole. Mechanically this setup is realized with a shaft in a shaft setup where the outer shaft drives the outer frame and the inner shaft transmits the rotation through gears to the inner frame, Fig. 5.12b) and appendix C. The rotation from the two motors is transmitted with timing belts to both shafts. The outer frame and the outer shaft are connected with a tapered fitting and secured with a lock nut. The inner shaft transmits its rotation via a pair of miter gears and another timing belt to the inner frame. In the schematic drawing no capsule holder setup is shown which is realized with a Newport xyz-stage as it can be seen in Fig. 5.12c). This xyz-stage can be mounted vertically on the inner frame or diagonally as the holes in the inner frame in the actual image indicate. This configuration allows different capsule holders and the generous space allows extra devices like battery powered vacuum chucks or additional thermal insulation around the capsule holder. Both brushless EC 60 maxon motors are equipped with an HEDL 9140 encoder, are computer controlled by EPOS2 70/10

controllers and powered by a Sorensen XHR60-18 power supply. All parts are rated to work in environments of 80°C or above, except of the controllers and the power supply which are operated outside the furnace. The device can be either controlled through the EPOS Studio maxon software or through LabView.

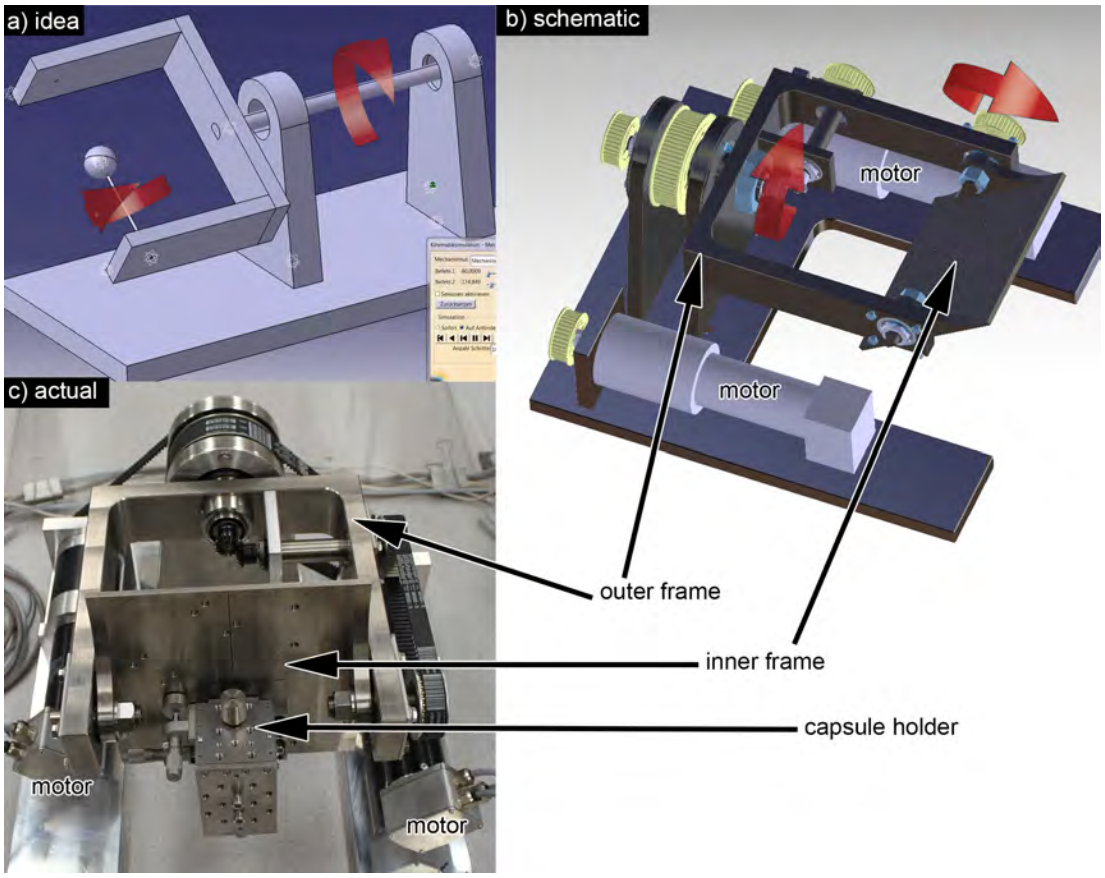

Figure 5.12: development of the two axis coater - a) shows the first schematic model of the two axis coater where one axis turns the "U" shape frame and the other axis turns the capsule; b) the CAD model of the actual two axis coater using the same driving principle as the schematic model where the rotation for the inner frames gets transmitted through an inner shaft, timing belts are not shown; c) the actual coater with the mounted xyz-stage to adjust the capsule position

In addition to the RPM I developed two other single axis coaters that rotate the capsule on one axis. The universal capsule holder mentioned above is mounted on axis on a small motor. The speed of the motor is adjusted with a variable voltage power sup-

ply. The alternative setup consist out of the steel-roller mentioned in the 2D-coatings section and steel cylinders with a tapered hole for the capsule are placed on this roller. The cylinders are further discussed below in the section for the in-situ radiographs at synchrotron beamtime.

The RPM controllers are hooked up with a computer via the USB-interface. Each controller has a unique ID to communicate to LabView. Figure 5.13 shows the LabView program I developed to run the RPM in four different modes. In all modes the parameters of the emergency stop, the mode selection and the start time, that can be used to delay the rotation, are used. In two modes only the inner frame is rotating while the outer frame can be manually leveled. In one of these modes the inner frame rotates with a fixed velocity and in the other mode the velocity is read every 10 seconds out of a text-file. The two modes where both frames are rotating have an additional ratio setting to control the speed ratio from the outer to the inner frame.

5.5.1.4 Radiography

The x-ray imaging instrument used in this research (Xradia, model: Micro XCT, Pleasanton, CA) is a bench top, high-resolution 3D X-ray imaging system for non-destructive analysis of samples with sub-micron pixel resolution. The instrument is capable for operating in x-ray microscopes mode for radiography measurements and x-ray computed tomography (CT) mode to provide 3D non-destructive imaging solution down to sub-micrometer scale. The acquired data were processed using Xradia reconstructor program (TXM) to convert images into a usable format. The radiography images are a projection and to ensure that these pictures capture the entire coating at least two images were taken, usually one frontal image and one image perpendicular to the first image. In-situ radiographs of rotating capsules partially filled with silcone oil were taken the Advanced Photon Source at Argonne National Laboratory. Beamline 2-BM was used with Peltier cooled CCD camera (Coolsnap HQ, Roper, Photometrics) with a fequency of up to 100 images per second.

5.5.1.5 Computer Fluid Dynamics Simulations

“Fluid simulations were made with conventional computational fluid dynamics (CFD) based on the Navier-Stokes equations. We used the commercial code Star-CCM+ by

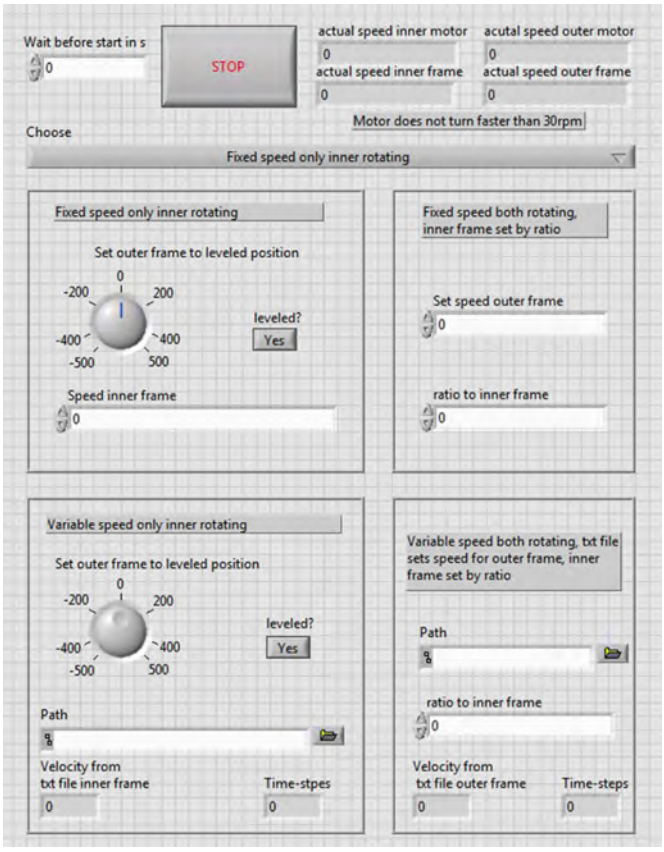

Figure 5.13: LabView control program for the two axis coater - the RPM can operated in four different modes with the LabView program; the first mode controls both axis with a fixed velocity ratio; the second mode allows to level the outer frame and run the inner frame at a set speed; the two other modes additionally include a time dependent velocity

CD-Adapco (Melville, NY, USA). The simulations were two-phase (air and liquid) using the volume-of-fluid (VOF) method. The problem was meshed with coarse polyhedra for the center region (containing air only) with a 15-layer prism mesh at the wall region containing the liquid (the outer 8 mm near the wall). The liquid was simulated as Newtonian, specifying a surface energy of 0.02 Jm^{-2} and density 0.88 $\frac{g}{cm^3}$, taken from a typical silicone oil, and a contact angle of 0°. No parameters were adjusted to improve agreement with experiment. The computations were 3D at the actual physical scale and idealized the vials as cylinders. A typical calculation took 3 days on 2 Intel Xeon CPUs to simulate 30 s wall-clock time for a steady-state solution."(19)

5.5.2 Results and Discussion

5.5.2.1 The rheological properties

The knowledge and the tuning of the viscosity *vs.* time are essential to understand shear conditions in a moving gelling system. The resulting shear forces during rotation in the flowing precursor solution can damage the initially fragile gel network. Thus the viscosity *vs.* time behavior and rotation parameters need to be analyzed to limit the damage to the gel network. Here, I first validate the viscosity *vs.* time measurements by verifying the instrument's calibration with viscosity standards. Then the analytical gel-point was compared with the actual sol-gel transition by turning vials with gelling precursor solution up-side-down. Finally I will show a co-polymerization approach to tune the gelation behavior by modifying the degree of cross-linking in the gel network.

Figure 5.14 shows the viscosity *vs.* time behavior of a pure 50 and 25 $\frac{mg}{cm^3}$ PDCPD gel in toluene. Both gels are dominated by an unchanged viscosity of toluene (0.56 m$Pa \cdot s$) in the beginning followed by a steep increase in viscosity. The gelation of the 50 $\frac{mg}{cm^3}$ gel occurs faster compared to the 25 $\frac{mg}{cm^3}$ gel. Both graphs are corrected for a delay from mixing the gel and adding it to the viscometer. As commonly known references I added the viscosity of water 0.9 m$Pa \cdot s$ and honey 10 $Pa \cdot s$ on the right side.

5.5.2.1.1 Instrument calibration To ensure accurate viscosity measurements the rheometer calibration was verified with silicone oil reference standards. Figure 5.15 shows two reference measurements perfomed in dynamic strain sweep. In this mode the

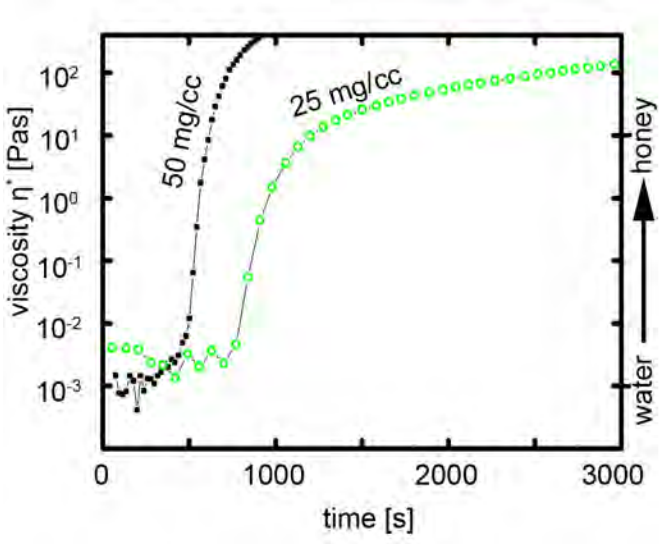

Figure 5.14: viscosity *vs.* time behavior of 25 and 50 $\frac{mg}{cm^3}$ PDCPD gels - the viscosity of the 50 $\frac{mg}{cm^3}$ aerogel increases much faster than the 25 $\frac{mg}{cm^3}$ PDCPD gel. In the beginning the viscosity was not sufficient to acquire a reliable signal while at high viscosities this fluctuation disappears.

frequency is constant at 10 $\frac{rad}{s}$ and several measurements with different deformations between 25 % and 250 % strain are performed. The Newtonian silicone oil in this measurement showed viscosities close to the target value for all strain rates which indicates that the instrument is well calibrated. The $0.941 Pa{\cdot}s$ silicone oil measurement stopped at 150 % strain because of the limit of the torque transducer.

5.5.2.1.2 The gel point - sol-gel transition The point where the sol turns into a gel that does not flow anymore is defined as the sol-gel transition or gel point. Depending on the gel this gel point can occur quickly at a low viscosity or after the sol went through a highly viscous phase which depends on the cross-linking characteristics of the sol to be tested. A rough approach to check whether a sol already reached the gel point is the shaking method by observing the gel while gently shaking the precursor in a vial.(56) For a rheometry experiment the gel point can be defined as the phase angle $\delta = 45°$ which is the crossover of the elastic- (storage, G') and viscous- (loss, G") modulus.(94, 98)

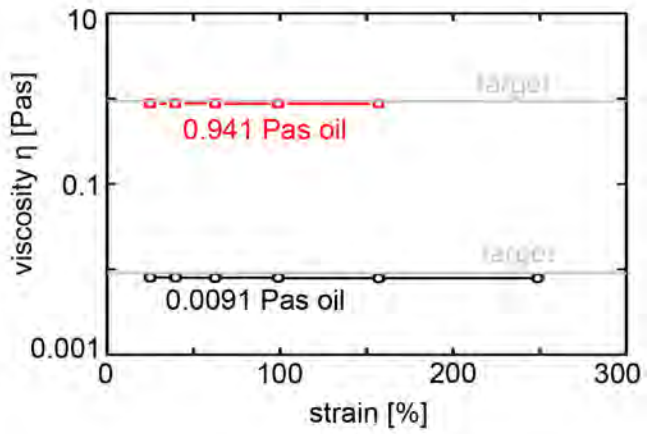

Figure 5.15: Reference measurements with silicone oil - a dynamic strain sweep measurement was performed to validate that instrument is calibrated accurately; both measurements with 0.941 and 0.0091 $Pa \cdot s$ are only slightly below the target viscosity. For sol-gels which are not ideal Newtonian fluids the shear rate was low enough to ensure that the oscillatory measurements did not interfere with the gel. By comparing the measurement with the gelation in stationary vials the harmless oscillation of the instrument was verified.

In Fig. 5.16 the measurement of both moduli of a 50 $\frac{mg}{cm^3}$ PDCPD, 0.2 wt.% catalyst are displayed with actual vials used in the shaking method as comparison to verify the rheologically measured gel points. As expected the liquid does not store any energy in the beginning, G' is almost zero and the precursor within the vial is a simple liquid. As soon as G' increases the liquid gets lumpy and G' crosses G" reaching the gel point. By comparing the rheometry result with the shaking method the gel point is always reached about 5 – 15 % later in the shaking method. The gel point of the shaking method is shown in the last picture with vial 10 where the gel stays at the bottom of the vial. Here I use the G' = G" method to determine the gel-point because of its high reproducibility even for high viscosity liquids.

For 50 $\frac{mg}{cm^3}$ PDCPD 0.2 wt.% catalyst concentration seem to be ideal based on the systematic evaluation in Figure 5.17. Gelation with 0.2 wt.% catalyst occurs in an reasonable timeframe, even for lower densities. With less than 0.2 wt.% catalyst concentration results were not as reproducible anymore because of small experimental deviations. Higher concentrations are not desirable due to the requirement of having a low atomic number pure CH_x-gel. Grubbs catalyst mostly consists out of ruthenium

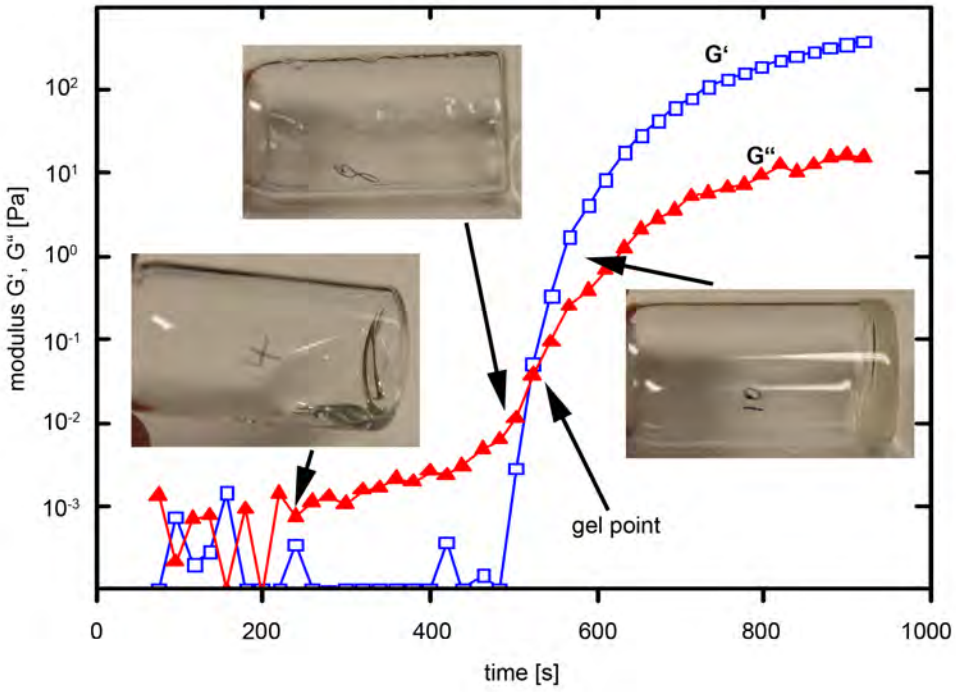

Figure 5.16: The elastic and plastic moduli *vs.* time for a PDCPD gel - initially the elastic modulus G' is very low since liquid cannot store any energy. As G' increases the gel network forms and some lumps are visible in the center vial. After G' crossed G" a weak gel is present which is shown by the vial containing the gel on right

which is a high atomic number element and is not desired for ICF targets. Lee et. al. reported a similar catalyst concentration - gel point dependency earlier where the catalyst concentration is shifted one order higher in magnitude.(56) This shift might be caused by lower purity starting materials that deactivate the catalyst and considerably slow the experiment.

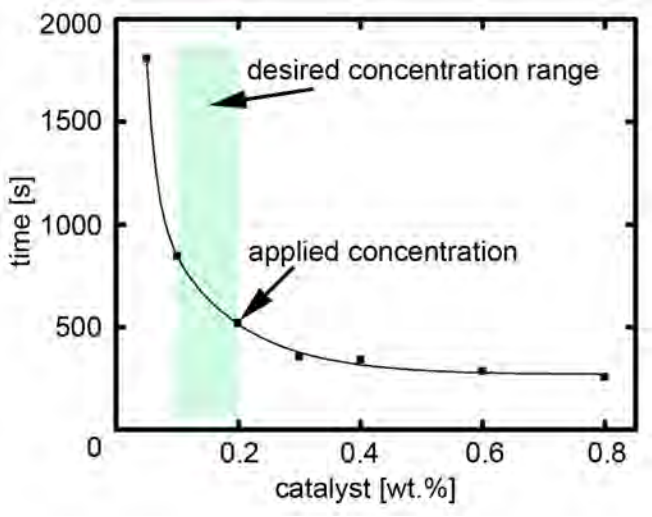

Figure 5.17: The influence of catalyst on the gel time - values above 0.2 wt% deliver highly reproducible results. The green bar marks the best compromise between gel time reproducibility and allowable catalyst incorporation

5.5.2.1.3 The co-polymerization approach To tune the viscosity over time behavior a co-polymerization approach was developed by adding NB to the PDCPD gel. In Fig. 5.18a) the addition of NB reveals an increase of viscosity and delay of the gel point. Concentrations between 1-10 wt.% NB were added and the higher the NB concentration the higher the gel point while the slope of the viscosity over time decreases. Figure 5.18b) summarizes these results by emphasizing the time and viscosity at the gel point *vs.* the NB concentration. The effect of increasing the NB concentration is almost linear in time for up to 5 % NB and for 10 % NB the gelation occurs faster than expected on this linear trend. The dependency of the viscosity at the gel point on the NB concentration is even more pronounced. Without the addition of NB the gel point is at about 0.05 $Pa \cdot s$ while the viscosity at the gel point for 10 wt.% NB is two orders of magnitude higher at 9 $Pa \cdot s$. In a common reference this is about the change from

olive oil 0.08 $Pa \cdot s$ to honey 10 $Pa \cdot s$. The same influence of NB on the gel point was observed for 25 $\frac{mg}{cm^3}$ P(DCPD-r-NB) gels in Fig. 5.19. The impact of NB on 25 $\frac{mg}{cm^3}$ gel is similar but the slope of the viscosity increase is much slower since the overall density is lower.

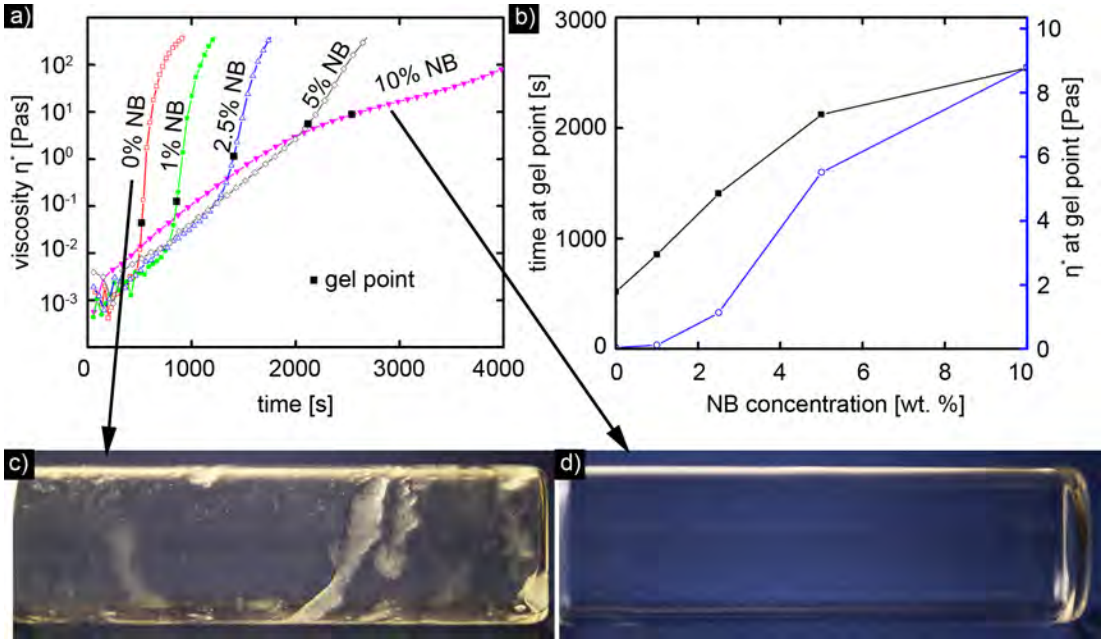

Figure 5.18: The influence of co-polymerization on homogeneous coatings - norbornene (NB) addition on the gelation of a 50 $\frac{mg}{cm^3}$ PDCPD gel in toluene with 0.2 wt.% catalyst; a) the addition of NB decreases the slope of the viscosity; b) the higher NB concentration increases the gel time and the viscosity at the gel point; c) 500 μL precursor solution in the 10 mL glass ampoule rotated at 10 rpm during gelation shows many inhomogeneities; d) rotated with the same parameters but with 10 % NB added to the PDCPD gel shows a uniform 180μm thick gel layer

For coating applications the change of the viscosity *vs.* time behavior and gel point can lead to in-homogenous coatings, Fig. 5.18c-d). Both 10 mL glass ampoules were rotated as schematically shown in Fig. 5.18a) on the low-profile roller at 10 rpm with 500 μL 50 $\frac{mg}{cm^3}$ precursor solution. The vial with pure PDCPD shows lumps while the 10 wt.% NB gel film formed a smooth uniform layer. This indicates that the small addition of 10 wt.% NB changes the gel network and makes it more rigid regarding shear forces during rotation. The classical theory of gelation can qualitatively explain

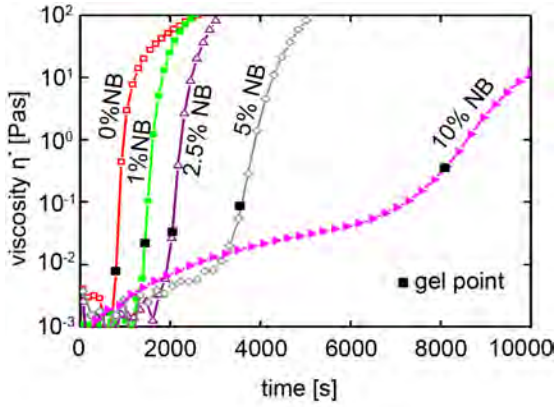

Figure 5.19: The influence of co-polymerization on 25 $\frac{mg}{cm^3}$ P(DCDP-r-NB) - in comparison to Fig. 5.18 the 25 $\frac{mg}{cm^3}$ gel with 0.2 wt.% catalyst shows the same influence of the NB on the gel. The gel point drops because of the lower density of the gel

this change in gelation behavior for polymer based networks. This theory predicts that gelation occurs as soon as the fraction p_c of all bonds that could possibly be connected reaches:

$$p_c = \frac{1}{z-1} \tag{5.8}$$

where z is the functionality of the polymer. Pure PDCPD has a functionality of four because of its two double bonds while NB only has a functionality of two because of the single double bond. This classical theory of gelation predicts for PDCPD the gelation when one third of all bonds are connected. The addition on NB lowers the functionality z and therefore the amount of bonds required for gelation increases and the gel point is reached at a higher viscosity. The theoretical and the experimental results are good agreement with each other since both predict an increased gel point for increasing NB concentrations. Ito et al. and Yang et al. observed a similar trend for block-propolymerization of resorcinol (z =3) with phloroglucinol carboxylic acid (z = 2) and for replacing resorcinol by phloroglucinol carboxylic acid.(48, 114) In addition to validate our hypothesis of the impact of the functionality on the gelation we performed the co-polymerization approach with crosslinking co-monomers which had a functionality above 4 and gelation occured much quicker sometimes almost instantly.

5.5.2.1.4 TiO_2-, Fe_2O_3- and SiO_2- gels In Figure 5.20 I characterized TiO_2-, Fe_2O_3- and SiO_2- gels by rheometry to compare their gelation behavior to PDCPD

gels. The gel point of the different gels is highlighted with black squares. The 50 $\frac{mg}{cm^3}$, 10 wt.% P(DCDP-r-NB) shows the same gelation as in Fig. 5.18a) with its almost linear increase in viscosity and relatively high gel point at 9 $Pa \cdot s$. The SiO_2 is very similar to the P(DCPD-r-NB) but the increase in viscosity starts after a delay period. The gel point is a bit lower at 2 $Pa \cdot s$ while the slope of the viscosity increase is almost the same. In comparison the Fe_2O_3 gel has a low gel point at 0.02 $Pa \cdot s$ with a steep almost instant increase in viscosity. The viscosity of the TiO_2 gel increases a bit slower than the Fe_2O_3 gel and reaches the highest gel point of all four gels at 27 $Pa \cdot s$. The initial bump in the TiO_2 curve is probably caused by the temperature increase after filling the ice cold precursor in the rheometer at room temperature. The different impact of the gel point and speed of gelation is discussed in chapter 5.5.2.2.3.

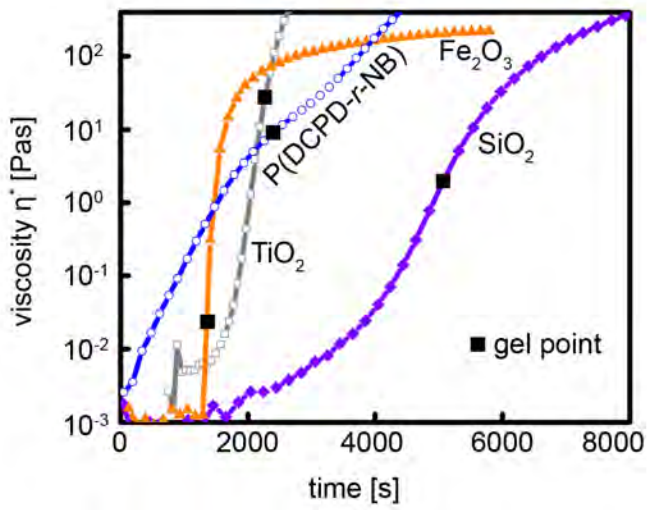

Figure 5.20: Viscosity *vs.* time of P(DCPD-r-NB), TiO_2-, Fe_2O_3- and SiO_2 aerogel - the viscosity of the P(DCPD-r-NB) aerogel increases almost linearly and has a viscous gel point, the TiO_2 gel has a very steep increase in viscosity with a viscous gel point, the Fe_2O_3 is very similar with the step increase in viscosity but has a relative low gel point, the SiO_2 is similar to the P(DCPD-r-NB) gel but the gelation is a bit slower

5.5.2.2 Cylinder coatings

The motion of the liquid within a partially filled horizontally rotating cylinder can reach three different states. The states are dependent on the rotational speed, the dragging forces of the viscous liquid and the gravity. At low rotation speeds the puddle

at the bottom builds a recirculating region and a distinctive edge parallel to the axis of rotation develops.(104) The position of this so called rimming edge is determined by the viscous drag and the gravity. This state is referred to as the rimming flow. With increasing the rotational speed of the cylinder the rimming edge separates in multiple edges; called the unstable state. Thoroddson experimentally characterizes several different instabilities that develop in various liquids.(104) At high speed all edges disappear and the liquid forms an almost uniform layer within the cylinder. In reference to the glass cylinder the liquid layer is slightly non-concentric because of the gravity and drag adding up in the rotational direction on one side of the glass cylinder and on the other side the drag fights the gravity. This almost uniform state is called the rimming state and is the desirable state for uniform coatings.

5.5.2.2.1 Melos and Moffats analytical approximation Melo and Moffat developed an approximation based on the dimensionless parameter Λ to determine the critical speed ω_c for the rimming flow, unstable state and rimming state:(64, 68)

$$\omega_c = \frac{\Delta \cdot g \cdot \bar{h}}{R \cdot \nu} \tag{5.9}$$

This approximation is based on the parameters shown in Fig. 5.21 which are the radius of the glass cylinder (R), average layer thickness of the distributed film ($\bar{h}$), kinematic viscosity (ν), acceleration of gravity (g) and angular velocity (ω). The angle θ in Fig. 5.21 will be used as comparison for the experimental and simulation results.

Melo and Moffat derived Λ from the Navier-Stokes equation with a slow flow of a thin layer with insignificant inertial effects (the lubrication approximation). According to their calculation at Λ=2.06 the liquid transforms into the uniform rimming state. Unfortunately the lubrication approximation cannot be used to predict the instable state where the rimming flow and state coexist. Melo further investigated the three different states and experimentally confirmed the analytical value of Λ=2.06 with Λ=2.14. In addition he found the transition from the rimming flow in the instable flow to be at Λ=1.56.

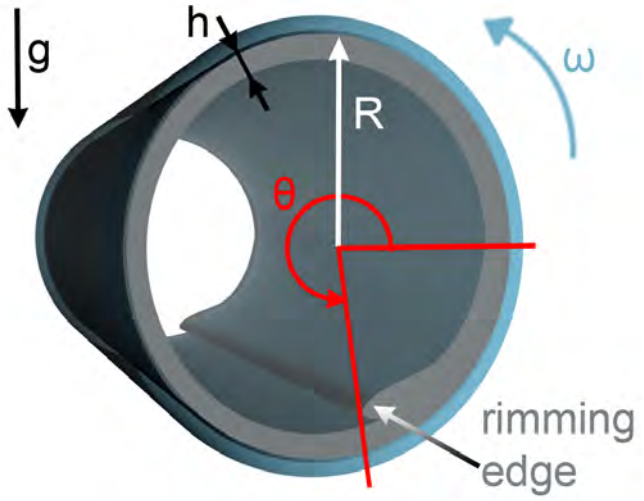

Figure 5.21: The parameters of rotating liquid in a cylinder - the rimming edge is formed by the recirculation of liquid in a horizontally rotating cylinder. The cylinder is rotated at velocity ω that creates a dragging forces at the cylinder wall that pull the liquid up while the gravity pulls the liquid down. The angle θ is defined between a horizontal plane of the cylinder and the rimming edge

To achieve uniform coatings the analytical approximation suggests that the viscosity and the rotational speed can be changed. The radius and the layer thickness are given in the requirements for the coatings. The dynamic viscosities I measured are the product of the kinematic viscosity and the density of the aerogel. Consequently by controlling the viscosity over time behavior and the rotational speed the shear forces which disrupt the gel network and build irregular gel fragments (Fig. 5.18c) can be mitigated to form uniform layers. In Fig. 5.18d) a uniform coating was achieved only by changing the viscosity over time characteristic. The viscosity before the gel-point was increased which allowed the glass cylinder walls to drag up the viscous sol and avoid shear forces in the recirculating puddle. In the next chapters I expand this approach by additionally changing the rotational speed to determine the coating limits.

5.5.2.2.2 Silicone oils To validate the analytical approximation I first used silicone oil with a fixed viscosity to check the transition predictions. The roller glass bottles were filled with either 100 mL or 200 mL of 485 m$Pa \cdot s$ silicone oil and rotated on the bottle roller at various speeds. The equation for the approximation predicts the transition from the rimming edge into the unstable region at 64 rpm (Λ=1.56) and in

the rimming state at 87 rpm (Λ=2.14) for 200 mL. Figure 5.22a) shows one example for the rimming edge condition at 40 rpm and b) for the unstable region at 60 rpm. The pictures were taken through the bottom of the glass bottle in the axis of rotation and after about 30 seconds of rotation at the desired speed to capture the steady state of the liquid.

The results of the comparison are summarized in Fig. 5.22c) including the position of the rimming edge. The rimming state is defined at theta = 360°, c.f. Fig. 5.21. In the rimming edge region theta increases linearly with the rotation speed up to 54 rpm where the transition in the unstable region occurs. The unstable region experimentally transitions into the rimming state between 92 and 108 rpm. I observed that at slow acceleration of the glass bottle the unstable region reaches into higher rotational speeds while the rimming state develops earlier at a fast acceleration from no rotation to a high velocity. Because of this overlapping of the unstable state and the rimming state the deviation between experimental data and analytical approximation is between 6 and 20 %.

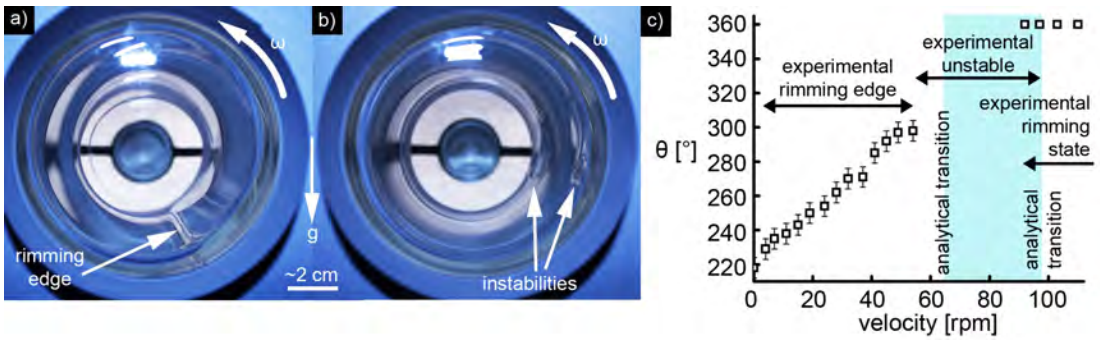

Figure 5.22: theta of silicon oil in a rotating cylinder - a) shows the rimming edge of 200 mL silicone oil (485 $mPa \cdot s$) in a 103 mm diameter glass bottle rotated at 40 rpm; b) with increasing speed to 60 rpm instabilities develop; c) summarizes the states of the silicone oil experiments where the rimming edge is up to 64 rpm and the uniform rimming state starts between 92 and 108 rpm with the unstable region in between. Equation 5.9 predicts the analytical transition

5.5.2.2.3 P(DCPD-r-NB), TiO_2-, Fe_2O_3- and SiO_2- coatings With the knowledge of the viscosity *vs.* time behavior in Fig. 4.16 and the analytical approximation

I was able to predict the optimal coating velocity and the maximum achievable layer thickness at this velocity. To limit the shear forces experienced by the gelling system under rotation a viscous liquid is desirable because it gets dragged up by the moving glass cylinder wall more easily. Especially for aerogels which can get irreversibly damaged by tearing the gel network apart it can be important to start the coating in the rimming state. This means the coating gets delayed until the sol reaches the desired viscosity. In addition, according to the analytical approximation a viscous liquid before the gel point enables thicker aerogel coatings without increasing the rotational speed. The viscosity *vs.* time behavior of the P(DCPD-r-NB)- and SiO_2-gel is promising because of the slow, linear increase in viscosity and the high gel-point. For Fe_2O_3-gels the time frame for coating is really narrow because of its rapid increase in viscosity and relatively low gel point. The low viscosity at the gel point limits the maximum layer thickness to a thin coating. The TiO_2-gel is a combination of behaviors of the P(DCPD-r-NB)- , SiO_2- and Fe_2O_3-gels with a steep increase in viscosity and a high gel point. This rapid increase makes the timing for the coating more challenging.

The coating viscosity was chosen to be in the coatable time frame with a viscosity that still easily spreads. I avoided the unstable region by transitioning the precursor with the desired viscosity from the rimming flow directly to the rimming state. Wetting of the glass surface was ensured by rotating the glass bottle several times at 3 rpm before the coating. Figure 5.23a) shows a dyed 50 $\frac{mg}{cm^3}$ 10 wt.% NB P(DCPD-r-NB) gel with a 650 μm layer. I started the coating at 22 rpm after 17 min where the viscosity should be around 0.1 $Pa \cdot s$ to start the coating immediately in the rimming state. Visual inspection of the coated layer reveals the instability effect of band separation on both sides of the bottle while the center has an uniform layer. The SiO_2-gel layer in Fig. 5.23b) has the same thickness with 650 μm and to simplify the visual inspection dye was added after gelation. The coating started after 75 min (0.2 $Pa \cdot s$) where I transitioned the precursor suddenly into the rimming state at 32 rpm. The layer is relatively homogenous except of a few irregularities on the right side of the bottle. These irregularities are probably a few drops that diagonally flowed off and gelled. Because of the rapid increase in viscosity for the TiO_2- and Fe_2O_3-gel the time frame which allows coating is really narrow. Thus I rotated both glass bottles at 7 rpm from the beginning until I observed rising of the rimming edge (θ increases) that indicated a

viscosity increase and that is where I transitioned the precursor into the rimming state. For the Fe_2O_3-gel I observed the tilting rimming edge after 40 min and increased the speed to 100 rpm. This highest speed of 100 rpm only leads to a centrifugal acceleration ($\omega^2 \cdot r$) that is 50 % of the gravitational acceleration. By contrast with the rheology viscosity *vs.* time measurements the viscosity increase should occur after 20 min. This difference indicates shear forces within the circulating precursor puddle during the 7 rpm rotation and thus delaying and damaging the gel network. The coating result of the Fe_2O_3-gel showed good uniformity of the 160 μm thick layer except of thinner coatings at both sides of the bottle, Fig. 5.23c). I had to reduce the layer thickness to 160 μm because of the low viscosity before the gel point which only supported thin layers. For the TiO_2-gel I accelerated the precursor after 30 min to 32 rpm into the rimming state. Initially some irregularities were visible in the rimming state but with the viscosity increasing over time the gel turned into a homogenous coating, Fig. 5.23d). The inhomogeneities observed here are not dependent on uneven glass cylinder walls since they are reproducible in different glass cylinders.(104)

With the guidance of the analytical approximation in combination with the viscosity *vs.* time behavior uniform aerogel coatings can be applied by using the rimming state, Table 5.1. I "deliberately used higher speeds for the coatings to compensate for the error determined with the silicon oil and for possible viscosity offsets. For the CH-aerogel coating the theoretical rotation speed should be 14 rpm according to Eq. 5.9, which is in reasonable agreement with the 22 rpm of the actual coating. The calculation for the thin Fe_2O_3-aerogel is 80 rpm that agrees well with the actual speed of 100 rpm. For TiO_2- and SiO_2-gels, however, Melo's approximation yields a rotational velocity of 13 rpm for 0.1 $Pa \cdot s$ which does not agree with the experimental observation. Instabilities were still observed at 22 rpm, and increasing the rotational velocity to 32 rpm was necessary to drastically improve the quality of the coating. Thus the theoretical prediction can only be used as a rough guide, which is especially true for the transition of the rimming edge to the unstable region and rimming state. Melo's approximation and the lubrication approximation do not take into account surface tension and inertia, which are shown to have significant effects.(3, 44)"(19)

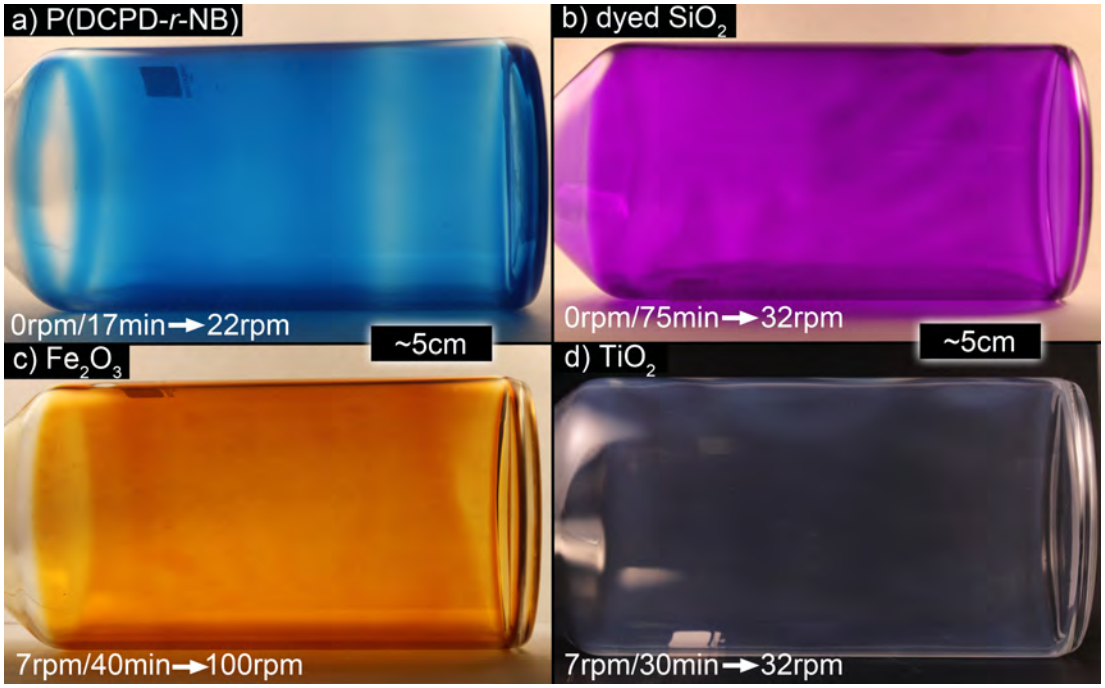

Figure 5.23: Aerogels coated inside glass cylinders - all coatings were obtained in the rimming state according to table 5.1. a) shows some instability bands at the sides; b) shows a few drops at the upper right that flowed off diagonally; c) a small uncoated spot is visible at the upper left; d) an uniform layer

Gel system	**Sol-gel transition** $[Pa \cdot s]$	**Sol-gel transition** $[min]$	**Layer thickness** $[\mu m]$	**Rotation start time** $[min]$	**Viscosity at start** $[Pa \cdot s]$	**Angular velocity** $[rpm]$	**Equation 5.9 velocity** $[rpm]$	**Layer quality**
PDCPD	9	40	650	17	0.1	22	14	good
SiO_2	2	85	650	75	0.2	32	7	good
Fe_2O_3	0.02	23	160	40	0.01	100	80	very good
TiO_2	27	38	650	30	0.1	32	13	excellent

Table 5.1: Coating results - the quality and parameters of the coatings in Fig. 5.23

5.5.2.2.4 CFD-simulations The above mentioned experiments were used as benchmark for CFD-simulations that are required for the understanding of coatings in 2 mm spherical capsules. Here, I verify the CFD- code with the silicone oil experiments to ensure that the code captures the liquid behavior. Figure 5.24 shows the three different states captured by the simulation. The rimming edge in Fig. 5.24a) is clearly visible in the lower right part while the remaining liquid forms a film around the circumference. Blue is the air within the simulation, red is the liquid and colors in between mark a mixture of air and liquid that are caused by the averaging of partly filled cells in the simulation. The simulation shows one slice through the glass cylinders and the rotation parameters are the same as in Fig. 4.18a). The rimming edge is almost at the same position in both pictures. Figure 5.24b) shows the simulation of instabilities at 60 rpm in the projection of the unwrapped cylinder wall. The colors indicate the thickness variations of the layer. In comparison with Fig. 5.22b) which is rotated with the same parameters two instabilities occur at roughly the same position even though a detailed review of the flow of liquids in horizontally rotating cylinders found that CFD simulations can determine the boundaries of instabilities, but usually not the detailed instability behavior.(96) In addition deviations from a Newtonian liquid, using an imprecise surface tension and having a different wetting behavior affect the simulation. The simulation of the rimming state at 100 rpm is shown in Fig. 5.24c). As expected one side of the cylinder is thicker than the other side which is caused by the balance of viscous drag and gravity. Visual inspection of the rimming state in experiments did not show a distinguishable difference and I could not compare the thickness variations with the simulation. The simulation has a thickness difference with a factor of about two. For simulations with aerogels which have an increasing viscosity over time this effect of a thick and a thin side disappears.(19)

For a better comparison the simulation results are compared with the experimental result in Fig. 5.25. In the rimming flow region I compare the angle theta and for the unstable region as well as the rimming state region their points of transition. The experimental determination of θ has an error of $\pm 6^\circ$ because of small alignment errors, the accuracy of the motor readout, lensing effects of the liquid on the bottom of the bottle, angle determination uncertainties and the high sensitivity to leveling errors in the bottle at fast velocities. The large glass bottles were used to mitigate the meniscus

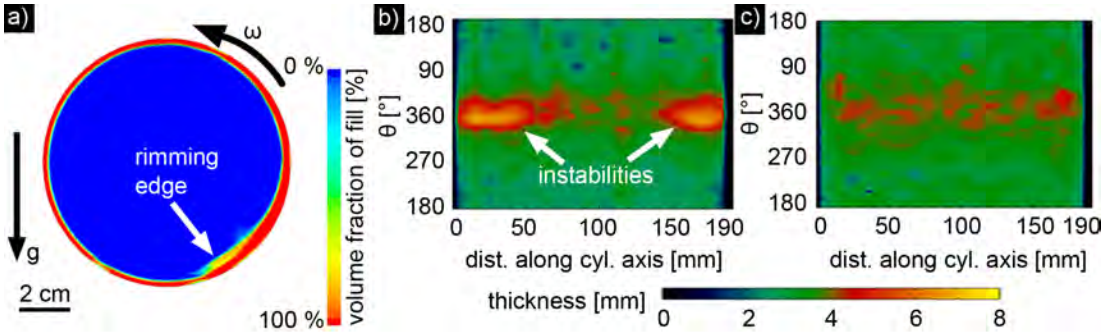

Figure 5.24: The simulation compared to the experiment - CFD simulation of the same parameters as in Fig. 5.22; a) cross section of a cylinder showing the rimming edge at the same position as in Fig. 5.22; b) the projected thickness distribution of an unwrapped cylinder shows instabilities at 60 rpm; c) the rimming state reached in a simulation showing a slightly thicker part at 360°

effect that pulls up liquid at bottom of the bottle and distorts the liquid distribution. The determination of θ in the simulation has an error of $\pm 5°$ due to the simulation cells that can contain a mixture of air and liquid without distinct border to pure liquid. The measurements in the unstable region are marked by huge "error bars" which indicate that no theta measurement is possible. The simulation and experimental theta measurements in the rimming flow almost match perfectly. The transition into the unstable region is expected to be between 50 and 60 rpm in the simulation which agrees with the experimental value of 54 rpm accurately. At 100 rpm the simulation reaches the rimming state right in the middle between the experimental values of 92-108 rpm. In contrast to the analytical approximation the simulation included surface tension and inertia which improved the prediction. In summary the rimming state for homogeneous coatings can be predicted and the analytical approximation can be used as guidance.

5.5.2.3 Spherical ablator shell coatings

5.5.2.3.1 RPM validation To achieve coatings within the capsules I first investigated coating patterns which would uniformly distribute the precursor. To simulate these coating patterns I plotted:

$$x = r \cdot \sin\phi \cdot \cos(a \cdot \phi) \tag{5.10}$$

$$y = r \cdot \sin\phi \cdot \sin(a \cdot \phi) \tag{5.11}$$

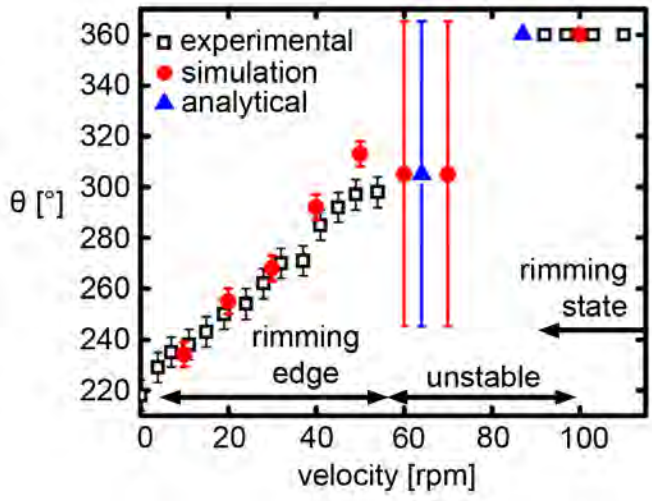

Figure 5.25: experimental, analytical and simulation results summarized - in the rimming edge region the angle θ of the experiment agrees well with the simulation data. The simulation and analytical approximation 5.9 predict the transition into the unstable region reasonably well. The transition into the rimming state depends on the acceleration and can only be roughly predicted.

$$z = r \cdot \sin \phi \tag{5.12}$$

where r is the radius of the capsule, ϕ an angle which gradually increases and a the speed ratio between both axes of rotation. Figure 5.26a) shows the coating with a speed ratio of 2. By changing this rational number the pattern changes but the track repeats itself again and again. This changes by using an irrational number like $\sqrt{2}$ which is shown in Fig.5.26b). This projection has two poles where the projection frequently intersects but the rest of the projection is uniformly distributed on the sphere. The pattern shown here stops after about 12 revolutions and the lines on the sphere would get denser after more revolutions. This uniform distribution on a sphere seems to be true for all irrational numbers leading to an incommensurable result tested here. Figure 5.26c) shows the first coating with this $\sqrt{2}$ pattern in a glass bead. This bead is out of glass decoration with an uneven surface. Other than the inhomogeneities caused by the uneven surface the SiO_2-aerogel distributed well and coated the entire capsule.

5.5.2.3.2 Concentricity, sphericity and surface roughness The parameters achieved in concentricity, sphericity and surface roughness are combined in a power

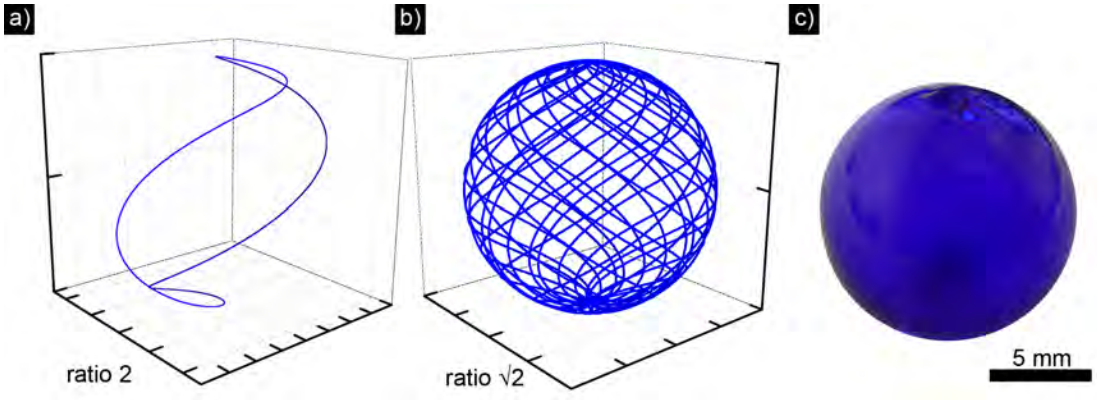

Figure 5.26: Paths on a sphere - a) shows the track of one point on a sphere if the two independently driven frames rotate in a velocity ratio of 2. The track does not change. b) with an irrational ratio the track constantly changes and liquid would be uniformly distributed. c) a glass bead coated with dyed SiO_2 aerogel using the $\sqrt{2}$ ratio

spectral density plot (PSD) obtained from a Fourier Transformation. For this analysis the position of the vapor – gel interface r(θ) is measured and this data is then converted to a PSD. A custom developed code was used for the vapor - gel interface which automatically detects the interface in the radiographs by contrast. Figure 5.27 shows a power spectrum of one of the coated capsules with the desired specification and the actual achieved modes. The first 6 modes of the PSD benchmark the shape of the gel layer where mode 1 means non-concentricity, mode 2 an egg shape, mode 3 a triangular deformation, etc.. Modes 7 to 128 determine the roughness of the gel layer.(53) The quality of the PSD here is limited by the resolution of the radiography images and hence I focus on the modes between 1 and 15.

5.5.2.3.3 Capsule coatings Figure 5.28 summarizes the systematic approach to achieve uniform coatings. For the first capsules coated I used the analytical approximation for cylinders as guidance to find a good starting velocity and an irrational ratio of $\sqrt{2}$ as coating pattern to uniformly distribute the precursor. By assuming a viscosity of 0.05 $Pa \cdot s$ that is even below the gel point for pure PDCPD gels and a layer thickness of 50 μm the analytical approximations suggest 8.5 rpm for the rimming state. With this guidance I used a velocity of 10 rpm for the inner frame and 14.14 rpm for the outer frame. Figure 5.28a) shows the coating of a 50 μm layer with 50 $\frac{mg}{cm^3}$ and 15 wt.% NB within a 2 mm diamond capsule. The start of the rotation on

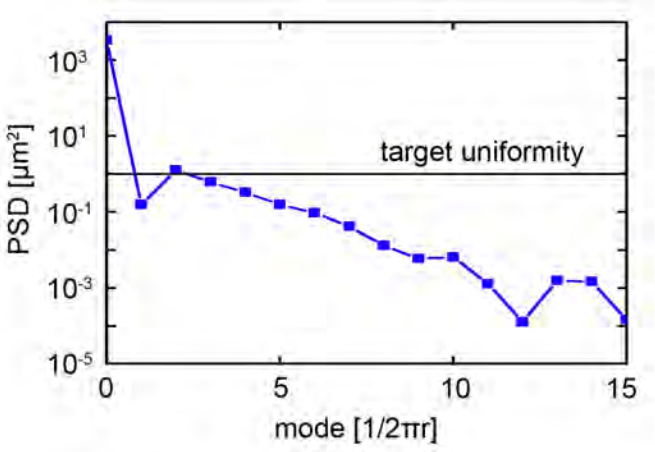

Figure 5.27: PSD - the mode number analysis of diamond capsule 80 showing a mode 2 deviation out of the desired uniformity. Mode 1 basically means non-concentric, mode 2 an egg shaped geometry, mode 3 a triangle shaped geometry, etc.

the RPM was only delayed for about 3 min by the mixing of the precursor and filling of the capsule which is well before the viscosity increase. The capsule shows a small mode one non-concentricity. The PSD of this capsule confirmed this mode 1 deviation from the desired specification. Figure 5.28b) investigates the tilting of the RPM which supposedly moves the frequent intersected poles in the coating pattern to a different position. In the 0° image the left part is still thicker than the right part. The tilting of the RPM does not seem to have any influence on the mode 1 non-concentricity. The thicker part at the bottom of the capsule is caused by residual solvent which gets into the capsule while the capsule was stored in toluene after the coating finished. In the following two Fig. 5.28c-d) the influence of the speed variation is systematically investigated. In c) the speed was increased by 100 % and in d) the speed was reduced by 50 %. Both pictures do not meet the mode one specification.

In the next step I tried a single axis rotation as comparison to the two axis rotation. In Fig. 5.28e) the single axis coating with 25 $\frac{mg}{cm^3}$, 15 wt.% NB lead two an almost perfectly spherical coating within the capsule. Only one small indent next to the fill hole is visible in the 90° image at the upper right part. With exactly the same parameters this coating was not reproducible within 8 tries. Consequently I tried to change the speeds to achieve uniformity. Figure 5.28f) shows the coating at 1 rpm which leads

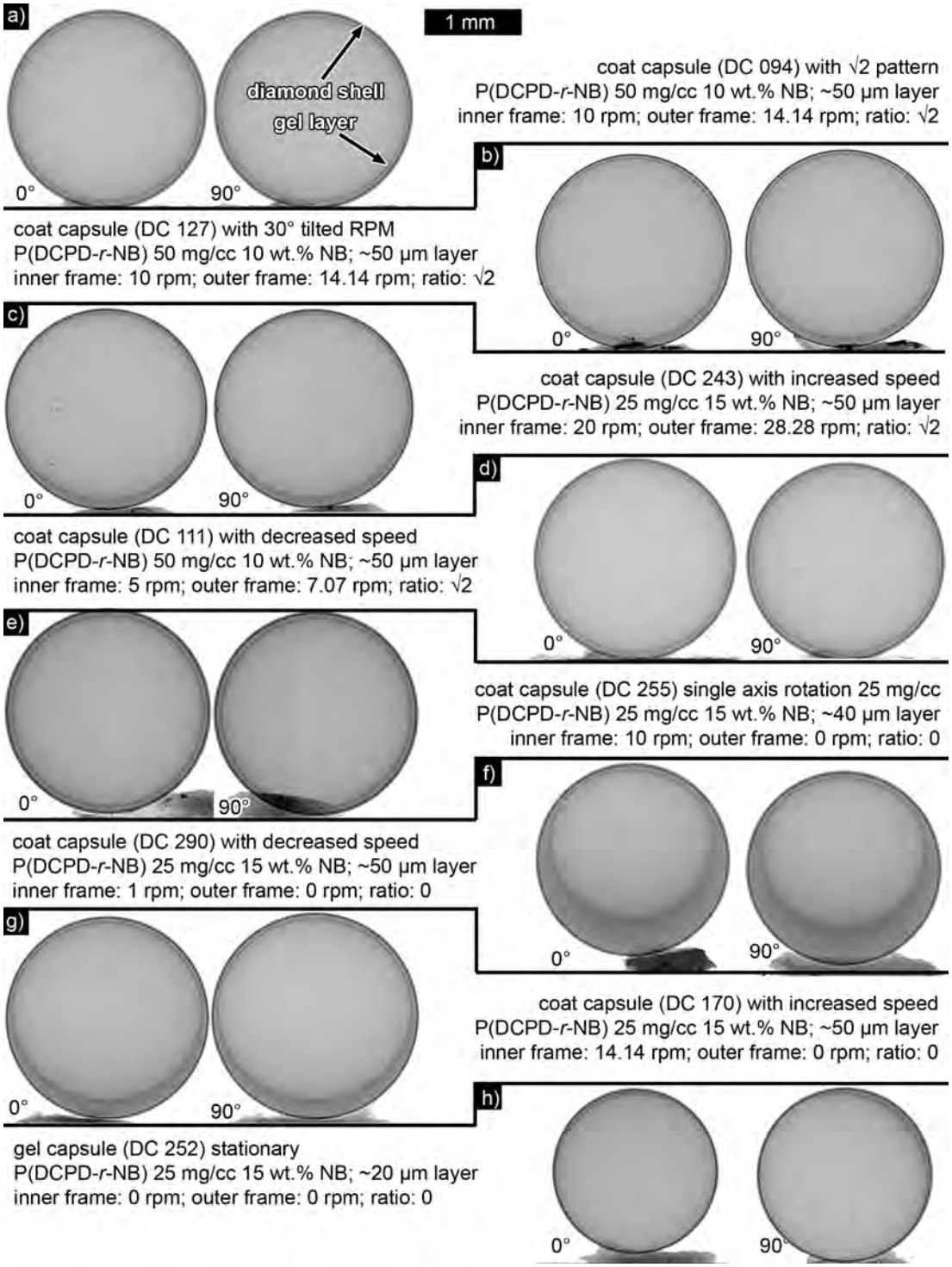

Figure 5.28: Analysis of different coating parameters - the influence of different coating parameters on the resulting wet gel. Some capsules slightly filled up with some liquid while they were stored in acetone or toluene. Because of gravity this liquid is always on the bottom in the radiographs

to a coating that does not meet the mode one specification. In another experiment I increased the single axis speed to 50 rpm and 14.14 rpm. In Fig. 5.28g) the 14.14 rpm case exemplary shows the result for both coatings without any mode one improvements. As reference Fig. 5.28h) shows a capsule where gelation occurred stationary. The wetting of the precursor solution seems to be excellent with the meniscus reaching almost up to the top which confirms the 0 ° wetting angle used for the CFD simulations.

In other experiments I delayed the coating to reach the desired viscosity, constantly adjusted the coating velocity to match the increasing viscosity of the gel, changed the layer thickness or utilized simulation predictions to improve the mode one non-concentricity. Here a list of things that were tried to improve the coating uniformity:

- Rheology

  The variation of the layer thickness between 15 μm and 750 μm.

  The change of the foam density 25, 30, 40 and 50 $\frac{mg}{cm^3}$

  Using SiO_2 with 5 $\frac{mg}{cm^3}$ instead of P(DCPD-r-NB)

  Adding crosslinker which accelerates the gelation

  Adding 5 %, 10 %, 15 % and 20 % NB

- Rotation parameters

  Using 4.5 as ratio instead of $\sqrt{2}$

  Mounting the capsule not in the intercept of the two RPM frames but instead off axis

  Using a tumbling motion by placing the capsule in a rotating vial with tracks

None of these approaches had any visual influence on the small non-concentricity.

To improve the understanding of the mode one non-concentricity the single axis flows is further investigated in a model and in-situ experiments. Figure 5.29a) shows an estimated flow of the precursor solution within the capsule. The liquid gets dragged up on the front side of the capsule while it “equally” flows down on the sides and on the back part. This model suggests that it is essential to accurately level the axis of rotation to ensure the liquid flows equally distributes to both sides of the capsule. The

belts and gears of the RPM allow a leveling of $\pm 0.5°$ which seems to be insufficient. The current mounting of the single axis coater does not allow a better leveling as well. To prove this leveling hypothesis I designed an additional capsule holder in a cylindrical shape which turns on the "hot-dog- steel roller", Fig. 5.29b). This holder is specifically designed to be used during synchrotron experiments to in-situ monitor the gelation in the capsule. The synchrotron beam is parallel to the axis of rotation and a high speed detector which takes pictures up to 100 Hz captures in-situ radiographs. In addition this holder allows to take pictures perpendicular to the axis of rotation as well. The capsule is fixed by two tapered brackets highlighted in red (Fig. 5.29b) and radiograph images can be taken as long as the brackets do not block the beam. First in-situ experiments with silicone oils in capsules are currently performed to verify CFD-simulations. Figure 5.29c) shows a successfully dried capsule coated with the synchrotron setup steel roller. The steel-roller was accurately leveled to the axis of rotation. The capsule has an almost perfect uniform layer with only about 5 μm out of roundness. Currently in-situ gelation experiments at the synchrotron are prepared.

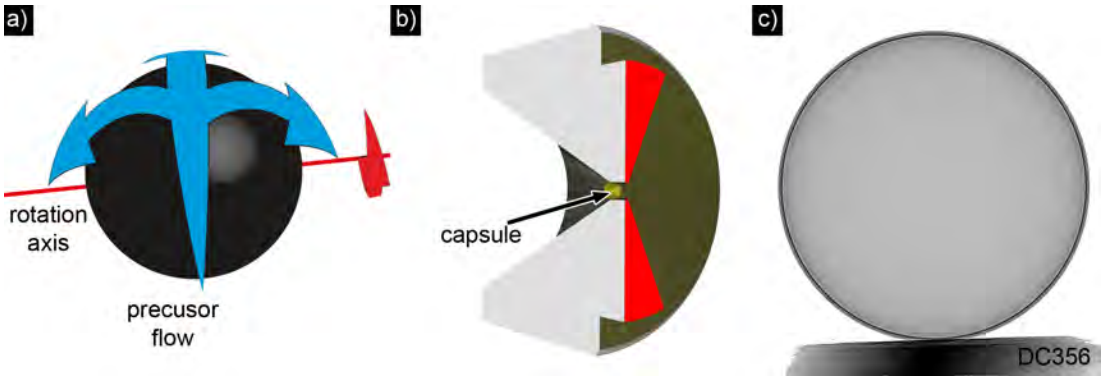

Figure 5.29: 3D single axis coating - a) the schematic flow of liquid getting pulled up on one side of a capsule and distributed to the other three sides in single axis rotation; b) the synchrotron in-situ x-ray radiography capable capsule holder where the capsule gets mounted in two tapered brackets and the beam can capture images parallel and perpendicular to the rotation axis; c) dried capsule with iodine doped P(DCPD-r-NB) aerogel coated with accurately leveled beam time holder on the steel roller

The comparison of the different coating parameters shows that single axis coatings achieve better concentricity than dual axis coatings. A dependency of velocity of the

coating on the layer uniformity was not confirmed even though the analytical approximation is speed dependent. To achieve higher reproducibility the coating process is currently evaluated by in-situ x-ray imaging during gelation.

5.5.2.3.4 Simulation Simulations are a valuable guidance for the coating process since the characterization of the 2 mm capsules is very challenging. Similar to the projection of the simulation in the cylinders a Mercator projection is used for the coating within the capsules. The same projection is used to chart the globe on a map. In addition to the verification of the CFD-code during rotation a stationary gelled simulation of a capsule was compared with a stationary gelled capsule. Figure 5.30a) shows the simulation and Fig. 5.28h) the experiment. The simulation aims for a higher layer thickness but still both images show the strong meniscus effect pulling up the liquid on the sides. A similar good agreement was reached for the 10 and 14.14 dual axis case. The simulation Fig. 5.30b) and the experiment 4.23a)both show a small non-concentricity. The simulation of a single axis case predicts an uniform layer in Fig. 5.30c). This has been achieved in experiments but is not reproducible yet. Moreover the simulation predicts better uniformity if the viscosity increases during the coating process. Currently the simulation is further verified with in-situ experiments of rotating silicone oils in capsules.

5.6 Drying

Capillary forces make aerogels sensitive to the drying process. Because of these capillary forces aerogels are required to be dried by freeze drying or supercritical drying. With these techniques the liquid solvent is transitioned into ice or supercritical fluid that do not have capillary forces anymore. Subsequently the ice is sublimated or the supercritical fluid removed. Here I am using the supercritical drying technique with liquid carbon dioxide (CO_2). For the drying process it is important to use a solvent which is miscible in liquid CO_2. Acetone has a high miscibility while other solvents like toluene require a solvent exchange before drying. However some capsules were successfully dried by skipping the solvent exchange step. The direct drying was not reproducible though.

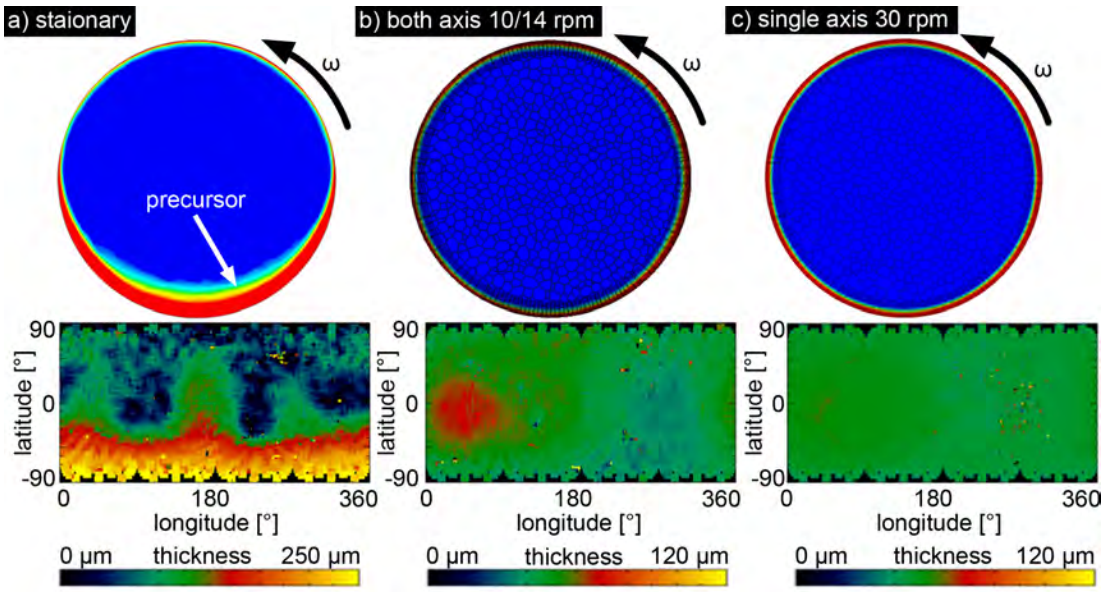

Figure 5.30: Simulation results of 3D coatings - the coating of 0.04 $Pa{\cdot}s$ silicone oil in a capsule after 30 seconds of simulation time, lower images show the Mercator projection of the entire sphere a) the stationary distribution of Fig. 5.28h) is confirmed and the wetting angle is almost 0°; b) the two axis coating case shows the non-concentric gel layer; c) the single axis case at 30 rpm shows an uniform layer which does not agree with the experiments

5.6.1 Experimental

5.6.1.1 Solvent exchange

The solvent exchange for bulk samples is relatively simple by placing the bulk gel into a stirred acetone bath. Over time the acetone diffuses into the bulk gel and exchanges the solvent. In a capsule the small fill hole of about 30 μm limits the diffusion which can be even further reduced by a plug of air-dried gel in the fill hole. To accelerate the solvent exchange I developed a pressure cycling setup that drives acetone in the capsule. Figure 5.31a) shows the schematic pressure cycling setup. The pressure chamber is pressurized with an inert gas like helium and the liquid surrounding the capsule is forced into the capsule. A pressure gauge monitors the process while two computer controlled valves regulate the pressure. Figure 5.31b) shows the corresponding LabView control program. The program is used to manually run the valves or to run programmed cycles. For the programmed cycles the wait time before start, the peak pressure, the time frame at peak pressure, the time frame at environmental pressure and the amount of cycles need to be set. The ramp speed meaning the slope of the pressure increase needs to be set for both modes. The small insert shows an exemplary recorded pressure cycle. The actual setup is shown in Fig. 5.31c) with the pressure regulator reducing the bottle pressure to 120 psi and passing the gas through stainless tubing into the pressure cycling setup. The first computer controlled omega FSV11 valve controls the gas input while the pressure is measured by an Omega PX409-150GV pressure transducer which was calibrated with a Swagelok PGU-50-P160 gauge. The pressure chamber consists of a chemglass CG-1880-04 heavy wall pressure vessel, a pressure relief device set at 150 psi and a second containment out of polycarbonate. The vent is controlled by an omega FSV11 which exhausts the gas into a fume hood. Valves and the pressure controller are connected through a National Instruments CompactDAQ controller with an analog out- and input.

5.6.1.2 Infrared spectroscopy

Infrared spectroscopy was used to identify the amount of solvent exchange which probes the efficiency of the solvent exchange procedure. The infrared radiation excites the characteristic vibrational frequencies of molecules which depend on the weight of the atoms and the strength of the bonds between atoms. If infrared radiation with the

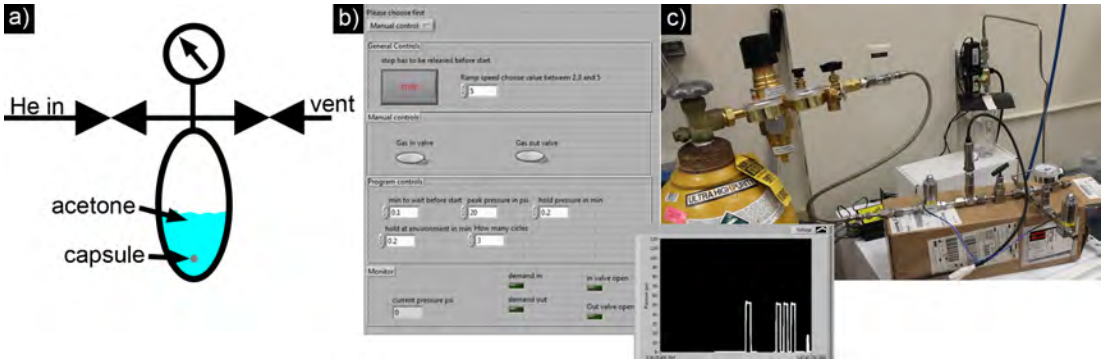

Figure 5.31: Pressure cycling setup - a) shows the schematic pressure cycling setup where the pressure within the pressure vessel is controlled by two valves; b) the lab view interface to control the pressure setup with an exemplary pressure curve on the lower right; c) the actual setup build with VCR fittings and tubing

right frequency is applied the molecule absorbs this radiation. Each molecule has a distinctive frequency absorption which consequently can be used to identify the solvent by this technique.

Here I am using a Fourier-transform-infrared-spectroscopy (FTIR) which probes all frequencies at once by using an interferometer. Figure 5.32a) shows schematically how the interferometer is designed to generate all frequencies. The coherent light beam first goes through a beam splitter to one stationary mirror and one retardation mirror. The retardation mirror moves back and forth to delay the light. The reflected light is combined in the beam splitter and the interference of the initial and delayed light generates all frequencies. The recombined beam probes the sample and a detector collects the incoming light. The detector sample gets decoded with a Fourier transformation leading to an absorption spectrum.

To measure the solvent within the capsules I am using a Perkin Elmer Spektrum 2000 instrument with MIRTGS-detector. Figure 5.32b) shows the setup of a gas cell with potassium bromide (KBr) windows which is used to measure the solvent in the capsules. Initially the gas cell is purged with nitrogen. The capsule is placed into the gas tight syringe which is connected to the gas cell. After I crushed the capsule I pulled nitrogen from the gas cell into the syringe and waited about 10 min for the vapor pressure to equilibrate. Then I injected the nitrogen solvent mixture into the

gas cell, closed the valves of the gas cell and removed the syringe. The sample holder containment of the instrument was purged for another 10 min with nitrogen before I started the measurement of the spectrum with the "Spectrum" software from Perkin Elmer.

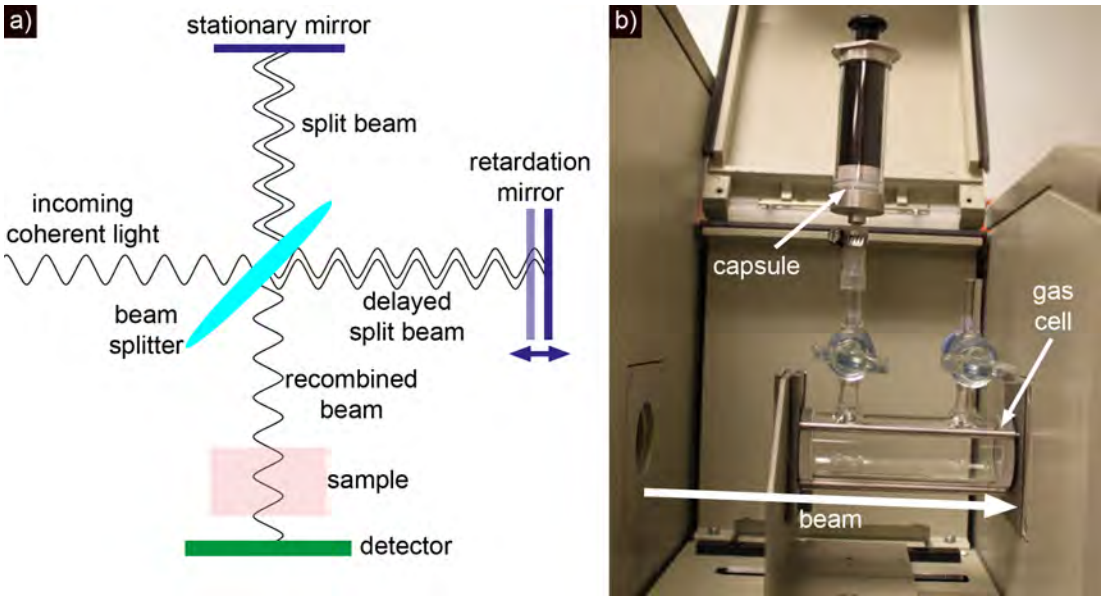

Figure 5.32: FTIR - a) the schematic setup of a FTIR interferometer where the interference is generated by a retardation mirror; b) the actual setup used where the capsule which contained the sample to be analyzed is crushed in a syringe and the vapor injected into the gas cell

5.6.1.3 Supercritical drying

To avoid capillary forces that would crash the aerogel in the drying process a supercritical fluid is used. In a supercritical fluid a distinct gas and liquid phase does not exist anymore and it has a relative high density compared to gas. Figure 5.33a) shows the phase diagram of CO_2 which is used for the drying here. Before starting the three step drying process the pressure vessel usually gets completely filled with acetone. In the first step the pressure vessel is chilled below room temperature to fill the chamber with liquid CO_2. One vent valve is slightly opened to purge the acetone out of the system. After the acetone is completely exchanged with liquid CO_2 the samples are kept at this condition between 1-7 days to exchange the solvent with CO_2. In the second step all

valves are closed while the temperature slowly increases to 50 °C. With the temperature ($T_{crit} = 31$) the pressure ($p_{crit} = 74bar$) increases and the CO_2 reaches its supercritical regime. The system needs to be supervised in this step to ensure the pressure does not increase above the relief device set at 1800 psi. In the final step the system is slowly vented until the chamber reaches environmental pressure and the dried samples can be removed. I used a Polaron E3100 critical point drier from Electron Microscopy Science which is shown in Fig. 5.33b). It has one valve for the liquid CO_2, two vent valves, one window to observe the inside of the chamber, one thermometer and one pressure gauge. The polaron is directly connected to a siphon tube CO_2-cylinder.

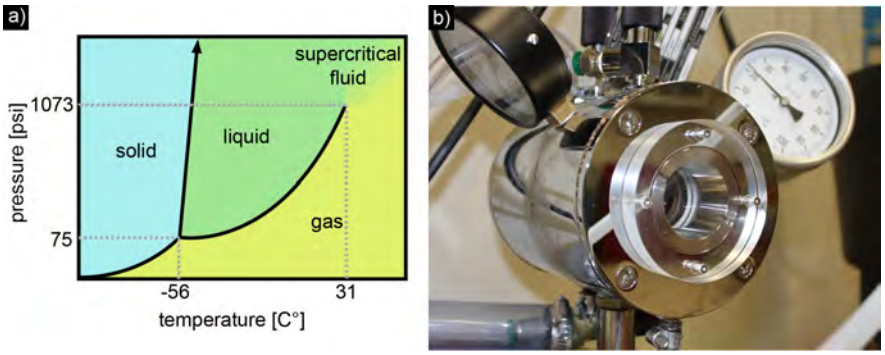

Figure 5.33: Supercritical drying - a) shows the phase diagram of CO_2. To dry the aerogel samples the polaron pressure vessel (b) gets filled with liquid CO_2 and by raising the temperature in the closed pressure vessel the pressure increases and reaches the supercritical regime. Capillary forces in the aerogel do not occur in a supercritical fluid. By opening a valve the supercritical fluid is released leaving the dry aerogel behind

5.6.2 Results and Discussion

The dependence of NB on the drying behavior and shrinkage is shown in Fig. 5.34. The transparency of the wet gel increases with increasing NB concentration in the 50 $\frac{mg}{cm^3}$ P(DCPD-r-NB) gel, Fig. 5.34a). Generally polymeric gels become clear when the particle or pore size becomes very small. Viscous polymer solutions are also clear. Preliminary small angle x-ray scattering spectroscopy and transmission electron microscopy indicated that the pore size in the P(DCPD-r-NB) decreases with increasing NB concentration. The small pore size makes the aerogel difficult to dry because of the slower solvent exchange caused by narrow pores. Figure 5.34b) exemplary shows that P(DCDP-r-NB) gels shrink during supercritical drying if the NB concentration

exceeds a certain threshold. By using hexane as intermediate solvent with a better miscibility in toluene the shrinkage was limited to a minimum in Fig. 5.34c). This successful drying is consistent with the hypothesis that the transparency is due to the small pore size. The toluene was exchanged with hexane for about 7 days, followed by an acetone exchange and final drying in liquid CO_2. The gels shown in Fig. 5.34c) were prepared with all the same amount of precursor while for the 2 step-drying the precursor amount increased with the NB concentration. The formulation with 10 wt.% NB as additive was selected for most of the coating experiments since it only shows limited shrinkage even in the 2-step drying process and it has the desired rheological properties.

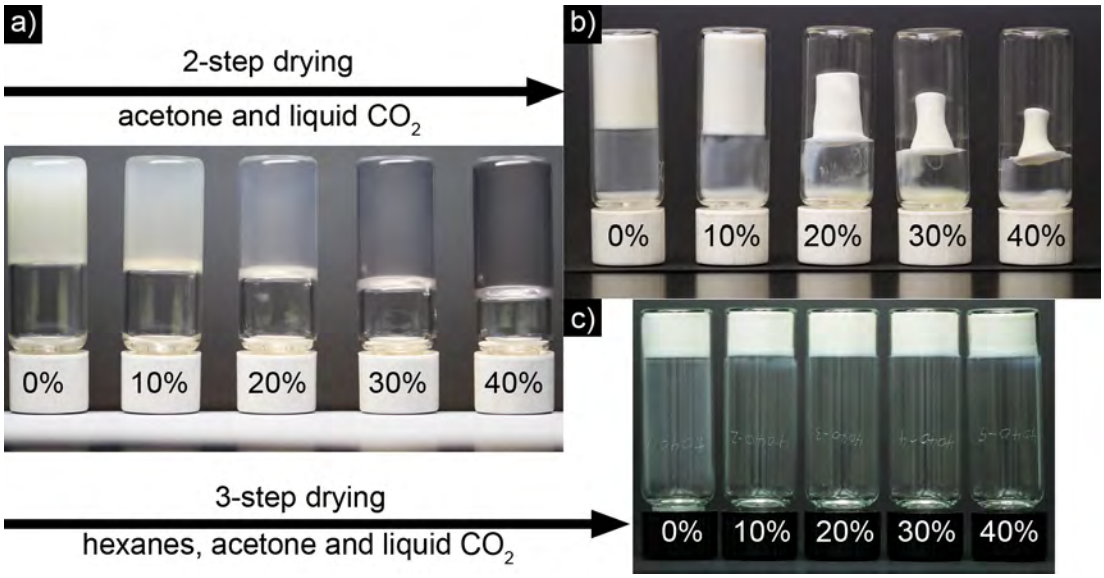

Figure 5.34: mitigating the shrinkage during drying - a) shows different P(DCPD-r-NB) wet gels where the transparency increases with increasing NB content. b) some shrinkage in the high NB concentrations occurs if the toluene is only exchanged with acetone; c) by exchanging with hexane before exchanging with acetone shrinkage can be avoided

The pressure cycling process is strongly dependent on the solvent which gets into the capsule. I compared eight capsules with 30 μm fill holes that were coated with a 50 μm layer of 25 $\frac{mg}{cm^3}$, 15 wt.% NB P(DCPD-r-NB) to measure the weight gain through solvent, the efficiency of the solvent exchange, the difference between multiple cycles and the influence of the fill hole orientation. The fill hole orientation and the amount

of cycles make no difference on the amount of liquid which gets into the capsule. To control the fill hole position the PTFE capsule holder was used. Capsules after one cycle at 105 psi for 120 min with the hole pointing up during the cycling gained about 3.2 mg of weight which is the same value capsules gained with the hole pointing down. A small air bubble was observed within the capsules which disappeared after storing the capsule for 7 days in acetone. Capsules which went through a two cycle process with 24 hours between the cycles immediately showed complete fill.

To control the efficiency of the pressure cycled capsules the FTIR spectra of the exchanged capsules and different toluene-acetone mixtures are compared. As reference standards I injected 3.5 μL of acetone and toluene in the ratio of: 100:0; 98:2; 95:5 and 0:100 directly into the gas cell. The 3.5 μL comply with the actual total capsule volume of 4.2 μL after compensating for remainders lost by the syringe injection method. For the low volumes and concentration used here the FTIR spectra barely show any distinctive absorption except of one toluene out-of-plane C-H bending at 735 cm^{-1}. This characteristic peak is shown in Fig. 5.35. The pure acetone spectrum in pink does not show any absorption around 735 cm^{-1} while toluene in black shows an obvious peak. The insert shows the references in comparison with two pressure cycled capsules. DC 331 underwent two cycles each 120 min at 105 psi and was measured 24 hours after the pressure cycling was finished. The FTIR result shows that this capsule contains a solvent mixture that has between 2 % and 5 % toluene. If only acetone would be filled in the capsule without having any diffusion or solvent exchange the concentration would be 14 %. DC 322 was pressure cycled once at 105 psi for 120 min and afterwards stored in acetone for 7 days. The FTIR spectrum indicates that the toluene was completely exchanged by acetone. In summary this means that diffusion is efficient enough after the capsule got filled by pressure cycling. The idea that a capsule with the fill hole pointing down has a contracting air bubble under pressure which contracts and expands with every cycle to pump acetone in and out disagrees with the experiment. However the complete fill has the advantage that a completely filled capsule is less sensitive to the pressure burst with liquid CO_2 since the filled capsule is incompressible.

After the chemistry in a capsule process was completed a representative capsule with a dried 50 $\frac{mg}{cm^3}$, 15 wt.% NB P(DCPD-r-NB) is shown in Fig. 5.36. This capsule was

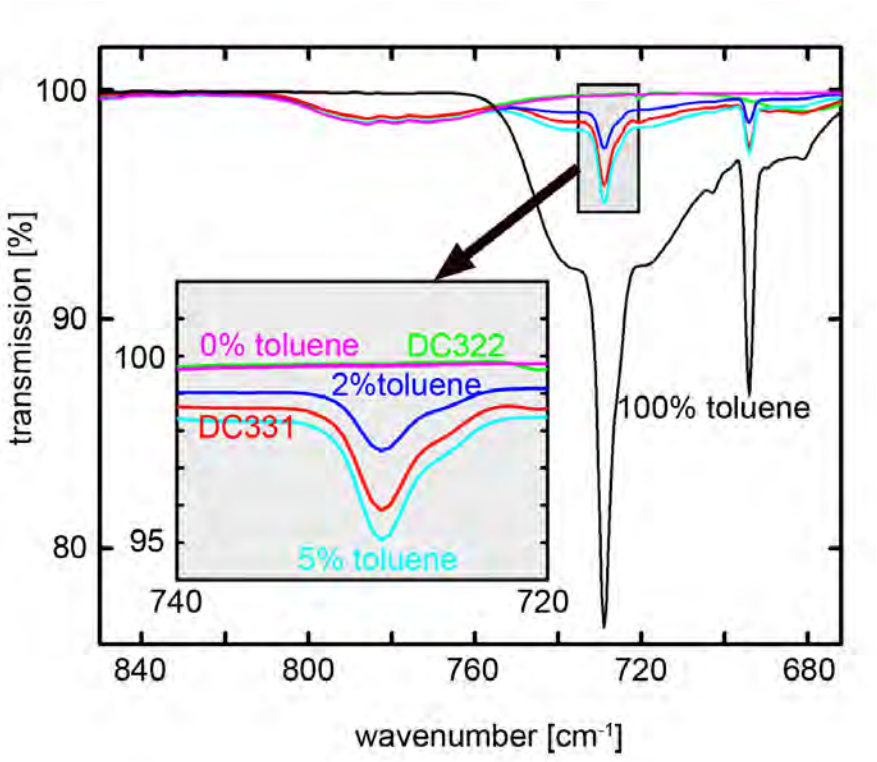

Figure 5.35: Amount of solvent exchanged characerized by FTIR - the best solvent exchange is reached for the diamond capsule 322 which was pressure cycled once and then diffusion for 7 days exchanged the remaining toluene. DC331 was pressure cycled twice but immediately measured after that so additional diffusion did not occur. Various toluene and acetone mixtures are shown as reference

doped by liquid iodine doping prior to the supercritical drying. The doping is required to increase the visibility of the foam during non-destructive x-ray imaging. The doped foam layer is clearly visible around the circumference. In the 0° view (Fig. 5.36a) the layer is slightly thinner at the upper right than the 90° view (Fig. 5.36b) while the lower right is a bit thinner. This is the non-uniformity of the wet gel. Figure 5.36c) shows the tomography of a free standing pure PDCPD film that was coated within a diamond capsule. The diamond shell has been removed during computer tomography image reconstruction. This disrupted gel layer agrees well the disrupted wet gel in Fig. 5.18c).

Figure 5.36: Capsules with a dried foam layer - a-b) show diamond capsule 94 after drying and doping with iodine. The layer is almost uniform. c) the free standing film with the diamond capsule removed shows a band with less coating. This coating was pure PDCPD without the addition of NB

5.7 Foam characterization

5.7.1 Experimental

The morphology of the dried aerogel samples was investigated with a Jeol JSM-74011f scanning electron microscope (SEM) which is equipped with energy-dispersive X-ray (EDX) elemental composition analysis capability (Oxford Instruments, Oxford INCA 350). Both techniques are usually combined in one instrument where electrons are accelerated with 2-3 kV onto the sample. For the images here the secondary electrons which are released by the interaction with the primary electrons are detected by the SEM and converted into an image. The x-rays measured by EDX are created by elec-

trons jumping in electron holes (electronic relaxation) that are caused by the primary excitation of electrons. The electrons which fill the electron holes are from an outer, higher-energy shell release energy by x-rays, among others. This released energy of the x-rays is distinctive for each element and can be used for characterization. Elastic Recoil Detection Analysis (ERDA) and Rutherford Backscattering (RBS) were performed with a 4 MV ion accelerator module 4UH by NEC that was done with 3.0 MeV $^4He+$ ions.

5.7.2 Results and discussion

The effect of the NB addition on supercritical dried 50 $\frac{mg}{cm^3}$ P(DCPD-r-NB) aerogels on the morphology is shown in Fig. 5.37a-c). P(DCPD-r-NB) gel shows a branched fibrous structure where pure PDCPD aerogel in Fig. 5.37a) is slightly coarser than aerogel with 10 wt.% NB in Fig. 5.37b) which is consistent with the increasing transparency of the wet gel with increasing NB addition. The void structure and the entangling of the branches are not significantly different. An effect of rotation on the morphology was not observed since the stationary gel in Fig. 5.37b) and the rotated gel in Fig. 5.37c) look very similar. The SEMs of the rotated dried SiO_2-, TiO_2- and Fe_2O_3-aerogel also look identical compared to stationary gels with the same composition. All images were acquired of the topview of the gel, not the cross section. SiO_2-aerogel has the characteristic small chain or pearls network in Fig. 5.37d), TiO_2-aerogel has a cauliflower like structure with some gaps in between and the Fe_2O_3-aerogel looks a bit similar to solidified lava. The elemental analysis of the P(DCPD-r-NB) foams within the capsules revealed a composition of 85-95 at.% carbon, 5-15 % oxygen, about 0.5 at.% iodine for the doped capsules and a small residual of aluminum. The high oxygen concentration is due to the storage of the dried aerogels in air. The characterization of P(DCPD-r-NB) directly after extraction revealed an oxygen concentration of about 1 at.%.

5.8 Conclusion

In summary, I demonstrated that the walls of rotating cylinders and deterministically rotated spheres can be coated with uniform aerogel layers. First I explained how

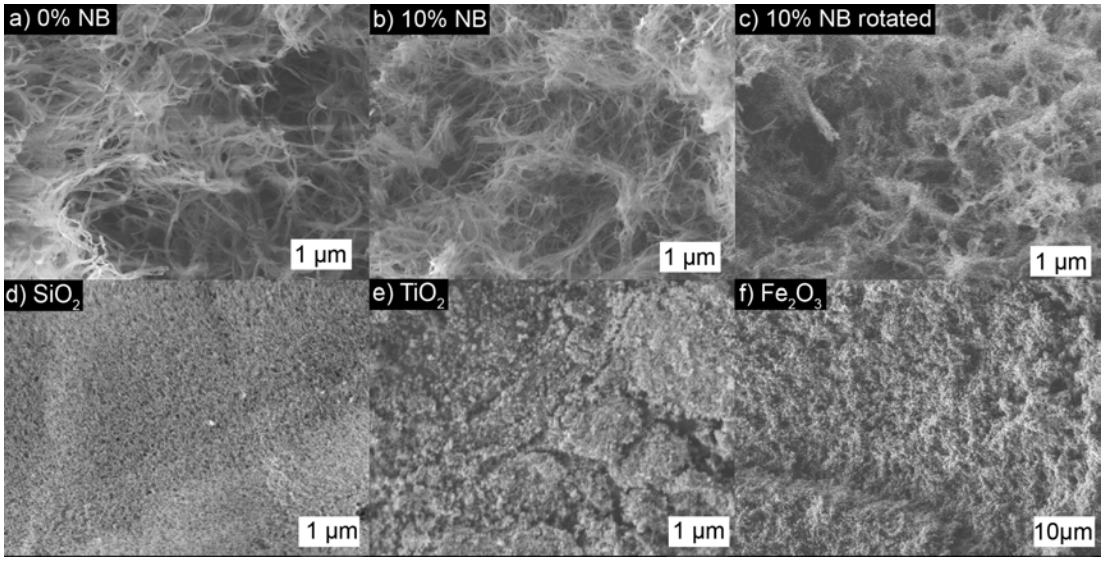

Figure 5.37: SEM images of the dried aerogels - a-c) the SEM images of P(DCDP-r-NB) show a smaller feature size with increasing NB concentration; d-f) SEM images of the aerogel layers coated in Fig. 5.23 which do not show any differences to stationary aerogels (not shown)

through a co-polymerization approach the viscosity of P(DCDP-r-NB) can be manipulated which can be used to decreases the shear forces experienced by the rotating liquid. In the second step I used the guidance of Melos Equation 5.9 and CFD simulation results to predict the coating of aerogels inside a horizontally rotating cylinder. Succesfull coatings were achieved for SiO_2, Fe_2O_3, TiO_2 and $P(DCPD-r-NB)$ aerogels where the liquid was transitioned abruptly into the rimming state region. With the knowledge of the pre-polymerization and the coating prediction I started to coat spherical diamond shells. These shells were first mounted in a PTFE capsule holder where a tapered hole clamped the capsule with its fill hole pointing upwards. In this holder the capsule was filled with nL precision by a custom build pressure differential filling device. Then the fill hole was temporary plugged by surrounding precursor solution which was contained by a pipette tip mounted on the capsule holder. Now the capsule with its holder was placed in a custom build positioning machine which constantly changes the gravity vector relative to the capsule. Different coating patterns, speeds, layer thicknesses and chemical compositions were tried to achieve a uniform coating within the spherical shell. In the final step the solvent of the aerogel is removed by supercritical

drying. For bulk aerogels a solvent exchange of the toluene in the P(DCPD-*r*-NB) with acetone led to negligible shrinkage during drying. To facilitate this solvent exchange an intermediate step before the supercritical drying was applied for some capsules where the capsule was pressure cycled in a custom build device.

The success of the coating process was tracked by a wiki-database. Unfortunately most capsules had a non-concentricity. The occurrence of this non-concentricity could not be clearly identified. In-situ synchrotron experiments were performed to understand the liquid flow within the capsules and thus the possible reason for the non-concentricity. The first results with silicone oil in the capsules are currently under review and in-situ experiments with precursor solution will follow in the future.

6

Catalytic coatings inside steel tubing

The chapter about catalytic coatings inside stainless steel 316 tubing is the cylindrical coating extension of chemistry in a capsule chapter 5. Coatings are applied inside steel tubing because of its robustness as well as negligible mass and heat transfer resistances which enable an excellent efficiency for catalytic processes. Especially the mechanical stability, morphology, rheology and thermal stability of aluminium-iron-oxide coatings that are promising catalysts for Fischer-Tropsch synthesis are characterized here.

6.1 Experimental

6.1.1 Pretreatment of steel tubing

Swagelok stainless steel 316 (17 % chromium, 12 % nickel, 2 % molybdenum) with 12 mm outer diameter and 9 mm inner diameter were cut in 2 cm pieces. On the inner edges of the tubes 45° chamfers were fabricated to facilitate mounting of rubber plugs for the coating. As chemical pretreatment the tubing pieces were first etched for 10 min in a mixture of sulfuric acid and water (1:1, 2:1, 1:2). If not mentioned differently a 1:1 mixture was used and the samples were sonicated after etching for 10 min in deionized water. After etching most samples were treated at 800 °C for 1 hour with the following temperature profile: 2 hours heating to 100 °C, 3 hours heating to 800 °C, holding the temperature for 1 hour and slowly cooling down to room temperature

for about 12 hours.

The morphology of the samples was characterized with a Zeiss Supra 40 SEM and a Keyence V-9710-K Laser microscope.

6.1.2 Aluminium-Iron-Oxide sol-gel

Two different sol-gel approaches were mainly used to fulfill the coating requirements. An epoxide addition method which is very similar to the iron oxide gel in chapter 5.1.1.3 was tested with an iron- and aluminium nitrate. The ratio between iron and aluminium was 2:1 where 1.45 g iron(III) nitrate nonahydrate (Sigma-Aldrich, ACS reagent, $Fe(NO_3)_3 \bullet 9H_2O$), 0.67 g aluminum nitrate nonahydrate (Riedel de Haën, ACS reagent, $Al(NO_3)_3 \bullet 9H_2O$) and 0.1 g polyethylene oxide (alfa aesar, M.W. 1,000,000) were dissolved in 13mL ethanol (VWR chemicals, ethanol NORMAPUR) and 0,65 g deionized water. After the polymer dissolved in the solution 3,31 g chilled propylene oxide (Acros Organics, 99.5 %) were added to the solution to start the sol-gel formation.

The shear-thinning aluminium-iron-oxide sol-gel is based on Germani's approach for platinum/ceria/alumina gels which was modified to incorporate iron.(31) About 17 g Aluminum-tri-sec-butoxide (Sigma-Aldrich, 97 %, ASB) are dissolved in about 50 mL deionized water (17 g ASB contain 1.86 g Al which results from multiplication of 17 g and $\frac{M(Al)}{M(ASB)} = 0.11$). The water is first stirred and heated at 80 °C and the ASB is slowly added, followed by 1 molar nitric acid solution until PH 2.5-3 is reached. The temperature is then lowered to 60 °C while the solution gets stirred for about 12 hours with a reflux condenser (w/o coolant) connected. The iron oxide content gets added by weight percent where the Al content gets multiplied by the desired iron oxide concentration and divided by the ratio of atomic mass of $\frac{M(Fe)}{M(Fe(NO_3)_3)} = 0.138$. For the 20 % iron content sol gel mainly used here this means $\frac{1.86 \cdot 0.2}{0.138} = 2.7 gASB$ which gets dissolved in about 15 mL deionized water. The amount of water is an empirical value for each iron concentration and influences the time to the sol-gel transition. In the last step the ASB solution and the iron oxide solution get mixed at 80 °C and stirred for 30 min. Within one day the solution transitions in a gel which turns back to a sol after

shaking the gel.

6.1.3 Rheology and coating

In contrast to the gels in chapter 5 where the gelation was irreversible over time the characterization of a shear thinning gel is different. The gel gets less viscous with increasing shear rate and by decreasing the shear rate the gel-network builds up again. Shear thinning gels are convenient for coatings as long as the shear forces of the rotation do not harm the viscosity increase. The distribution of the shear thinning gel is done by shaking which temporary harms the gel network. The coating is now similar to the gels characterized before because of the following increase in viscosity. A shear-rate scan was performed with a shear rate between 0 and 250 $\frac{1}{s}$ with two cycles on a CVO 100 instrument by Bohlin Industries and the appendent software. As setup geometry a cone and plate setup with a $50\mu m$ gap was used which gave sufficient torque for the transducer to get a reliable result.

For the coating of the steel tubes with the epoxide addition method the tubes were plugged with a rubber ring between two washers and by tightening the screw in the center the rubber got compressed and sealed the tube. The tube was sealed on one side first then filled with about $200\mu L$ and sealed on the opposite side. To coat the tubes with the shear-thinning gel rubber plugs with a conical outer diameter of about 9-9.5 mm and an inner hole with 4 mm were mounted. About $200\mu L$ of precursor solution were filled through the 4 mm holes of the plugs. To pipette the sol in the tube it was sufficient to shake the container before use. This resulted in a layer of about $400\mu m$ thickness and shaking the filled tube uniformly distribute the sol in the tube.

The filled tubes were then placed on the roller as shown in Fig. 5.11b) at room temperature and rotated with speeds between 12 and 60 rpm. If not mentioned differently the speed was 12 rpm. The resulting layer was then either dried in air during rotation, in air after solvent exchanged in a vial (acetone, ethanol or t-butanol) or supercritically dried after solvent exchange in acetone (VWR chemicals, Acetone NORMAPUR). As supercritical drier a Bal-TEC CPD 030 device was used and the sample was placed in 25mL acetone in the beginning. The remainder of the chamber got filled with liquid

carbon dioxide and the acetone was purged out for about 6 hours. The sample was kept in liquid carbon dioxide for 72 hours and then the carbon dioxide was transitioned in the supercritical regime and vented as described in chapter 5.6.1.3.

6.1.4 Calcination

The coated tubes were calcined after drying at 400 °C in a furnace. To remove remaining liquid in the gel layer the samples were first heated to 100 °C within an hour and the temperature stayed there for another 3 hours. In the next 3 hours the temperature increased to 400 °C where the specimen was kept for another 3 hours. After this process the furnace slowly cooled down to room temperature in about 12 hours and the samples were removed.

6.1.5 Mechanical stability

The mechanical stability and especially the adhesion were tested by tapping the tube on a stone plate and by sonication. To measure the loss during the process the tubes were weighed after each step. In the first step the samples were knocked 5 times very light on the plate and rougher in the second step (5 times). The ultrasound test was started at 30 % power at a frequency of 80 kHz for 5 min. The samples were plugged in the same way as the tubes during the epoxide addition method coating above to ensure that the coated layer stays dry. In the final step the power was increased to 100 % for 5 min. Similar adhesion tests were performed before by Avila and in references therein.(5)

6.2 Results and discussion

6.2.1 Tubing pre-treatment

The treatment of the metal tube surface is important to control the morphology and elemental composition which influences the adhesion between surface and coating. Figure 6.1 a) shows an untreated tube of stainlesss steel 316 on the left as reference. A magnification of the outer tube surface is recorded by laser microscope (b (left) where groves

are visible. Further magnification shows the SEM image (right) with a smoother surface and rare craters between the grooves. The acid treatment c) changes the morphology to many small pitting corrosion craters as the SEM and laser microscopy images show. Different acid concentration 22 % and 66 % were used for etching as well but had no visible influence on the surface morphology (not shown). Additional heat treatment at 800 °C after the acid treatment grows small crystalls on the surface d). The root-mean-square roughness measurement by the laser microscope of the three tubes was similar between $0.2 - 1\mu m$ for all tubes.

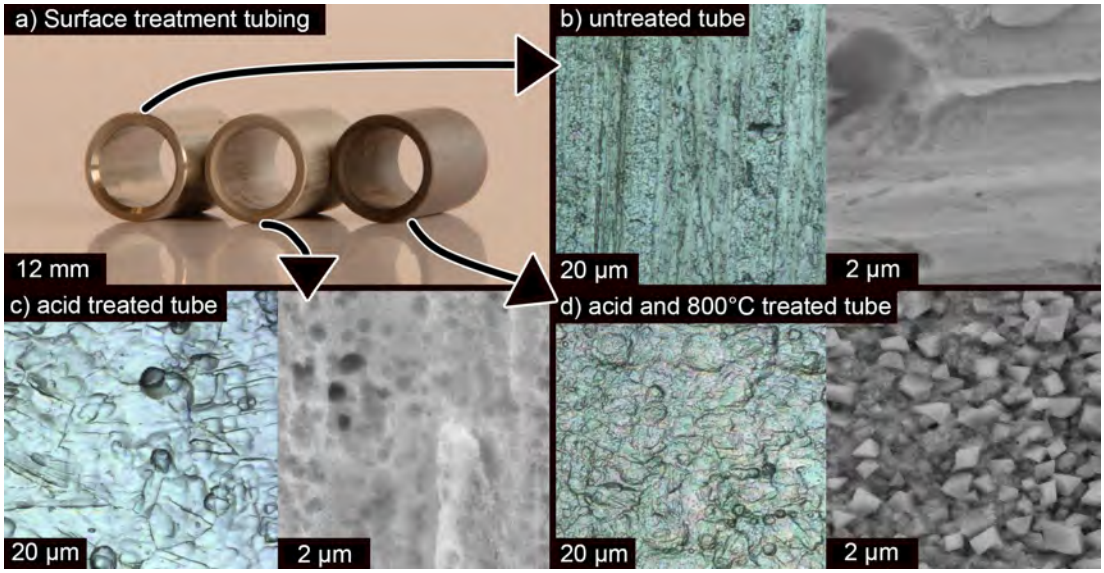

Figure 6.1: Tubing pre-treatment - a) shows the treatment with chemical etching (center tube) and additional heating (right tube). As reference and untreated tube is shown on the left. b-d) show Laser-Scanning-Microscope images and SEM images of the surface of these tubes. b) shows some grooves in axial direction. c) shows some craters created by the etching with 50 % sulfuric acid. d) in addition to the creators some crystals grew on the surface

Earlier investigations of the heating of stainless steel already observed the formation of carbides, mainly chromium carbide, on the surface.(39, 58, 110) These carbide crystals on the surface are known to either enhance the adhesion or to cause delamination depending whether the film was deposited before the carbide formation or after.(39) For an untreated tube with a sol-gel film this means that during calcination the carbides can form and cause cracks. By heating the tubes before the coating the formed carbide

crystals are used as anchors for the sol-gel and improve the adhesion of the layer. Here, the use of an fine grained boehmite primer as suggested by Zhao, Rao Peela and Jia did not yield to a better adherence for the sol gel layer.(50, 81, 116)

6.2.2 Coating feasibility

Thermal expansion mismatch between the coated layer and the surface as well as rigid layers that cannot compensate for thermal mismatch and gel shrinkage are the main reasons for gel delamination and cracks. Moreover it is important to use a sol-gel system that forms gel in a reasonable time. Preliminary experiments showed that the ethylene glycol sol-gel by Takahashi and iron oxide in water/ammonia by Orel did not form any gels within 72 hours and were not further tested.(77, 101) The gel time of expoxide addition gel was easily tunable by changing the water concentration and gelation for the shear thinning gel occurred quick in a cold environment or by evaporating the solvent.

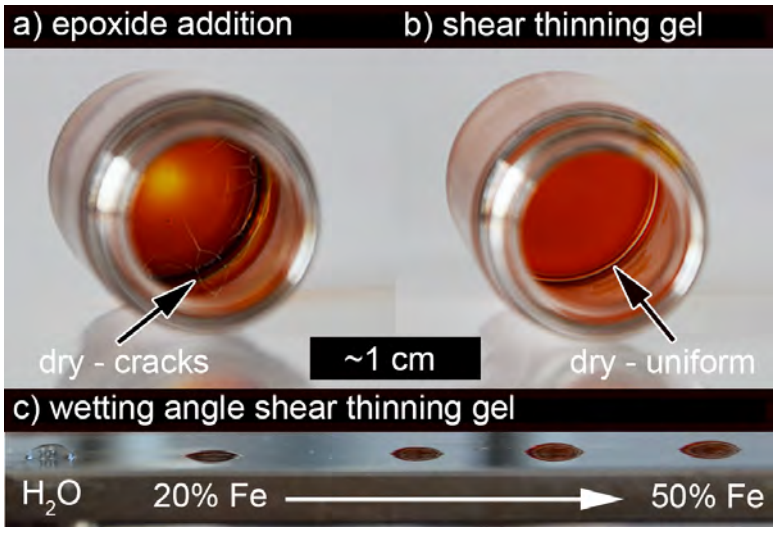

Figure 6.2: Crackability of gels - a) the epoxide addition gel shows some cracks after drying under ambient conditions and the gel layer is thinner in the center of the vial; b) by contrast, the shear thinning gel is uniform on the entire vial button; c) the wetting angle of shear thinning gels with different Fe/Al ratios on stainless steel shows better wetting for the low iron content that has less water and more ASB

The xerogel was formed by drying the wet gel layers at ambient conditions (room

temperature). The epoxide addition sol-gel showed a lot of inhomogeneous shrinkage which is shown by the thinner layer in center of the vial in Fig. 6.2 a). In addition the thicker parts showed cracks as the arrow indicates. The shear thinning gel in b) shows a perfect uniform layer without any hints of delamination. The same behavior occurred on steel surfaces. Because of the crack formation I decided to focus on the shear thinning sol-gel which has superior drying characteristics. The wetting angle of the shear thinning gel wets stainless steel better than water and the lower the iron content the better the wetting, Fig. 6.2. This makes this gel promising for coatings since in tubes under rotation it is important that the sol uniformly wets the surface.

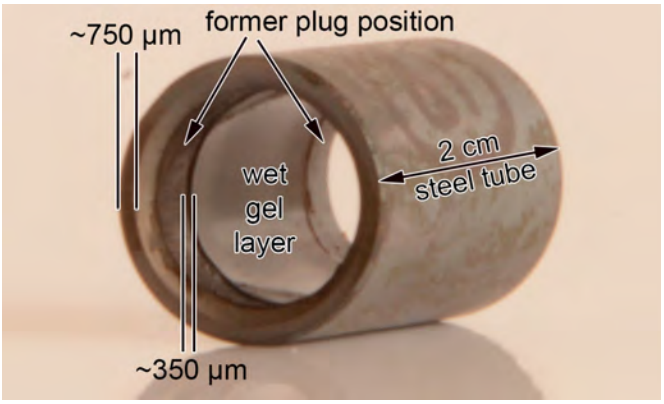

Figure 6.3: Shear thinning gel in steel tube - after coating the tube with the shear thinning gel for about 12 hours the gel layer shrinks and gets stabilized by the evaporation through the holes in the plugs

To achieve robust coatings in a reasonable time frame with the shear thinning gel the solvent of the sol-gel partly evaporates during the coating because of holes in the plugs. Figure 6.3 shows this condensed layer after 12 hours. The wet gel was restricted by the plug on each side and is about $350\mu m$ thick which is roughly about $50\mu m$ less than the initial filled volume. To accurately control the thickness of the resulting wet layer the venting and humidity of the ambient air needs to be controlled which was only partly the case in the lab room. As reference for the thickness measurement I used the chamfered edge of the steel tube. Preliminary experiments for 4 mm inner diameter Swagelok tubes showed that the coating works in smaller diameters as well. The filling of these small tubes is more challenging since bubbles which fill the entire tube must be

avoided. In addition first experiments with higher iron concentrations up to 40 % and cobalt instead of iron yielded to uniform, well adhered coatings as well. Both metals, iron and cobalt, as sol-gel with aluminium as structural promoter were already proven to work for Fischer-Tropsch synthesis.(67)

6.2.3 Rheology shear thinning gel

The advantage of the shear thinning gel is that the viscosity can be reversibly lowered. By shaking the gel in the beginning it is very easy to wet the entire surface and with time the viscosity increases again to form a gel. Figure 6.4 clearly shows this behavior where an increasing shear rate in the first cycle dramatically lowers the viscosity and by decreasing the shear rate the viscosity increases again. At low shear rates the second cycle does not match the first cycle since the sol had not enough time to form the entire gel network again. At higher shear rates the first and second cycle match again. The shear rate in rotating tube is so low that shear thinning behavior in the tube is mitigated. Consequently the viscosity only increases after shaking the filled tube and placing it on the roller. With the increasing viscosity the shear forces disappear since at high viscosities the gel moves with the rotating tube. Shear forces of the rotation were not enough to lower the viscosity. The holes in the plugs allow the evaporation of the solvent of the sol which increases the particle fraction in the sol and thus the viscosity. This effect even allowed uniform coatings at 60 rpm because of the disappearing shear forces for a viscous sol under rotation. This behavior and Melo's equation 5.9 which predicts 35 rpm for a 400 μm thick layer (gets thinner with evaporation) at 0.2 Pas (probably higher with evaporation and time) indicate that it might be feasible to coat even thicker layers.

6.2.4 Layer characterization

Sol gel coatings have the advantage that very high surface to volume ratios can be reached and thus a large catalytic surface is built. Various drying techniques were used to generate this high surface area with a porous network. Initially SEM images of air dried xerogels only showed an about $3\mu m$ thick coating with a dense surface (the initial precursor volume was for a $400\mu m$ layer and the coated wet layer in ambient

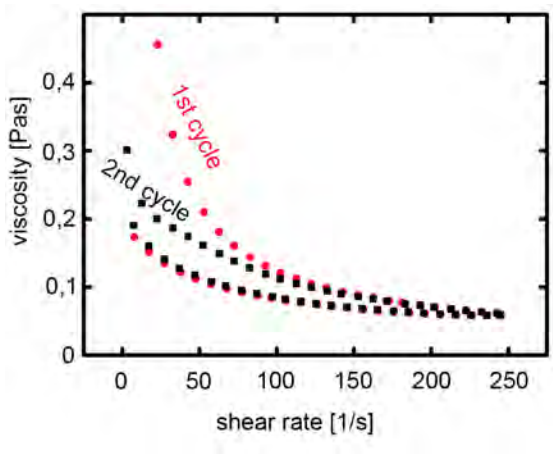

Figure 6.4: Rheology shear thinning gel - The viscosity of the gel decreases with increasing shear rate. This process is reversible as the first and second cycle nearly match. Only at lower shear rates the gel would need more time in the second cycle to build up the gel network and reach the viscosity of the first cycle

conditions was about $350\mu m$ thick). In general shrinkage is caused by capillary forces of the evaporating liquid which is water in this case. With solvent exchange to liquids with lower surface tension this effect can be mitigated. Here I used acetone, ethanol or t-butanol to exchange the water out of the gel network. The SEM images of these samples showed layers between about $10-20\mu m$ thick. Additional supercritical drying even led to an approximately $50\mu m$ thick layer. Thickness measurements are only a rough guidance since the values were extracted out of two dimensional SEM images.

Figure 6.5 shows an overview of the porous films after calcination achieved by drying at ambient conditions (xerogel) and drying at supercritical conditions (aerogel). The about $50\mu m$ thick layer of the supercritical dried aerogel is shown in Fig. 6.5a) with some gel fragments located at the former plug positions. By visual inspection the aerogel layer itself looks very uniform and adheres well to the surface. The stability of the dried layer confirms the assumption that a gel network formed instead of a viscous sol which would collapse during drying. By handsaw a part of the tube with the adhered layer was cut out and inspected by SEM. The SEM image in b) of this piece shows a very aerial network similar to the P(DCPD) network in Figure 5.37 on page 106. SEM images of xerogel samples with solvent exchange by ethanol and t-butanol are not shown because of their undesirable skin layer or dense surface. The solvent

exchange with acetone yielded to a porous surface as it can be seen in Fig. 6.5 c). The surface is more dense than in b) but the network still shows open pores.

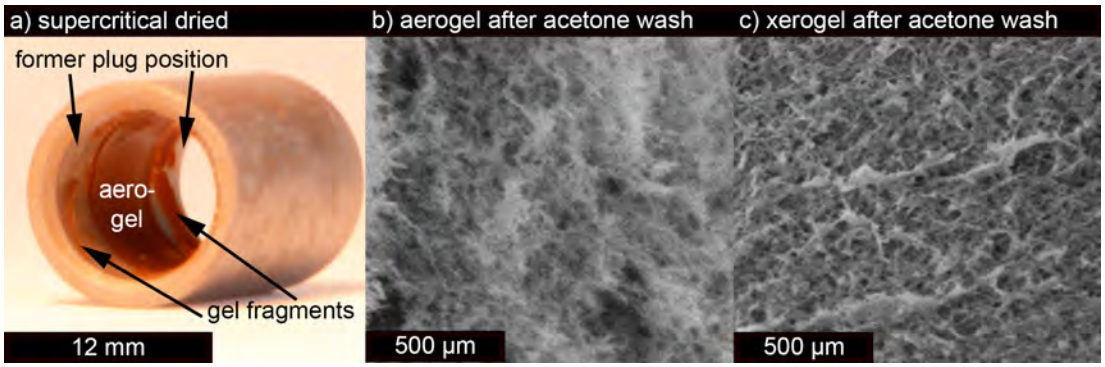

Figure 6.5: Dried gel layers - a) supercritical dried gel layer in the center of the tube showing bigger fragments at the edges where the plug was located. The layer in the center is uniformly distributed and adheres well to the steel tube. b) the magnification of the layer shown in a) by SEM. The layer shows a porous network structure. The image shown is from the cross section of the coating, the top view looked very similar but had some debris particles from the supercritical drying procedure. c) a coated film after solvent exchange with acetone and subsequent drying at room temperature in air. The SEM is top view and a denser but still porous network compared to b) can be seen

EDX measurements of the porous aero- and xerogel (the water of the wet gel was exchanged by acetone and then dried in air for the xerogel) revealed similar elemental compositions with about 50 wt.% oxygen, 36 wt.% aluminium, 9 wt.% iron and remaining chromium and carbon. Chromium was only measured in the thinner xerogel. The iron to aluminium ratio agrees well with the desired 20 % iron of the sol mixture.

The adhesion tests by lightly and heavily knocking the samples did not reveal a considerable weight loss. The scale is up to 0.1 mg accurate and the biggest difference was 0.6 mg for a sample where the metal tubing had no additional heat treatment at 800 °C. All other samples only lost weight within the tolerance of the balance. The quantification of the weight loss during ultra-sonic treatment was even tougher because of the damage caused by the mounting and removal of the plugs. The biggest loss was 2.6 mg but no visual impact on the layer was visible except of the edges where the plug was mounted. An additional adhesion test was performed when cutting out the samples

for the SEM imaging. Even when cutting through the tube and layer the coating still adhered to the tube.

6.3 Conclusion

In summary a sol gel layer out of an aluminium iron mixture can be uniformly coated inside stainless steel tubing. The steel tubing requires pre-treatment of oxidation and heating to enhance its surface properties for the adhesion of the film. The shear thinning aluminium iron sol-gel can be reversibly liquefied and used for coatings while its viscosity increases again. In addition it fulfills the required parameters with a desirable viscosity, good surface wetting and is robustness during shrinkage. The formed gel layer adheres well to the surface and the dried film has a promising porosity for both xero- and aerogel.

7

Conclusion and outlook

In conclusion spherical diamond ablator shells were filled with an almost uniform layer of aerogel. The desired diamond ablator characteristics were discussed in chapter 4 where micro- and nanocrystalline grown diamond samples were characterized regarding their grain size, density, hydrogen content, sp^2 content and surface roughness. The ideal ablator target would have a high density with a smooth as grown surface roughness. In one approach where micro- and nanocrystalline diamond layers were combined in one sample we tried to achieve this requirement. It resulted in an interesting new material which had about 500 uniform layers of micro- and nanocrystalline diamond on top of each other and reached 5 TPa during compression but the density did not increase compared to pure nanocrystalline diamond.(100)

In the following chemistry in a capsule chapter 5 the filling of diamond ablator shells with aerogel is discussed. The major purpose of the aerogel layer within the ablator shell is to embed dopants which would show a characteristic temperature spectrum during the compression in ICF experiments. The aerogel precursor is injected as a liquid with nL precision into the ablator shell and during gelation the capsule is deterministically rotated. The gel layer on the inside of the capsule then gets supercritically extracted and the free standing foam with the embedded dopant is left behind. Apart from being a carrier for the dopant the aerogel as a scaffold for the DT-fuel opens the door for mass production of ICF targets as required for energy generation based on the ICF technology. With the aerogel as fuel scaffold the mass production of ICF targets

gets more feasible.

Currently the NSCL group is working on in-situ synchrotron experiments to understand the cause of the non-concentricity of the aerogel within the ablator shell. First experiments with silicone oil rotated while in-situ radiographs were taken look promising to understand the reaction of the liquid to different viscosities and rotational speeds. Future experiments will include the in-situ observation of a capsule being coated during the formation of the wet gel layer.

The last chapter discusses how the knowledge of the chemistry in a capsule coating technique is transfered to catalytic layers inside tubing. The rimming state sol gel coating has the advantage over washcoating that thicker porous layers are feasible where the gel itself determines the porosity instead of the monolith, c.f page 11 and 24. A promising catalytic layer of porous aluminium-iron-oxide is applied by the sol-gel technique inside metal tubing. The manufactured aero- and xerogel layers adhere well to the pretreated metallic surface and its robustness might enable bundled tube reactors which have excellent heat transfer properties. The catalytic activity of these coatings is now tested at University of Bremen.

References

[1] International Energy Agency. Key world energy statistics 2012. 9 rue de la Federation, 75739 Paris Cedex 15, France, 2012. 1

[2] Christos Agrafiotis and Athena Tsetsekou. Deposition of meso-porous gamma-alumina coatings on ceramic honeycombs by sol-gel methods. *Journal of the European Ceramic Society*, **22**(4):423 – 434, 2002. 12

[3] J. Ashmore, A. E. Hosoi, and H. A. Stone. The effect of surface tension on rimming flows in a partially filled rotating cylinder. *Journal of Fluid Mechanics*, **479**:65–98, 2003. 85

[4] R. D. Atkinson and F. G. Houtermans. On the question of the possibility of building elements in stars. *Zeitschrift Fur Physik*, **54**(9-10):656–665, 1929. 1

[5] Pedro Avila, Mario Montes, and Eduardo E Miro. Monolithic reactors for environmental applications: A review on preparation technologies. *Chemical Engineering Journal*, **109**(1):11–36, 2005. 112

[6] J. E. E. Baglin, A. J. Kellock, M. A. Crockett, and A. H. Shih. Absolute cross-section for hydrogen forward scattering. *Nuclear Instruments & Methods in Physics Research Section B-Beam Interactions with Materials and Atoms*, **64**(1-4):469–474, 1992. 33

[7] S. V. Baryshev, A. V. Zinovev, C. E. Tripa, R. A. Erck, and I. V. Veryovkin. White light interferometry for quantitative surface characterization in ion sputtering experiments. *Applied Surface Science*, **258**(18):6963–6968, 2012. 39

[8] J. Biener, C. Dawedeit, S. H. Kim, T. Braun, M. A. Worsley, A. A. Chernov, C. C. Walton, T. M. Willey, S. O. Kucheyev, S. J. Shin, Y. M. Wang, M. M. Biener, J. R. I. Lee, B. J. Kozioziemski, T. van Buuren, K. J. J. Wu, Jr. J. H. Satcher, and A. V. Hamza. A new approach to foam-lined indirect-drive nif ignition targets. *Nuclear Fusion*, **52**(6):062001, 2012. 16

[9] J. Biener, D. D. Ho, C. Wild, E. Woerner, M. M. Biener, B. S. El-dasher, D. G. Hicks, J. H. Eggert, P. M. Celliers, G. W. Collins, N. E. Teslich, B. J. Kozioziemski, S. W. Haan, and A. V. Hamza. Diamond spheres for inertial confinement fusion. *Nuclear Fusion*, **49**(11), 2009. 12, 24, 25, 46

[10] A. G. Borst and J. J. W. A. van Loon. Technology and developments for the random positioning machine, rpm. *Microgravity Science and Technology*, **21**(4):287–292, 2009. 10, 69

[11] D. K. Bradley, J. H. Eggert, R. F. Smith, S. T. Prisbrey, D. G. Hicks, D. G. Braun, J. Biener, A. V. Hamza, R. E. Rudd, and G. W. Collins. Diamond at 800 gpa. *Physical Review Letters*, **102**(7), 2009. 12

[12] K. A. Brueckner and S. Jorna. Laser-driven fusion. *Reviews of Modern Physics*, **46**(2):325–367, 1974. 2

[13] L. K. Campbell, B. K. Na, and E. I. Ko. Synthesis and characterization of titania aerogels. *Chem Mater*, **4**(6):1329–1333, 1992. ISI Document Delivery No.: KA305 Times Cited: 83 Cited Reference Count: 34 Campbell, lk na, bk ko, ei Amer chemical soc Washington. 55

[14] C. Chen, T. Norimatsu, M. Takagi, H. Katayama, T. Yamanaka, and S. Nakai. Development of foam shells for cryogenic laser fusion targets. *Journal of Vacuum Science & Technology a-Vacuum Surfaces and Films*, **9**(2):340–344, 1991. 19

[15] T. J. B. Collins, A. Poludnenko, A. Cunningham, and A. Frank. Shock propagation in deuterium-tritium-saturated foam. *Physics of Plasmas*, **12**(6):062705, 2005. 17

[16] P. M. Cox, R. A. Betts, C. D. Jones, S. A. Spall, and I. J. Totterdell. Acceleration of global warming due to carbon-cycle feedbacks in a coupled climate model. *Nature*, **408**(6809):184–187, 2000. 1

[17] A. Cybulski and J.A. Moulijn. *Structured Catalysts and Reactors*. Chemical Industries. Taylor & Francis, 2005. 11

[18] C. Dawedeit, S. H. Kim, T. Braun, M. A. Worsley, S. A. Letts, K. J. Wu, C. C. Walton, A. A. Chernov, J. H. Satcher, A. V. Hamza, and J. Biener. Tuning the rheological properties of sols for low-density aerogel coating applications. *Soft Matter*, **8**(13):3518–3521, 2012. 9

[19] C. Dawedeit, C. C. Walton, A. A. Chernov, S. H. Kim, M. A. Worsley, T. Braun, S. A. Gammon, J. H. Satcher, K. J. Wu, A. V. Hamza, and J. Biener. Coating functional sol–gel films inside horizontally-rotating cylinders by rimming flow/state. *Journal of Sol-Gel Science and Technology*, pages 1–8, 2012. 73, 85, 87

[20] A Dewaele, F Datchi, P Loubeyre, and M Mezouar. High pressure–high temperature equations of state of neon and diamond. *Physical Review B*, **77**(9):094106, 2008. 12

[21] F. Dobran. Fusion energy conversion in magnetically confined plasma reactors. *Progress in Nuclear Energy*, **60**:89–116, 2012. 2

[22] L. R. Doolittle. Algorithms for the rapid simulation of rutherford backscattering spectra. *Nuclear Instruments & Methods in Physics Research Section B-Beam Interactions with Materials and Atoms*, **9**(3):344–351, 1985. 33, 42

[23] B. L. Doyle and P. S. Peercy. Technique for profiling h-1 with 2.5-mev vandegraaff ACcelerators. *Applied Physics Letters*, **34**(11):811–813, 1979. 33

REFERENCES

[24] A. C. Ferrari and J. Robertson. Interpretation of raman spectra of disordered and amorphous carbon. *Physical Review B*, **61**(20):14095–14107, 2000. ISI Document Delivery No.: 318LF Times Cited: 2816 Cited Reference Count: 75 Ferrari, AC Robertson, J Amer physical soc College pk. 33

[25] J Filik. Raman spectroscopy: a simple, non-destructive way to characterise diamond and diamond-like materials. *Spectroscopy Europe*, **17**(5):10–17, 2005. 42

[26] M. Fleischmann and S. Pons. Electrochemically induced nuclear-fusion of deuterium. *Journal of Electroanalytical Chemistry*, **261**(2A):301–308, 1989. 2

[27] P.J. Flory. *Principles of polymer chemistry*. Cornell University Press, 1953. 9

[28] M. Funer, C. Wild, and P. Koidl. Novel microwave plasma reactor for diamond synthesis. *Applied Physics Letters*, **72**(10):1149–1151, 1998. 27

[29] M. Füner, C. Wild, and P. Koidl. Simulation and development of optimized microwave plasma reactors for diamond deposition. *Surface and Coatings Technology*, **116-119**(0):853–862, 1999. 27

[30] A. E. Gash, T. M. Tillotson, J. H. Satcher, J. F. Poco, L. W. Hrubesh, and R. L. Simpson. Use of epoxides in the sol-gel synthesis of porous iron(iii) oxide monoliths from fe(iii) salts. *Chem Mater*, **13**(3):999–1007, 2001. 55

[31] G Germani, Pierre Alphonse, Matthieu Courty, Yves Schuurman, and Claudine Mirodatos. Platinum/ceria/alumina catalysts on microstructures for carbon monoxide conversion. *Catalysis today*, **110**(1):114–120, 2005. 110

[32] S.K. Ghosh. *Functional Coatings and Microencapsulation: A General Perspective*, pages 1–28. Wiley-VCH Verlag GmbH & Co. KGaA, 2006. 6

[33] A. Gicquel, K. Hassouni, F. Silva, and J. Achard. Cvd diamond films: from growth to applications. *Current Applied Physics*, **1**(6):479–496, 2001. 28

[34] D. T. Goodin, N. B. Alexander, G. E. Besenbruch, A. S. Bozek, L. C. Brown, L. C. Carlson, G. W. Flint, P. Goodman, J. D. Kilkenny, W. Maksaereekul, B. W. McQuillan, A. Nikroo, R. R. Paguio, R. W. Petzoldt, R. Raffray, D. G. Schroen, J. D. Sheliak, J. Spalding, J. E. Streit, M. S. Tillack, and B. A. Vermillion. Developing a commercial production process for 500 000 targets per day: A key challenge for inertial fusion energy. *Physics of Plasmas*, **13**(5), 2006. 15

[35] W. C. Gough and B. J. Eastlund. Prospects of fusion power. *Scientific American*, **224**(2):50, 1971. 2

[36] J. J. Gracio, Q. H. Fan, and J. C. Madaleno. Diamond growth by chemical vapour deposition. *Journal of Physics D: Applied Physics*, **43**(37):374017, 2010. 42

[37] D. M. Gruen. Nanocrystalline diamond films 1. *Annual Review of Materials Science*, **29**(1):211–259, 1999. 12

[38] Robert Guettel and Thomas Turek. Comparison of different reactor types for low temperature fischer–tropsch synthesis: A simulation study. *Chemical Engineering Science*, **64**(5):955 – 964, 2009. 11

[39] Massimo Guglielmi. Sol-gel coatings on metals. *Journal of Sol-Gel Science and Technology*, **8**(1-3):443–449, 1997. 11, 113

[40] S. W. Haan, J. D. Lindl, D. A. Callahan, D. S. Clark, J. D. Salmonson, B. A. Hammel, L. J. Atherton, R. C. Cook, M. J. Edwards, S. Glenzer, A. V. Hamza, S. P. Hatchett, M. C. Herrmann, D. E. Hinkel, D. D. Ho, H. Huang, O. S. Jones, J. Kline, G. Kyrala, O. L. Landen, B. J. MacGowan, M. M. Marinak, D. D. Meyerhofer, J. L. Milovich, K. A. Moreno, E. I. Moses, D. H. Munro, A. Nikroo, R. E. Olson, K. Peterson, S. M. Pollaine, J. E. Ralph, H. F. Robey, B. K. Spears, P. T. Springer, L. J. Suter, C. A. Thomas, R. P. Town, R. Vesey, S. V. Weber, H. L. Wilkens, and D. C Wilson. Point design targets, specifications, and requirements for the 2010 ignition campaign on the national ignition facility. *Physics of Plasmas*, **18**(5):051001, 2011. 2, 4

[41] G. Hazak, A. L. Velikovich, J. H. Gardner, and J. P. Dahlburg. Shock propagation in a low-density foam filled with fluid. *Physics of Plasmas*, **5**(12):4357–4365, 1998. 17

[42] S. Heusing and M. A. Aegerter. *Sol-Gel Coatings For Electrochromic Devices*, pages 239–274. Advances in Sol-Gel Derived Materials and Technologies. Springer US, 2012. 6

[43] U. Holzwarth and N. Gibson. The scherrer equation versus the 'debye-scherrer equation'. *Nat Nano*, **6**(9):534–534, 2011. 31, 37, 39

[44] A. E. Hosoi and L. Mahadevan. Axial instability of a free-surface front in a partially filled horizontal rotating cylinder. *Phys Fluids*, **11**(1):97–106, 1999. 85

[45] L. W. Hrubesh. Aerogel applications. *Journal of Non-Crystalline Solids*, **225**(1-3):335–342, 1998. 6

[46] Dale L Huber. Synthesis, properties, and applications of iron nanoparticles. *Small*, **1**(5):482–501, 2005. 11, 17

[47] N. Hüsing and U. Schubert. *Aerogels*. Wiley-VCH Verlag GmbH & Co. KGaA, 2000. 6, 54

[48] F. Ito, K. Nagai, M. Nakai, T. Norimatsu, A. Nikitenko, S. Tolokonnikov, E. Koresheva, T. Fujimura, H. Azechi, and K. Mima. Low-density-plastic-foam capsule of resorcinol/formalin and (phloroglucinolcarboxylic acid)/formalin resins for fast-ignition realization experiment (FIRex) in laser fusion research. *Japanese Journal of Applied Physics Part 2-Letters & Express Letters*, **45**(8-11):L335–L338, 2006. 9, 23, 79

[49] K. Y. Jang, K. Kim, and R. S. Upadhye. Study of sol-gel processing for fabrication of hollow silica-aerogel spheres. *J. Vac. Sci. Technol. A-Vac. Surf. Films*, **8**(3):1732–1735, 1990. 19

[50] Jingsheng Jia, Jin Zhou, Hanguo Zhang, Zhongshan Yuan, and Shudong Wang. The influence of preparative parameters on the adhesion of alumina washcoats deposited on metallic supports. *Applied Surface Science*, **253**(23):9099–9104, SEP 30 2007. 114

[51] N. K. Kim, K. Kim, D. A. Payne, and R. S. Upadhye. Fabrication of hollow silica aerogel spheres by a droplet generation method and sol-gel processing. *Journal of Vacuum Science & Technology a-Vacuum Surfaces and Films*, **7**(3):1181–1184, 1989. 9, 19

[52] S. H. Kim, M. A. Worsley, C. A. Valdez, S. J. Shin, C. Dawedeit, T. Braun, T. F. Baumann, S. A. Letts, S. O. Kucheyev, J. W. Kuang Jen, J. Biener, J. H. Satcher, and A.V. Hamza. Exploration of the versatility of ring opening metathesis polymerization: an approach for gaining access to low density polymeric aerogels. *RSC Advances*, **2**(23):8672–8680, 2012. 7, 56

[53] B. J. Kozioziemski, E. R. Mapoles, J. D. Sater, A. A. Chernov, J. D. Moody, J. B. Lugten, and M. A. Johnson. Deuterium-tritium fuel layer formation for the national ignition facility. *Fusion Science and Technology*, **59**(1):14–25, 2011. 4, 15, 90

[54] S. M. Lambert, G. E. Overturf, G. Wilemski, S. A. Letts, D. SchroenCarey, and R. C. Cook. Fabrication of low-density foam shells from resorcinol-formaldehyde aerogel. *Journal of Applied Polymer Science*, **65**(11):2111–2122, 1997. 21

[55] J. I. Langford and A. J. C. Wilson. Scherrer after 60 years - survey and some new results in determination of crystallite size. *Journal of Applied Crystallography*, **11**(APR):102–113, 1978. 31

[56] J. K. Lee and G. L. Gould. Polydicyclopentadiene based aerogel: a new insulation material. *Journal of Sol-Gel Science and Technology*, **44**(1):29–40, 2007. 6, 52, 53, 74, 77

[57] S.A. Letts, S.R. Buckley, Fung-Ming Kong, E.F. Lindsey, and M.L. Sattler. Structure and properties of resorcinol-formaldehyde gels. *MRS Proceedings*, **177**:275–279, 1989. 9, 23

[58] M.H Lewis and B Hattersley. Precipitation of m23c6 in austenitic steels. *Acta Metallurgica*, **13**(11):1159 – 1168, 1965. 113

[59] J. D. Lindl et al. Progress towards ignition on the national ignition facility. *Nuclear Fusion*, **51**(9), 2011. 3, 4

[60] J. D. Lindl, R. L. McCrory, and E. M. Campbell. Progress toward ignition and burn propagation in inertial confinement fusion. *Physics Today*, **45**(9):32–40, 1992. 2

[61] X. Q. Liu, S. W. Tao, and Y. S. Shen. Preparation and characterization of nanocrystalline alpha-fe2o3 by a sol-gel process. *Sensors and Actuators B-Chemical*, **40**(2-3):161–165, 1997. 7

[62] Valérie Meille. Review on methods to deposit catalysts on structured surfaces. *Applied Catalysis A: General*, **315**(0):1 – 17, 2006. 11, 12, 24

[63] Valérie Meille, Stéphanie Pallier, Gabriela V. Santa Cruz Bustamante, Marilyne Roumanie, and Jean-Pierre Reymond. Deposition of -al2o3 layers on structured supports for the design of new catalytic reactors. *Applied Catalysis A: General*, **286**(2):232 – 238, 2005. 11

[64] F. Melo. Localized states in a film-dragging experiment. *Phys Rev E*, **48**(4):2704–2712, 1993. 8, 9, 81

[65] Sh. Michaelson, O. Ternyak, R. Akhvlediani, O. A. Williams, D. Gruen, and A. Hoffman. Hydrogen concentration and bonding in nano-diamond films of varying grain sizes grown by different chemical vapor deposition methods. *physica status solidi (a)*, **204**(9):2860–2867, 2007. 44

[66] R. Miles, M. Spaeth, K. Manes, P. Amendt, M. Tabak, T. Bond, S. Kucheyev, J. Latkowski, G. Loosmore, E. Bliss, K. Baker, S. Bhandarkar, M. Havstad, R. Petzoldt, N. Alexander, M. Tillack, and D. Holdener. Challenges surrounding the injection AND arrival of targets at life fusion chamber center. *Fusion Science and Technology*, **60**(1):61–65, 2011. 15, 16

[67] M. Minnermann, B. Neumann, V. Zielasek, and M. Baumer. Alumina-promoted cobalt and iron xerogels as catalyst for the fischer-tropsch synthesis. *Catal. Sci. Technol.*, pages –, 2013. 12, 17, 116

[68] H. K. Moffatt. Behaviour of a viscous film on the outer surface of a rotating cylinder. *J. de Mecanique*, **16**(5):651–673, 1977. 7, 9, 81

[69] T. Mori, M. Toki, M. Ikejiri, M. Takei, M. Aoki, S. Uchiyama, and S. Kanbe. Silica glass tubes by new sol-gel method. *Journal of Non-Crystalline Solids*, **100**(1–3):523–525, 1988. 8

[70] E. I. Moses, T. D. de la Rubia, E. Storm, J. F. Latkowski, J. C. Farmer, R. P. Abbott, K. J. Kramer, P. F. Peterson, H. F. Shaw, and II Lehman, R. F. A sustainable nuclear fuel cycle based on laser inertial fusion energy. *Fusion Science and Technology*, **56**(2):547–565, 2009. 3

[71] K. S. Murray. Binuclear oxo-bridged iron(iii) complexes. *Coordination Chemistry Reviews*, **12**(1):1–35, 1974. 7

[72] A. Nikroo, D. Czechowicz, R. Paguio, A. L. Greenwood, and M. Takagi. Fabrication and properties of overcoated resorcinol-formaldehyde shells for omega experiments. *Fusion Science and Technology*, **45**(2):84–89, 2004. 22

[73] T. Norimatsu, C. M. Chen, K. Nakajima, M. Takagi, Y. Izawa, T. Yamanaka, and S. Nakai. Cryogenic targets AND related technologies at ile osaka-university. *Journal of Vacuum Science & Technology a-Vacuum Surfaces and Films*, **12**(4):1293–1301, 1994. 22

[74] J. Nuckolls, A. Thiessen, L. Wood, and Zimmerma.G. Laser compression of matter to super-high densities - thermonuclear (CTr) applications. *Nature*, **239**(5368):139–&, 1972. 2

[75] J. Ongena and G. Van Oost. Energy for future centuries prospects for fusion power as a future energy source. *Fusion Science and Technology*, **61**(2T):3–16, 2012. 1

[76] B. Orel, M. Macek, F. Svegl, and K. Kalcher. Electrochromism of IRon-oxide films prepared via the sol-gel route by the dip-coating technique. *Thin Solid Films*, **246**(1-2):131–142, 1994. ISI Document Delivery No.: NQ356 Times Cited: 40 Cited Reference Count: 32 Orel, b macek, m svegl, f kalcher, k Elsevier science sa lausanne Lausanne 1. 24

REFERENCES

[77] Boris Orel, Marjeta Macek, Franc Svegl, and Kurt Kalcher. Electrochromism of iron oxide films prepared via the sol-gel route by the dip-coating technique. *Thin Solid Films*, **246**(1):131–142, 1994. 114

[78] R. R. Paguio, C. A. Frederick, J. F. Hund, D. G. Czechowicz, A. Nikroo, M. Takagi, O. Acenas, and M. Thi. Fabrication capabilities for spherical foam targets used in ICf experiments. *21st IEEE/NPSS Symposium on Fusion Engineering. SOFE 05 (IEEE Cat. No.05CH37764)*, page 5 pp., 2007. 21

[79] R. R. Paguio, A. Nikroo, K. M. Saito, J. F. Hund, E. R. Castillo, N. M. Ravelo, and K. Quan. Improvements on permeation gdp coatings for resorcinol formaldehyde foam shells for cryogenic experiments on omega. *Fusion Science and Technology*, **55**(4):450–455, 2009. 22

[80] R. R. Paguio, M. Takagi, M. Thi, J. F. Hund, A. Nikroo, S. Paguio, R. Luo, A. L. Greenwood, O. Acenas, and S. Chowdhury. Improving the wall uniformity of resorcinol formaldehyde foam shells by modifying emulsion components. *Fusion Science and Technology*, **51**(4):682–687, 2007. 9, 23

[81] Nageswara Rao Peela, Anamika Mubayi, and Deepak Kunzru. Washcoating of gamma-alumina on stainless steel microchannels. *Catalysis Today*, **147, Supplement**(0):S17 – S23, 2009. 114

[82] J. Philip, P. Hess, T. Feygelson, J. E. Butler, S. Chattopadhyay, K. H. Chen, and L. C. Chen. Elastic, mechanical, and thermal properties of nanocrystalline diamond films. *Journal of Applied Physics*, **93**(4):2164–2171, 2003. 12, 13, 45

[83] J. Puetz, F. N. Chalvet, and M. A. Aegerter. Wet chemical deposition of transparent conducting coatings in glass tubes. *Thin Solid Films*, **442**(1–2):53–59, 2003. 8, 24

[84] P. Reichart, G. Datzmann, A. Hauptner, R. Hertenberger, C. Wild, and G. Dollinger. Three-dimensional hydrogen microscopy in diamond. *Science*, **306**(5701):1537–1540, 2004. 43

[85] J. Robertson. Diamond-like amorphous carbon. *Materials Science and Engineering: R: Reports*, **37**(4–6):129–281, 2002. 43

[86] C. C. Röhlig, M. Niebelschütz, K. Brueckner, K. Tonisch, O. Ambacher, and V. Cimalla. Elastic properties of nanowires. *physica status solidi (b)*, **247**(10):2557–2570, 2010. 35

[87] Claus-Christian Röhlig. *Evaluierung elastischer Eigenschaften von Mikro- und Nanostrukturen*. PhD thesis, Albert-Ludwigs-Universität Freiburg im Breisgau, 2011. 35

[88] M. D. Sacks and R. S. Sheu. Rheological properties of silica sol-gel materials. *Journal of Non-Crystalline Solids*, **92**(2-3):383–396, 1987. 15

[89] R. A. Sacks and D. H. Darling. Direct drive cryogenic ICf capsules employing d-t wetted foam. *Nuclear Fusion*, **27**(3):447–452, 1987. 19

[90] S. Sahin, H. M. Sahin, and A. Acir. Life hybrid reactor as reactor grade plutonium burner. *Energy Conversion and Management*, **63**:44–50, 2012. 3

[91] P.A. Sørensen, S. Kiil, K. Dam-Johansen, and C.E. Weinell. Anticorrosive coatings: a review. *Journal of Coatings Technology and Research*, **6**(2):135–176, 2009. 11

[92] P. Scherrer. Estimation of the size and structure of colloidal particles by rontgen rays. *Nachrichten von der Koniglicher Gesellschaft der Wissenschaften zu Gottingen, Mathematisch-Physikalische Klasse*, (i):96–100100, 1918. 31, 37

[93] D. S. Schimel, J. I. House, K. A. Hibbard, P. Bousquet, P. Ciais, P. Peylin, B. H. Braswell, M. J. Apps, D. Baker, A. Bondeau, J. Canadell, G. Churkina, W. Cramer, A. S. Denning, C. B. Field, P. Friedlingstein, C. Goodale, M. Heimann, R. A. Houghton, J. M. Melillo, B. Moore, D. Murdiyarso, I. Noble, S. W. Pacala, I. C. Prentice, M. R. Raupach, P. J. Rayner, R. J. Scholes, W. L. Steffen, and C. Wirth. Recent patterns and mechanisms of carbon exchange by terrestrial ecosystems. *Nature*, **414**(6860):169–172, 2001. 1

[94] P. Schwab, R.H. Grubbs, and J.W. Ziller. Synthesis and applications of rucl12(chr)(pr3)2 the influence of the alkylidene moiety on metathesis activity. *J. Am. Chem. Soc.*, **118**(number):100–110, 1996. 74

[95] J. Schwan, S. Ulrich, H. Roth, H. Ehrhardt, S. R. P. Silva, J. Robertson, R. Samlenski, and R. Brenn. Tetrahedral amorphous carbon films prepared by magnetron sputtering and dc ion plating. *Journal of Applied Physics*, **79**(3):1416–1422, 1996. 44

[96] G. Seiden and P. J. Thomas. Complexity, segregation, and pattern formation in rotating-drum flows. *Rev Mod Phys*, **83**(4):1323–1365, 2011. 87

[97] T. Sharda, T. Soga, and T. Jimbo. Optical properties of nanocrystalline diamond films by prism coupling technique. *Journal of Applied Physics*, **93**(1):101–105, 2003. 39

[98] X. Sheng, J. K. Lee, and M. R. Kessler. Influence of crosslink density on the properties of ROMp thermosets. *Polymer*, **50**(5):1264–1269, 2009. 74

[99] V. Smil. *Enriching the Earth: Fritz Haber, Carl Bosch, and the Transformation of World Food Production*. MIT Press, 2004. 17

[100] R. F. Smith, J. H. Eggert, D. G. Braun, J.R. Patterson, R. E. Rudd, R. Jeanloz, T.S. Duffy, J. Biener, Lazicki A.E., A.V. Hamza, J. X. Wang, T. Braun, L.X. Benedict, P. M. Celliers, and G. W. Collins. Diamond to 5 tpa. *Science*, **submitted**, 2013. 47, 121

[101] N Takahashi, N Kakuta, A Ueno, K Yamaguchi, T Fujii, T Mizushima, and Y Udagawa. Characterization of iron oxide thin film prepared by the sol-gel method. *Journal of materials science*, **26**(2):497–504, 1991. 114

[102] M. Takaqi, T. Norimatsu, T. Yamanaka, S. Nakai, and H. Ito. A novel technique to make foam shells with high sphericity and wall uniformity for cryogenic laser fusion-targets. *Journal of Vacuum Science & Technology a-Vacuum Surfaces and Films*, **9**(3):820–823, 1991. 21

[103] E. Teller. Work of many people. *Science*, **121**(3139):267–275, 1955. 2

[104] S. T. Thoroddsen and L. Mahadevan. Experimental study of coating flows in a partially-filled horizontally rotating cylinder. *Experiments in Fluids*, **23**(1):1–13, 1997. 81, 85

[105] Department of Economic United Nations, Population Estimates Social Affairs, Population Devision, and Projections Section. Total population - both sexes, 6 2011. 1

[106] J.C. Vickerman. *Surface analysis: the principal techniques*. John Wiley, 1997. 32

[107] C. T. Wang and R. J. Willey. Fine particle iron oxide based aerogels for the partial oxidation of methanol. *Catalysis Today*, **52**(1):83–89, 1999. 7

[108] Duhua Wang and Gordon. P. Bierwagen. Sol–gel coatings on metals for corrosion protection. *Progress in Organic Coatings*, **64**(4):327 – 338, 2009. 11, 12

[109] H. Watanabe, C. E. Nebel, and S. Shikata. Isotopic homojunction band engineering from diamond. *Science*, **324**(5933):1425–1428, 2009. 12

[110] B. Weiss and R. Stickler. Phase instabilities during high temperature exposure of 316 austenitic stainless steel. *Metallurgical Transactions*, **3**(4):851–866, 1972. 113

[111] O. A. Williams. Nanocrystalline diamond. *Diamond and Related Materials*, **20**(5–6):621–640, 2011. 12, 41

[112] M. Wiora, K. Brühne, A. Flöter, P. Gluche, T. M. Willey, S. O. Kucheyev, A. W. Van Buuren, A. V. Hamza, J. Biener, and H. J. Fecht. Grain size dependent mechanical properties of nanocrystalline diamond films grown by hot-filament cvd. *Diamond and Related Materials*, **18**(5–8):927–930, 2009. 13, 39, 41, 44

[113] M. A. Worsley, S. O. Kucheyev, J. H. Satcher, A. V. Hamza, and T. F. Baumann. Mechanically robust and electrically conductive carbon nanotube foams. *Applied Physics Letters*, **94**(7), 2009. 7

[114] H. Yang, K. Nagai, N. Nakai, and T. Norimatsu. Thin shell aerogel fabrication for FIRex-i targets using high viscosity (phloroglucinol carboxylic acid)/formaldehyde solution. *Laser and Particle Beams*, **26**(3):449–453, 2008. 9, 21, 23, 79

[115] J. Zhao, F. E. Huggins, Z. Feng, F. L. Lu, N. Shah, and G. P. Huffman. Structure of a nanophase iron oxide catalyst. *J Catal*, **143**(2):499–509, 1993. 7

[116] Su Zhao, Jizhong Zhang, Duan Weng, and Xiaodong Wu. A method to form well-adhered gamma-al2o3 layers on fecral metallic supports. *Surface and Coatings Technology*, **167**(1):97–105, 2003. 114

[117] M. L. Zheludkevich, I. Miranda Salvado, and M. G. S. Ferreira. Sol-gel coatings for corrosion protection of metals. *J. Mater. Chem.*, **15**:5099–5111, 2005. 11

Declaration

Detailed list of my contributions:

- Atomic Force Microscopy measurements and data analysis (Fig. 4.3d-f, 4.6)
- Coatings in vials and capsules (Fig. 5.18, 5.21, 5.22, 5.23, 5.25, 5.26, 5.28, 5.36a-b) except of Fig. 5.29c
- Design and development of a custom Random Positioning Machine with Lab View interface (Fig. 5.12, 5.13)
- Design and development of custom hot-dog-rollers to turn cylinders (Fig. 5.11d)
- Design and development of the custom capsule fill procedure (Fig. 5.8)
- Design and development of the capsule holders (Fig. 5.7 and 5.29a-b)
- Development of density measurements for samples below 10 mg, by modifying a Mettler Toledo XP56 balance (Fig. 4.9b)
- Development of the pressure cycling setup with LabView interface (Fig. 5.31)
- Fourier Transformed Infrared Spectroscopy device setup, measurements and data analysis for characterizing the content of filled diamond capsules (Fig. 4.8b 5.32 5.35)
- Assisted in some Soft X-ray Absorption Near Edge Structure measurements at SSRL (Fig. 4.7a)
- Introducing and setting up a wiki to track the coating results (Fig. 5.6)
- Raman spectroscopy data anaylsis (Fig 4.7b)

- Rheology experiments and calibration (Fig. 5.10, 5.14, 5.15, 5.16, 5.17, 5.18, 5.20)
- Scanning Electron Microscopy data analysis (Fig. 4.6)
- Setup of a commericial supercritical dryer and some drying (Fig. 5.33)
- Some X-ray diffraction data analysis (Fig. 4.6)
- The linear interpolation of Elastic Recoil Detection analysis results that were not simulated by Sergei Kucheyev (only two of ten samples were simulated) (Fig. 4.9a)
- Grain size distribution of Transmission Electron Microscopy and Electron Backscatter Diffraction (Fig. 4.6)
- Verifying the failure of the liquid iodine doping (Fig. 5.5)

And I would like to thank my collaborators for the following work:

- Alex Chernov: For his research in existing analytical coating solutions (Fig. 5.25 and Eq. 5.9)
- Anthony van Buuren, Trevor Willey, Michael Bagge-Hansen and Jon Lee: For the For the Soft X-ray Absorption Near Edge Structure measurements (Fig. 4.7a) and the computer tomography in Fig. 5.36
- Arne Wittstock and Marcus Worsley: For the initial development of filling aerogel in the capsule (Fig. 3.2)
- Bassem el Dasher: For the Electron Backscatter Diffraction measurement (Fig. 4.4a-b)
- Christopher Walton: For the power spectral density plots (Fig. 5.27) and computational fluid dynamics simulations (Fig. 5.24, 5.25, 5.30)
- Edward Lindsey, Monika Biener: For making the Scanning Electron Microscopy images of the diamond (Fig. 4.3a-c and appendix A)
- Kuang Jen Wu: For performing all the radiography measurements
- Kaung Jen Wu, Tony van Buuren, Trevor Willey and Tom Braun: For the hydrogen filling experiment (Fig. 5.4)
- Marcus Worsley: For the some Scanning Electron Microscopy images of the aerogels (Fig. 5.37) and some supercritical drying

- Sergei Kucheyev: For the Elastic Recoil Detection Analysis (Fig. 4.8a)
- Sung Ho Kim: For most of the supercritical drying (Fig. 5.34) and the development of new polymers (Fig. 5.2).
- Tom Braun: For running the pressure calibration measurement for the capsule fill procedure (Fig. 5.9) and for running the density measurement in Fig 4.9b
- Yinmin (Morris) Wang: For the TEM images (Fig. 4.4)
- Fraunhofer IAF and especially Christoph Wild, Lutz Kirste and Eckard Woerner: For the White Light Interferometry measurements (Fig. 4.3g-i), the X-ray diffraction measurements (Fig. 4.2 4.5), the growth of the diamond samples (Fig. 4.1 4.11), the Raman measurements (Fig 4.7b), the Fourier transformed infrared spectroscopy (Fig. 4.8b) and the Young's modulus measurements (Fig. 4.9b)
- The Institut für Angewandte und Physikalische Chemie group of Marcus Bäumer at University of Bremen and especially Miriam Klink and Martin Nowak: For the development of an aluminium-iron based xerogel and building a custom bottle roller

Appendix A

Diamond SEM

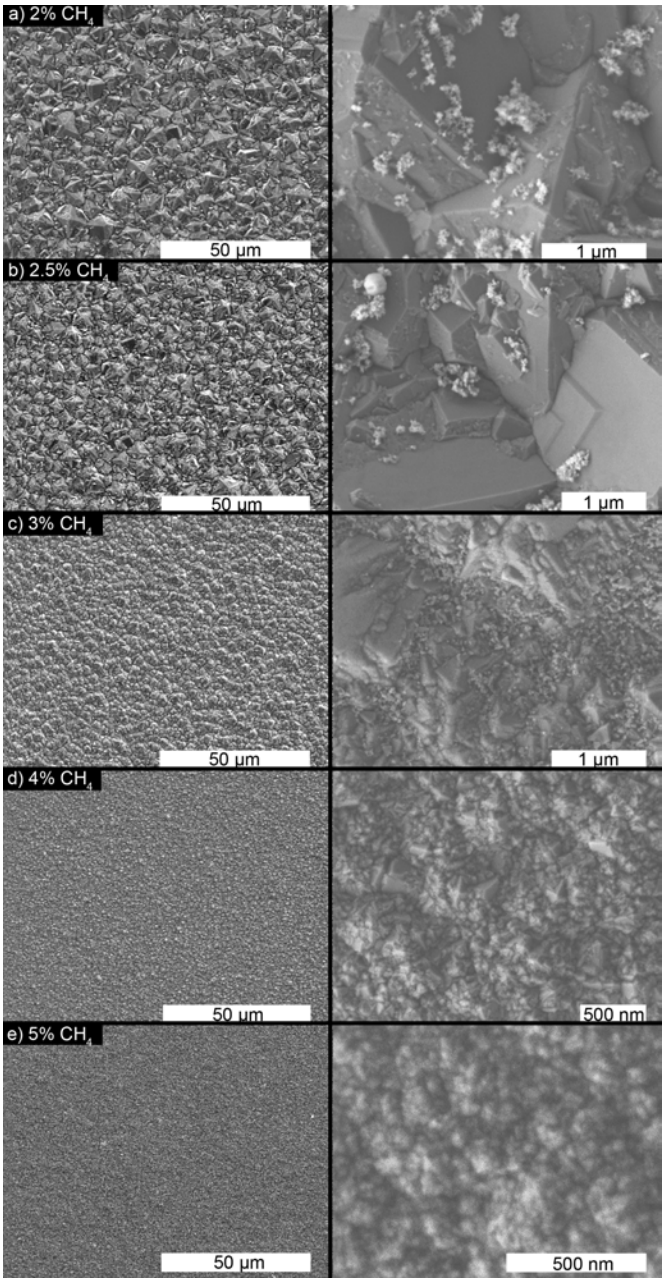

Figure A.1: Surface morphology - the crystallite size decreases with increasing CH_4 concentration. a-b) show bigger crystallites while in c) a mixture of very small and big crystallites is visible. d-e) only contain smaller crystallites

Appendix B

Capsule Holder

B. CAPSULE HOLDER

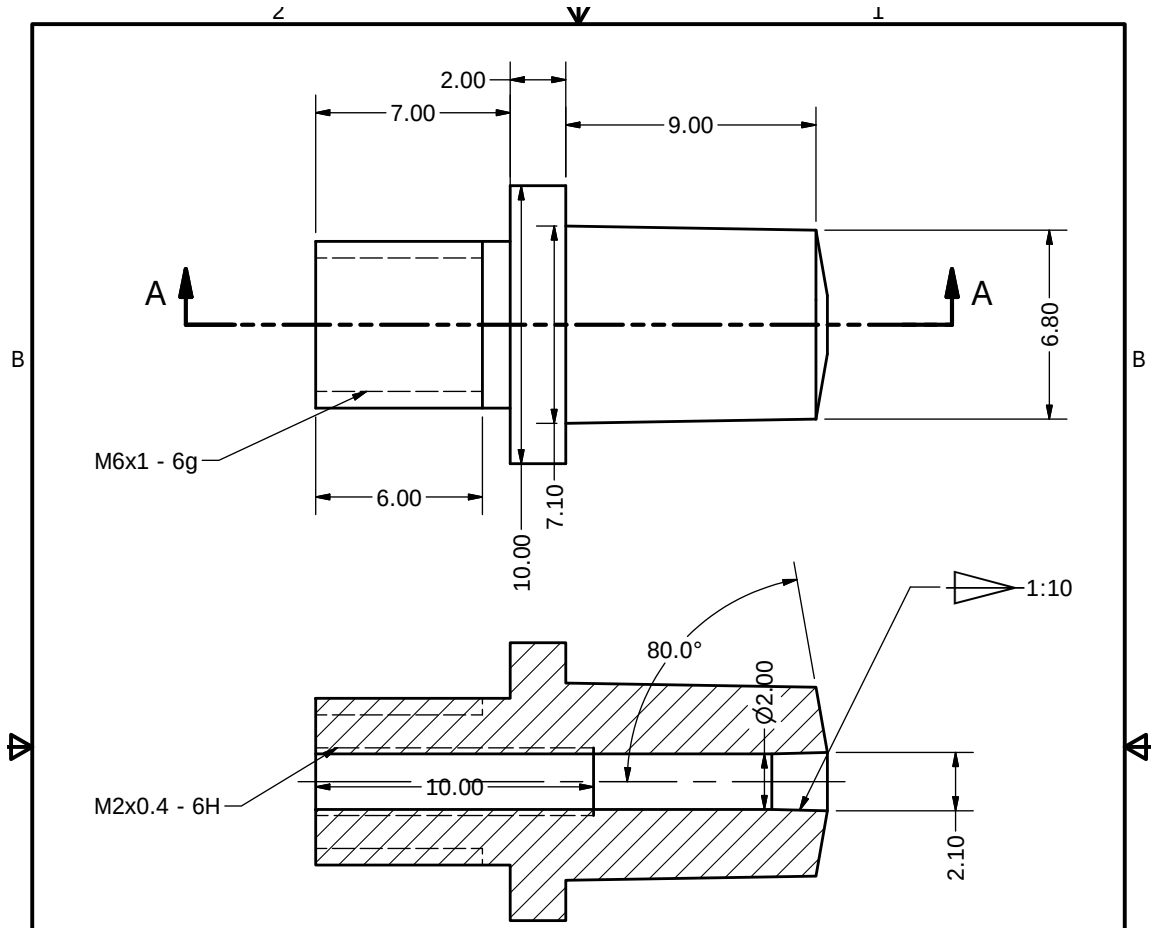

SECTION A-A
SCALE 5: 1

DRAWN dawedeit1	3/20/2012	holder 6, PTFE Teflon		
CHECKED		TITLE		
QA		metric dimensions, Scale 5:1		
MFG				
APPROVED		SIZE A	DWG NO holder 6	REV
		SCALE		SHEET 1 OF 1

Appendix C

Random Positioning Machine

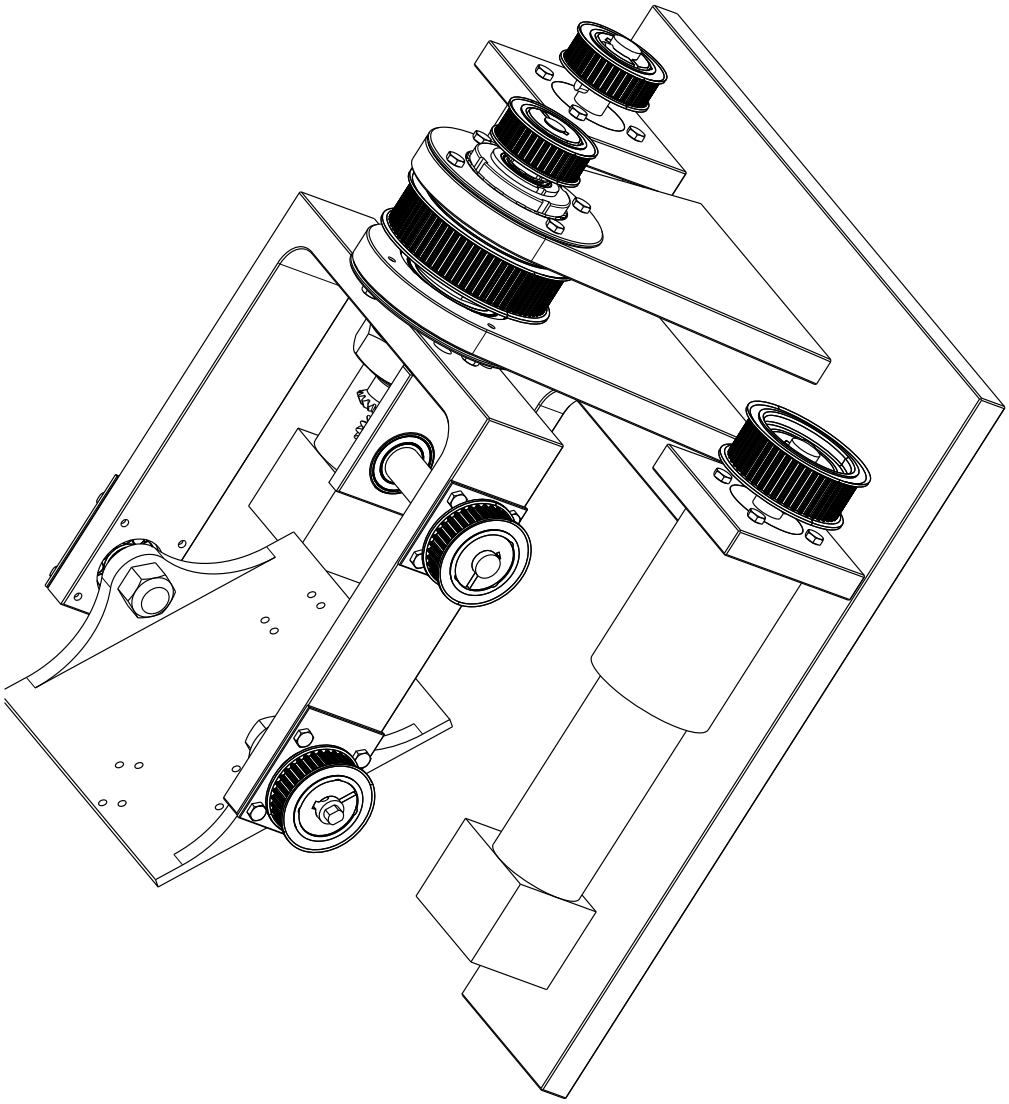

1	2	3	4	5	6
Position	Amount	Unit	Description	Supplement	Comment
1	1		U Shape Sample Holder		
2	1		Type X Bearing	QJ304-MPA	
3	1		Shaft type X bearing		
4	2		Parallel Key	DIN 6885A 5x5x20	
5	4		Lock Nut	KB4	
6	4		Lock Washer	MB4	
7	1		Shaft NU Cylindrical Bearing		
8	1		Cylindrical roller bearing	NU204-E-TVP2	
9	1		Inner Rotation Plate		
10	2		Hexagon Nut	ISO4032 M18	
11	20		Hexagon Screw	ISO4017 M6x20	
12	1		Bearing Holder NU		
13	2		Ball Bearing	6004-2RSR	
14	1		Shaft Miter Gears		
15	2		Parallel Key	ANSI B17.1 3/32 x 3/32 x 1/2 inch	
16	1		Bearing Holder Miter Gear floating		
17	10		Hexagon socket head screw	ISO4762 M6x20	Only 2used at pos. 17,others used for pos. 9
18	1		Bearing holder miter gear		
19	2		Taper Lock	1108 16mm	
20	4		Sprocket	P36-5MGT-15	
21	2		Miter Gear	HMK 1616	
22	1		Outer Shaft		
23	1		Inner Shaft		
24	2		Ball Bearing	6003-2RSR	
25	2		Lock Washer	MB3	
26	2		Lock Nut	KM3	
27	1		Internal Circlip	D=37mm	
28	1		Parallel Key	DIN 6885A 5x5x14	
29	1		Thin Nut	Nut M40x1.5	if necessary Lock Nut KM8 or custom made
30	1		Ball Bearing	6010-2RSR	
31	1		Ball Bearing	6009-2RSR	
32	1		Parallel Key	ANSI B17.1 1/2 x 1/2 x 1 inch	Check for right key with bushing pos 33
33	1		Taper Lock	2012 2 1/8 inch	
34	1		Bearing holder outer shaft 75mm		
35	1		Bearing holder outer shaft 80mm		
36	1		75mm Bearing lid		
37	1		80mm Bearing lid		
38	1		Taper Lock	1108 14mm	
39	1		Sprocket	P68-5MGT-25	
40	1		Ground Plate		
41	2		Motor Holder		
42	1		Belt	5MR-800-25	
43	1		Belt	5MR-535-15	
44	1		Belt	5MR-625-15	
45	8		Hexagon Screw	ISO 4017 M6x16	
46	1		Lock Nut	KM9	
47	1		Lock Washer	MB9	
48	1		Taper Lock	1108 19mm	
49	1		Taper Lock	1210 19mm	
50	1		Sprocket	P48-5MGT-25	
51	1		Bearing holder type X		
52	1		Sampleholder		not shown in assembly
53	1		Sampleholder lid		not shown in assembly

C. RANDOM POSITIONING MACHINE